Boston University

OpenBU **http://open.bu.edu**

Theses & Dissertations Boston University Theses & Dissertations

2019

Improving electrochemical performance of Nickel - Yttria stabilized Zirconia cermet anodes employing nickel nanoparticles

https://hdl.handle.net/2144/37980

Boston University

BOSTON UNIVERSITY

COLLEGE OF ENGINEERING

Dissertation

IMPROVING ELECTROCHEMICAL PERFORMANCE OF NICKEL – YTTRIA STABILIZED ZIRCONIA CERMET ANODES EMPLOYING NICKEL NANOPARTICLES

by

PAUL JOSEPH GASPER

B.S., Worcester Polytechnic Institute, 2013
M.S., Worcester Polytechnic Institute, 2014

Submitted in partial fulfillment of the

requirements for the degree of

Doctor of Philosophy

2019

© 2019 by
PAUL JOSEPH GASPER
All rights reserved

Approved by

First Reader

Uday B. Pal, Ph.D.
Professor of Mechanical Engineering
Professor of Materials Science and Engineering

Second Reader

Soumendra N. Basu, Ph.D.
Professor of Mechanical Engineering
Professor and Associate Division Head of Materials Science and Engineering

Third Reader

Srikanth Gopalan, Ph.D.
Associate Professor of Mechanical Engineering
Associate Professor of Materials Science and Engineering

Fourth Reader

Chuanhua Duan, Ph.D.
Assistant Professor of Mechanical Engineering
Assistant Professor of Materials Science and Engineering

ACKNOWLEDGMENTS

This work couldn't have been done without the help from many different people in my life. First and foremost, I'd like to show my gratitude for the lifetime of support given to me by my parents, Drs. Joseph and Juli-Ann Gasper. Throughout my childhood, they fostered in me a love of science and engineering, and always helped me to achieve my own goals. They've pushed me to become independent by pursuing my ambitions, but have also aided me when it was needed, and without that aid, I don't think it would have been possible for me to pursue my doctorate. So, to my parents, I will always be grateful.

I am also grateful for the love and support of my partner, Stasia. You've always built up my confidence in myself, even though I probably have a lot to spare already, but confidence is often in short supply in the midst of research, and it's always appreciated. Also, you bring the balance of emotional awareness and kindness to the very intellectual effort of getting my doctorate; without you, I would not be as stable or as happy as I am today. Finally, you bring an attention to detail and care that makes possible our effort to live healthy and environmentally friendly lives, which mirrors my intellectual pursuit of sustainable energy technologies. This balance brings completeness to both my work and my daily life, and I am proud of the lives we are trying to build together.

I would also like to acknowledge the support of my many advisors at Boston University (BU). I am sincerely grateful for the generous support and honest criticism from my primary advisor, Prof. Uday B. Pal. After we first spoke, I was hopeful that I would be able to learn from you and also have the independence to make contributions

that I felt were personally important to the research. Because of our conversation I applied to BU, and I'm very happy to say these hopes came true. In addition, I'd like to thank Prof. Soumendra N. Basu for your criticism of my writing and presentations, which dramatically improved the quality of our published works. And finally, I'd like to thank Prof. Srikanth Gopalan, whose careful consideration of the basic science and contributions during meetings helped me to understand my results and to design new experiments.

Any mention of my collaborators at BU would not be complete without an acknowledgement of my partner-in-crime, Yanchen Lu, Ph.D. Our daily conversations about experimental results, sharing of newly found literature, and analysis of each other's work were the backbone of my time at BU. And perhaps most importantly, you bring a humor and levity into our work, which I will certainly miss. I also would like to acknowledge the friendship and support of all of my current and prior lab mates, which at this point have numbered too many to list in full!

I would also like to acknowledge the technical and administrative support of BU staff, particularly Bob Sjostrom and David Campbell in EPIC, Anlee Krupp in the Photonics Center, and Elizabeth Flagg and Ruth Mason.

Finally, I gratefully acknowledge the United States of America Department of Energy for financially supporting my research under award number DEFE0026096. I hope to be able to use my education to contribute positively to my country.

IMPROVING ELECTROCHEMICAL PERFORMANCE OF NICKEL – YTTRIA STABILIZED ZIRCONIA CERMET ANODES EMPLOYING NICKEL NANOPARTICLES

PAUL JOSEPH GASPER

Boston University College of Engineering, 2019

Major Professor: Uday B. Pal, Ph.D., Professor of Mechanical Engineering, Professor of Materials Science and Engineering

ABSTRACT

Nickel-Yttria Stabilized Zirconia (Ni-YSZ) cermets are used as anodes in solid oxide fuel cells. These anodes are stable for tens of thousands of hours during operation and have low cost. In this work, Ni-YSZ anodes are infiltrated with nickel nanoparticles to increase the density of electrochemical reaction sites and improve their performance. However, infiltrated nickel nanoparticles are isolated from one another, so they are not electrochemically active. Two approaches have been utilized to activate infiltrated nickel nanoparticles: in-situ nickel spreading and simultaneous infiltration of nickel with $Gd_{0.1}Ce_{0.9}O_{2-\delta}$ (GDC). In-situ nickel spreading, which occurs during exposure to anodic mass transfer limited currents, connects and activates nickel nanoparticles, improving anode performance but inherently causing nanoparticle coarsening. Simultaneous infiltration of Ni and GDC results in substantially improved anode performance, and the infiltrated nanostructures are more stable than infiltrated nickel. Detailed analysis of the electrochemical impedance by equivalent circuit modeling is used to separate the contributions of nickel and GDC infiltrants to the overall cell performance.

TABLE OF CONTENTS

LIST OF TABLES

LIST OF FIGURES

LIST OF ABBREVIATIONS

AAL ..... Anode Active Layer

AC ..... Alternating Current

DC ..... Direct Current

DRT ..... Distribution of Relaxation Times

ECM ..... Equivalent Circuit Model

EIS ..... Electrochemical Impedance Spectroscopy

FIB ..... Focused Ion Beam

FLW ..... Finite Length Warburg

GDC ..... Gadolinium Doped Ceria

Ge ..... Gerischer

I-V ..... Current – Voltage

LSM ..... Lanthanum Strontium Manganite

MSRI ..... Materials and Systems Research, Inc.

OCV ..... Open Circuit Voltage

SEM ..... Scanning Electron Microscope

SOFC ..... Solid Oxide Fuel Cell

STEM ..... Scanning Transmission Electron Microscope

TEM ..... Transmission Electron Microscope

TPB ..... Triple Phase Boundary

YSZ ..... Yttria Stabilized Zirconia

1. BACKGROUND AND PROBLEM STATEMENT

Solid oxide fuel cells (SOFCs) are electrochemical systems that convert chemical fuel, such as hydrogen or hydrocarbon gasses, into electrical energy. Because SOFCs are not limited by Carnot efficiency, they are much more efficient for electricity generation than turbines or engines, reaching up to 60% electrical efficiency [1–4]. SOFCs operate without combustion, so they emit hundreds of times less polluting exhausts than any combustion process [1,4,5]. This includes both CO_2 emission as well as NO_x, SO_2, and particulate emissions. SOFCs also are noise and vibration free, only requiring pumps to move fuel and oxidant gasses. Additionally, SOFCs are modular, allowing individual cells to be arranged in series or parallel without impacting the overall efficiency.

However, SOFCs are still not widely adopted for energy generation. The factors limiting SOFC adoption can be broken down into three issues: cost, durability, and performance. Thus, the goal of this project is to improve the properties of SOFC anodes by using one or more of the following approaches: reducing the cost, increasing the durability, and improving the performance. Because nickel – yttria stabilized zirconia (Ni-YSZ) cermet anodes are by far the most common and least expensive material for SOFC anodes, approaches that aim to improve Ni-YSZ cermets with minimal processing will be considered.

In recent years, new approaches for improving SOFC anode performance have emerged; foremost among these is liquid infiltration, a technique by which metallic or oxide materials can be introduced into the porous electrode [6–9]. The critical advantage of the infiltration technique is that infiltrated materials can be introduced after sintering

of the bulk electrode, producing nanoscale features that would coarsen at sintering temperatures. The effect of infiltration on electrode performance is perhaps best typified by the manufacturing of electrodes where all of the nickel in introduced via infiltration into a porous YSZ substrate. Infiltrated nickel features in these electrodes have a smaller average feature size than those of a conventionally manufactured Ni-YSZ cermet, thus increasing the average density of electrochemical reaction sites [10,11]. This results in high initial electrochemical performance compared with Ni-YSZ cermets [11–13]. However, infiltrating enough nickel to ensure that the electrical conductivity of the electrode is high is time consuming, requiring a large number of infiltration cycles [14,15]. Because of this difficulty, this approach has not yet been adopted commercially.

Surprisingly, the use of liquid infiltration to introduce nanometer scale nickel features into Ni-YSZ cermet anodes has not been thoroughly studied. This is perhaps because of the processing required. Ni-YSZ anodes are usually prepared in-situ by reducing the sintered NiO-YSZ composite. Handling and processing of the reduced Ni-YSZ electrode is a concern, as the electrode is more fragile after being reduced. Some researchers have avoided this problem by infiltrating the NiO-YSZ composite before reduction [16–20]. However, all of these studies manufactured their own NiO-YSZ electrodes, presumably with enough porosity to enable liquid infiltration. This approach is not easy to replicate. Commercially available NiO-YSZ electrode supported SOFCs cannot be effectively infiltrated; these electrodes must be ‘pre-reduced’ before liquid infiltration can occur. The pre-reduction process requires heating the assembled testing apparatus up to the reduction temperature, usually 800°C, reducing the anode from NiO-

YSZ to Ni-YSZ under flow of a reducing gas, then cooling back to room temperature. This heating cycle risks degradation of the electrolyte as well as the gas seals in a stack.

To this author's knowledge, the only published literature on liquid infiltration of pre-reduced Ni-YSZ anode supported SOFCs is from two recent studies by researchers at Haldor Topsøe A/S [21]. Their results showed that infiltration of reduced Ni-YSZ electrodes can be conducted on commercially sized SOFC stacks without negative consequences for the performance of the cell, with both studies reporting improved performance. However, these studies infiltrated different materials and had different testing methodologies. So, while the approach of infiltrating pre-reduced Ni-YSZ electrodes seems to be validated, the lack of systematic investigation means that the impact of nickel infiltration on Ni-YSZ electrode performance is not clear.

One key detail that needs to be discussed when considering this approach for improving SOFC anodes is the electronic connectivity of infiltrated nickel nanoparticles. To contribute to the electrochemical reaction in the anode, nickel nanoparticles deposited on the YSZ must be connected with one another as well as with the nickel of the Ni-YSZ cermet. When infiltrated, nickel nanoparticles deposit homogenously on YSZ, but are not connected with one another. This problem is most simply addressed by infiltrating enough nickel to connect particles to one another. For nickel nanoparticles to percolate on YSZ, the surface coverage needs to be approximately 50-60% [10,22]. This corresponds to approximately 15 vol% of infiltrated nickel within the electrode, approximately half of the total electrode porosity of a Ni-YSZ cermet anode [22]. This would have clear negative consequences for cell performance.

So, this research aims to improve the electrochemical performance of Ni-YSZ anodes by employing nickel nanoparticles to increase the electrochemical reaction site density. The issue of nanoparticle connectivity within the electrode will be addressed in several ways. Firstly, nickel nanoparticles may be modified in-situ by exposure to high humidity. This causes spreading of infiltrated nickel nanoparticles, due to the influence of H_2O partial pressure on the equilibrium contact angle between nickel and YSZ [23]. Secondly, additional conducting phases such as gadolinium-doped-ceria (GDC) may be infiltrated into the anode in order to facilitate connection between nickel nanoparticles and the Ni-YSZ cermet. In order to address these goals, Section 2 of this dissertation describes the relevant features of SOFCs, describes the techniques for measuring electrochemical performance of SOFCs, reviews prior research utilizing liquid infiltration for improving SOFC anodes, and discusses the two approaches for connecting nickel nanoparticles mentioned previously. Section 3 describes the experimental results of a study on the impact of in-situ spreading of nickel nanoparticles on the performance and stability of nickel infiltrated electrodes. Section 4 describes the experimental results of a study on the electrochemical performance and stability of nickel infiltrated, GDC infiltrated, and Ni-GDC infiltrated electrodes. In order to quantify the impact of each infiltrant on the anodic charge transfer resistance and anodic mass transfer resistance, fitting of the electrochemical impedance spectroscopy data was done by equivalent circuit modeling; this procedure has been documented in Section 4.3.

2. LITERATURE REVIEW

2.1 Solid oxide fuel cells

Solid oxide fuel cells utilize a ceramic oxide membrane, which requires operating temperatures between 600°C – 1000°C to maintain high ionic conductivity. This high operating temperature has several unique advantages over other types of fuel cell systems. SOFCs operate exothermically, producing high temperature exhaust heat that is desirable for cogeneration applications. High temperature operation also enables SOFCs to use many different types of hydrocarbon fuels by employing internal or external fuel reformation [1,5]. However, high operating temperatures also present several challenges for SOFC system design. Thermal expansion during heating and cooling cycles necessitates careful matching of coefficient of thermal expansion between stack components [3,24]. The chemical compatibility and stability of materials at both processing and operating temperatures also needs to be managed when selecting materials [6]. Finally, long term operation at high temperatures results in performance degradation due to many factors, including phase stability, gas contamination of electrodes, and changes of the operating conditions during testing [6,7,25–27].

A single cell of an SOFC consists of three layers: anode, cathode, and electrolyte. During fuel cell operation, a fuel gas mix is passed over the anode and an oxygen gas mix is passed over the cathode. Molecular oxygen in the cathode is ionized by electrons from an external circuit, and then these ions are conducted across the electrolyte to the anode, where they oxidize the fuel, producing water vapor and electrons. The current and voltage of the cell is measured across the external circuit. Figure 1 shows the

electrochemical reaction of H_2 fuel and oxygen. As the figure shows, other fuels can also be used.

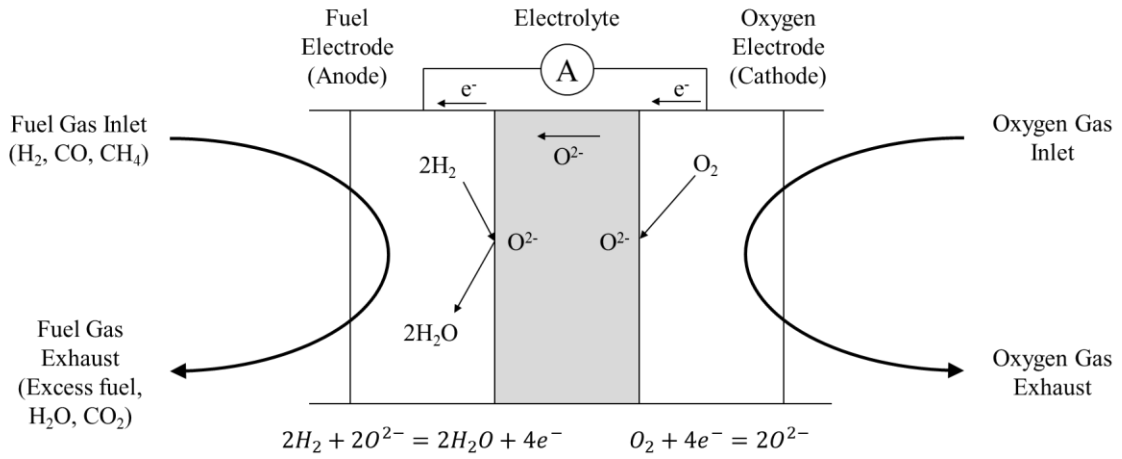

Figure 1: Schematic of the electrochemical reaction of H_2 fuel and an oxidant in a solid oxide fuel cell

The most common SOFC architecture currently used is the planar anode supported cell. This cell utilizes a porous Ni-YSZ cermet anode up to 1 mm thick, a dense YSZ electrolyte that is as thin as possible, and a composite cathode composed of YSZ and an electrically conductive material that is favorable to the oxygen reduction reaction. Traditionally, the cathode material of choice has been Strontium doped Lanthanum Manganite (LSM). Both the anode and cathode contain an 'active layer' at the electrode-electrolyte interface. These active layers have finer microstructures than the rest of the electrode, and are thus more favorable for electrochemical reactions. A schematic of the cross section of an anode supported SOFC before the reduction of NiO to Ni can be seen in Figure 2. There are many other possible materials and cell architectures for solid oxide fuel cells [24,28–32], but this research focuses on improving the performance of standard Ni-YSZ anode supported cells by improving the kinetics of

the electrochemical reaction within the anode.

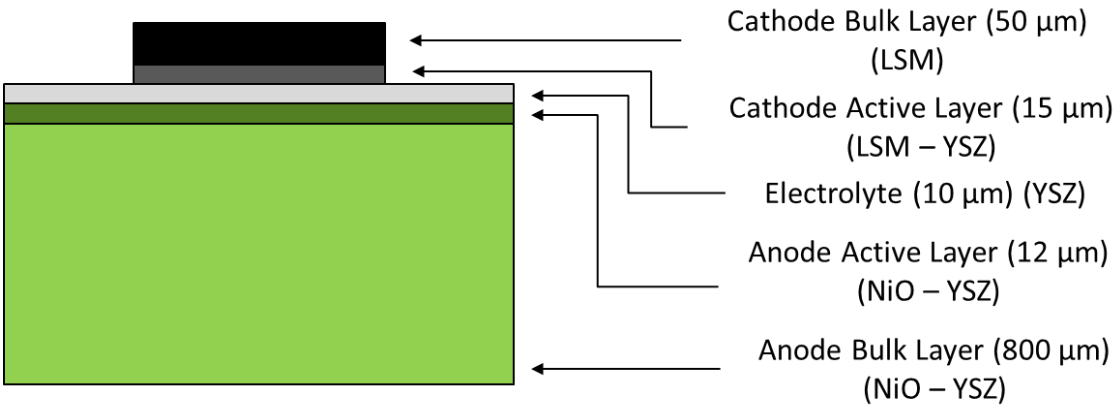

Figure 2: Cross section of an anode supported SOFC before anode reduction.

Electrochemical reactions in both the anode and the cathode require transport of three distinct species: molecular gas, electrons, and ions. Thus, the electrochemical reaction can only occur at regions where all of these are present. If three different phases are used, one for each species, this region is one-dimensional. These regions are called triple phase boundaries (TPBs). The TPB density, measured by the length of TPB per unit volume, is a critical metric for qualitatively understanding the performance of Ni-YSZ anodes and LSM-YSZ cathodes. In general, higher TPB densities within the anode result in increased performance [11,25,33,34]. TPB density, as well as other microstructural properties, can be controlled by changing the relative particles sizes of nickel and YSZ, the relative composition of the anode, as well as broader changes such as electrode architecture [9,11,22,35]. All of these changes are then reflected in the resulting electrochemical performance of the cell.

2.2 Electrochemical performance of solid oxide fuel cells

Solid oxide fuel cells are in essence an oxygen concentration sensor, with an internal resistance low enough to draw useful current from the electrochemical reactions at each electrode. The open circuit voltage (OCV) of the cell, which is the voltage of the cell without drawing any current, is also known as the Nernst potential and is calculated by the Nernst equation:

$$E_0 = \frac{RT}{4F} \ln\left(\frac{p_{O_2,c}}{p_{O_2,a}}\right) \quad (1)$$

where E_0 is the Nernst potential, R is the ideal gas constant, T is the cell temperature in Kelvin, F is Faraday's constant, $p_{O_2,c}$ is the oxygen partial pressure at the cathode, and $p_{O_2,a}$ is the oxygen partial pressure at the anode. The oxygen partial pressure at the cathode is usually between 1 atm and 0.01 atm. The oxygen partial pressure in the anode fuel gas mix, which for this study is H_2 and H_2O, is controlled by the equilibrium reaction between H_2¸ H_2O, and O_2:

$$2H_2 + O_2 = 2H_2O \quad (2)$$

The partial pressure of oxygen at a given temperature is then calculated using a known equilibrium constant, K_2:

$$p_{O_2,a} = \frac{p_{H_2O}^2}{K_2 . p_{H_2}^2} \quad (3)$$

As current is drawn from the cell, the voltage of the cell drops due to the resistance of the various cell processes. It is desirable to have the lowest possible overall cell resistance, as the drop in potential due to current causes the electrochemical efficiency, $\varepsilon_{Electrochemical}$, to decrease according to:

$$\varepsilon_{Electrochemical} = \frac{E_{Cell}}{E_0} \quad (4)$$

where E_{Cell} is the operating voltage of the cell at a given current. The difference between the cell operating voltage and the Nernst potential is referred to as the polarization or the overpotential of the cell. Reducing the resistance of the cell reduces the polarization of the cell at any given current, resulting in higher cell efficiency. Thus, it is desirable to minimize the resistance of any fuel cell to reduce cell polarization. Overall cell polarization is due to the summation of the polarizations from each cell process. Three types of polarizations dominate SOFC performance: Ohmic polarization, concentration polarization, and activation polarization. The cell operating voltage can be calculated at any given current density i by the following equation:

$$E_{cell} = E_0 - \eta_{Ohmic} - \eta_{conc} - \eta_{act} \quad (5)$$

These polarizations are described in detail in the following subsections.

2.2.1 Ohmic polarization

Ohmic polarization is due to the conduction of ions and electrons through the ionic and electronic conducting phases of the cell, respectively. The cell polarization due to Ohmic resistance at a given current is calculated very simply:

$$\eta_{Ohmic} = i \cdot R_{Ohmic} \quad (6)$$

where η_{Ohmic} is the Ohmic polarization of the cell in Volts, i is the current density, and R_{Ohmic} is the Ohmic resistance of the cell.

2.2.2 Concentration polarization

Concentration polarization is due to the concentration gradient of the product and reactant gasses through the porous electrodes of the SOFC. Cathodic concentration polarization, due to the diffusion of oxygen through the cathode electrode, is very small in anode-supported solid oxide fuel cells. This is because the cathode electrode is very thin, allowing for high currents to be drawn before any significant concentration gradient is established. Only when the partial pressure of oxygen in the cathode gas mixtures is less than about 10% does the cathodic concentration polarization become a significant contribution to overall cell polarization [36,37]. In this work, cells are not tested at such low cathodic oxygen partial pressures.

Anodic concentration polarization is caused by the diffusion of H_2 into the electrode and H_2O out of the electrode. Because the thickness of the anode in anode-supported cells is relatively large, the concentration gradients of H_2 and H_2O are significant even at low current densities. As current is increased, more fuel is consumed and more water vapor is produced at the anode-electrolyte interface, steepening the concentration gradients of H_2 and H_2O through the anode thickness. These concentration gradients are assumed to be linear [38], and can be calculated by:

$$p_{H_2}(x,i) = p_{H_2}^0\left(1 - \left(\frac{x}{x_a}\right)\left(\frac{i}{i_{limit,a}}\right)\right) \tag{7}$$

$$p_{H_2O}(x,i) = p_{H_2O}^0\left(1 + \left(\frac{p_{H_2}^0}{p_{H_2O}^0}\right)\left(\frac{x}{x_a}\right)\left(\frac{i}{i_{limit,a}}\right)\right) \tag{8}$$

where p_{H_2} and p_{H_2O} are the H_2 and H_2O partial pressures at a given position in the anode and at a specific current i, $p_{H_2}^0$ and $p_{H_2O}^0$ are the H_2 and H_2O partial pressures in the bulk

vapor phase, x_a is the thickness of the anode, and $i_{limit,a}$ is the anodic mass transfer limited current density. The anodic mass transfer limited current density is the current density at which all of the available hydrogen fuel is consumed. This is a very useful property for modeling the diffusion of hydrogen and water vapor through the anode, and can be calculated by [39]:

$$i_{limit,a} = \frac{2Fp_{H_2}^0 D_{H_2-H_2O,eff}}{RTx_a} \tag{9}$$

where $D_{H_2-H_2O,eff}$ is the effective diffusivity of the H_2-H_2O gas mixture in the anode. With the anodic mass transfer limited current density defined, the anodic concentration polarization can be simply calculated as [39]:

$$\eta_{conc,a} = -\frac{RT}{2F}\ln\left(1-\frac{i}{i_{limit,a}}\right)+\frac{RT}{2F}\ln\left(1+\frac{p_{H_2}^0}{p_{H_2O}^0}\frac{i}{i_{limit,a}}\right) \tag{10}$$

Upon modification of a Ni-YSZ cermet anode by infiltration, the anodic concentration polarization can only increase. This is because the infiltration process trades pore volume for infiltrant volume. This reduction of pore volume reduces gas phase diffusivity and increases the mass transfer resistance of the anode [36,40–43]. The relationship between electrode porosity and effective gas diffusivity can be calculated simply by [38]:

$$D_{H_2-H_2O,eff} = \frac{\varepsilon}{\tau} D_{H_2-H_2O,0} \tag{11}$$

where $D_{H_2-H_2O,0}$ is the binary gas diffusivity of the H_2-H_2O gas mixture, ε is the porosity of the electrode, and τ is the tortuosity of the electrode. So, any reduction in anode porosity results in an equal reduction of gas diffusivity within the electrode and of the anodic mass transfer limited current, resulting in increased anodic concentration

polarization. Thus, any infiltration procedure for Ni-YSZ cermet anodes needs to limit the total amount of infiltrant, which should minimize the negative impact of infiltration on the anodic concentration polarization.

2.2.3 Activation polarization

Activation polarization is due to the energy barriers of the charge transfer reactions in both the anode and cathode electrodes. The magnitude of this energy barrier is referred to as the activation energy, hence the term activation polarization. For electrochemical devices where mass transfer is rapid or the current is small, such as SOFCs, activation polarization is usually modeled by the Butler-Volmer equation, which can be rearranged to give the activation polarization [36,37]:

$$\eta_{act} = \frac{2RT}{nF} \ln\left(\frac{1}{2}\left(\left(\frac{i}{i_0}\right) + \sqrt{\left(\frac{i}{i_0}\right)^2 + 4}\right)\right) \tag{12}$$

where n is the number of electrons participating in the cell reaction and i_0 is the exchange current density, which is a measure of the catalytic activity of the overall electrochemical reaction. For solid oxide fuel cells, n can be equal to either 1 or 2, depending on what fits best with the experimental data, and can change based on the cell temperature or gas concentrations at either electrode [36,42–45]. This model also does not separately consider the activation polarization at the anode and the cathode.

The infiltration of nickel nanoparticles will reduce the activation polarization of the anode due to the increase of the TPB density within the anode active layer [11,25,33,46]. A very recently developed transmission-line-model of the electrochemical reaction within Ni-YSZ electrodes, which predicts the performance directly from the

microstructure of the electrode, determined that a three-fold increase in the TPB density results in a 55% decrease in the area specific resistance of the anode at 800°C in a 90% H_2 – 10% H_2O fuel gas mixture [34].

2.3 Measuring electrochemical performance of solid oxide fuel cells

2.3.1 Galvanostatic and potentiostatic testing

The electrochemical performance of SOFCs is most simply measured by galvanostatic or potentiostatic testing. In galvanostatic testing, a constant current is applied to the cell over time, and the voltage is measured. The simplest galvanostatic measurement is a measurement of the OCV over time, which is the cell voltage at zero current. While very straightforward, ensuring that the OCV of the cell is near the theoretical value as calculated by Equation 1 is critical for reliable measurement of cells [47–49]. Detailed analysis of the OCV over time can even be used for fault identification in commercial stacks [50]. Galvanostatic testing with applied current is commonly used to test cell degradation over long periods; the degradation in the voltage response over long times is often linear, and is reported in terms of percent drop per thousand hours [26,51–53]. Cell degradation is due to many possible degradation pathways, depending on the operating conditions of the cell [26,52–55].

In potentiostatic testing, the cell is held at a constant voltage and the resulting current is measured. This is similar to galvanostatic testing conceptually, but is not often used, because galvanically controlled measurements can be conducted with much more affordable electronics and are used to operate commercial scale stacks. With that being said, potentiostatic measurements can be very useful, because the oxygen partial

pressures at each electrode-electrolyte interface are determined by the applied potential, according to Equation 1. If a reference electrode is used for the voltage measurement on the working electrode side of the cell, the applied potential is a direct measurement of the oxygen partial pressure at the electrode-electrolyte interface of the counter electrode. This can be useful for measuring the behavior of materials near their metal-oxide equilibrium [23,56].

2.3.2 Current-voltage scans and fitting

A current-voltage (I-V) scan is a direct-current (DC) measurement used to measure the power output and resistance of a cell at a given current. I-V scans are conducted by sweeping the applied current from zero amps up to a given current density at a specified rate. The typical curvature of an I-V scan on an SOFC is shown in Figure 3; in this figure, the anode gas mixture is being varied, which causes a substantial change to the shape of the I-V curve. The curvature of the I-V scan also changes based on cell temperature and cathodic oxygen partial pressures. This is due to the changing contributions of the individual cell polarization when the cell testing environment is changed. The curvature of the I-V measurement can be utilized to conduct I-V fitting, which separates the individual cell polarizations from one another [36,57].

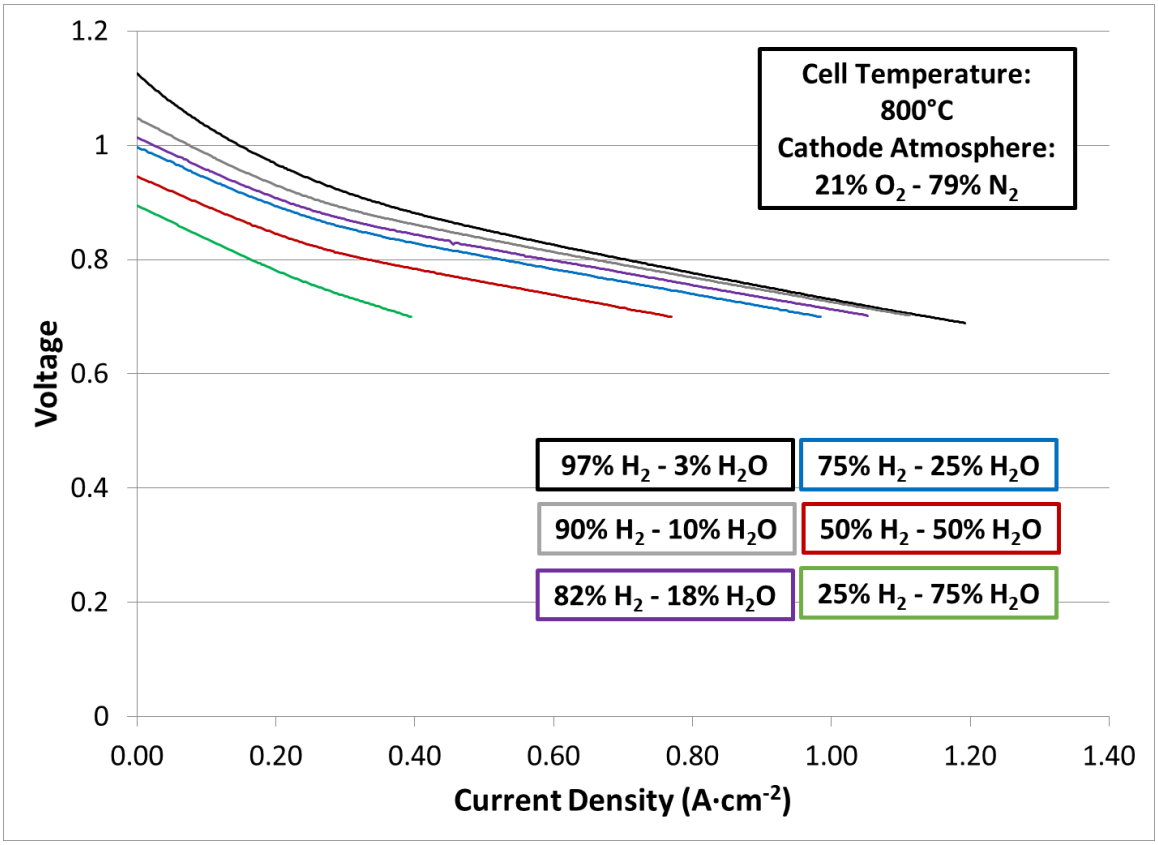

Figure 3: Typical I-V scans for an SOFC while varying the anode gas mixture.

The quality of I-V data fitting is greatly improved by a direct measurement of the anodic mass transfer limited current density. This can be done either by an out-of-cell diffusivity measurement of the Ni-YSZ cermet, or by conducting an I-V scan to low potentials while flowing 100% O_2 [57,58]. Flowing pure oxygen over the cathode ensures that there is no contribution of cathodic concentration polarization to the measurement. An example of I-V curves conducted to measure the anodic mass transfer limited current density are shown in Figure 4. It should be noted that operating cells at such high current densities is only possible for button cells, as stacks can suffer from fuel depletion and nickel oxidation in these conditions. Also, at low current densities, the I-V data is

representative of the stable galvanostatic response of the cell, while at very high currents this is not true [47]. An example of a fitted I-V scan from a conventional anode supported SOFC using this fitting procedure is shown in Figure 5. MATLAB programs for fitting I-V data (one setting the parameter n from Equation 12 to 1, the other to 2) is attached in Appendices 1 and 2, with an example run provided in Appendix 3. While I-V fitting is clearly useful for understanding the contributions of cell components to overall cell polarization, it is fundamentally limited in its ability to separate the unique contributions of the anode and cathode half-cell reactions to the activation polarization of the full cell.

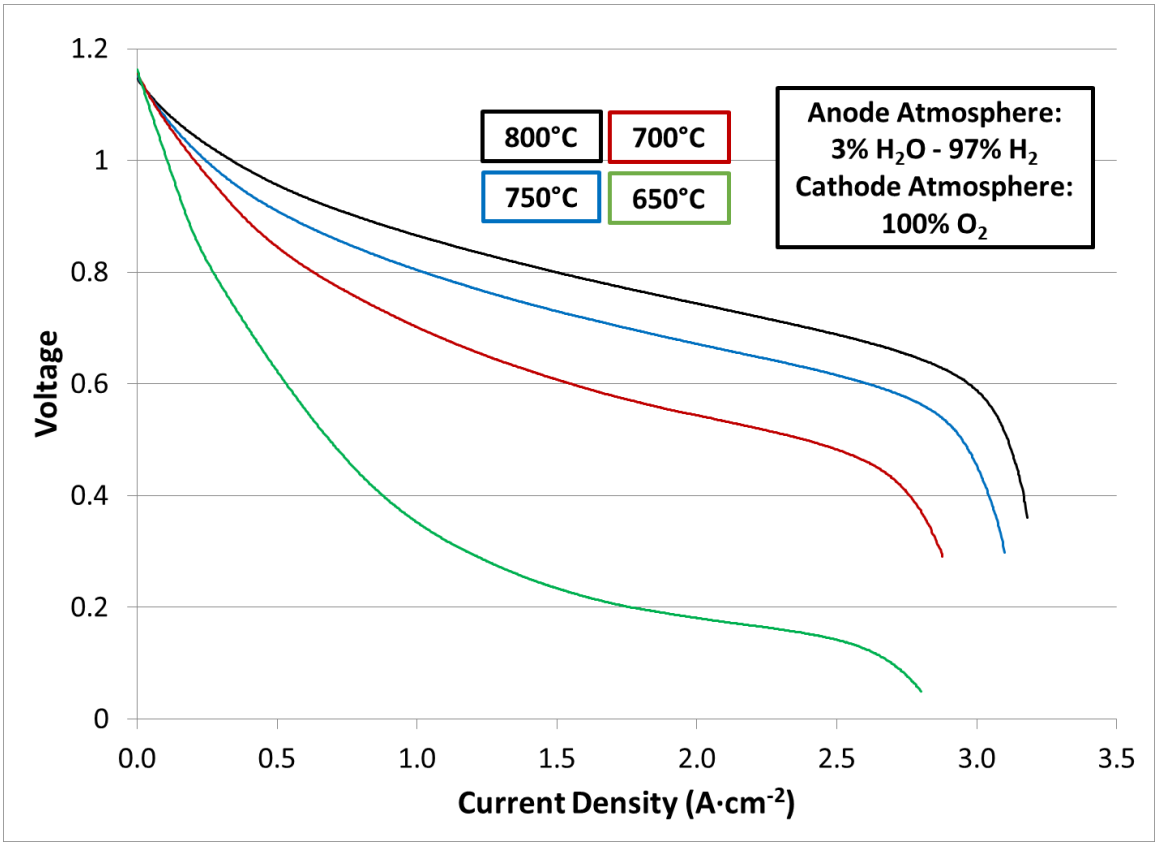

Figure 4: I-V scans conducted to low potentials for measurement of the anodic mass transfer limited current density.

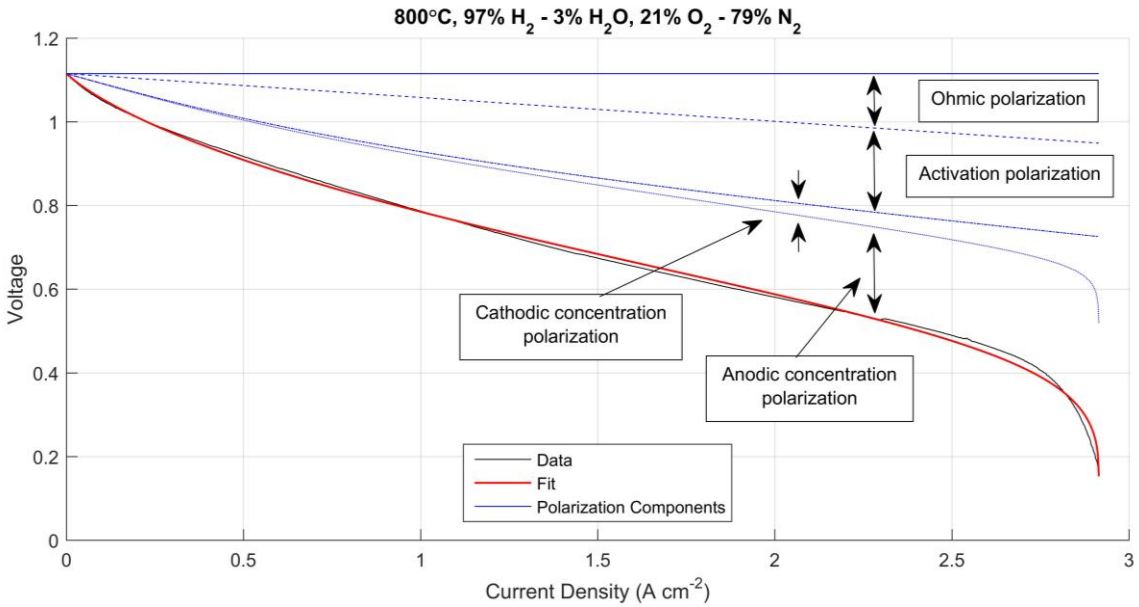

Figure 5: Example of a fitted I-V scan from a Ni-YSZ/YSZ/LSM-YSZ anode-supported SOFC.

2.3.3 Electrochemical impedance spectroscopy and fitting

Electrochemical impedance spectroscopy (EIS) is one of the most frequently used performance characterization techniques for SOFCs. EIS measurements are conducted by applying a small alternating-current (AC) perturbation to the cell and measuring the resulting response, which can have both a different amplitude as well as a phase-shift from the perturbation wave. This can be seen schematically in Figure 6 [1]. A full spectrum of impedance measurements is recorded by varying the frequency of the input AC signal across a wide range; SOFCs usually require a frequency range of 100 mHz to 1MHz to measure the full impedance response of a cell. Measurements can be conducted using either a current wave or a potential wave as inputs, with similar results.

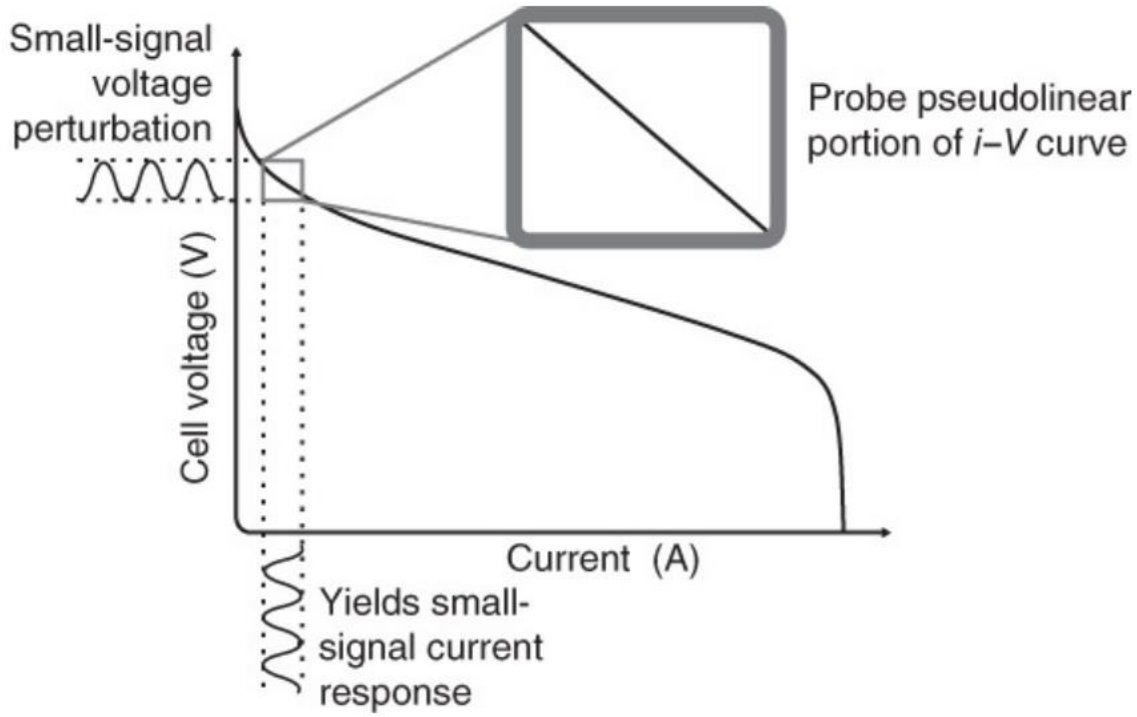

Figure 6: Schematic of the measurement of cell impedance [1].

EIS measurements are widely used because it is very simple to separate the Ohmic resistance and polarization resistances from one another. This can be clearly seen in a Nyquist plot, which is a plot of the real versus the imaginary components of the impedance, and is shown in the top plot of Figure 7. The leftmost intercept of the Z_{Real} axis is the Ohmic resistance of the cell, while the rightmost intercept of the Z_{Real} axis is the total resistance of the cell; the difference between the total and Ohmic resistances is the polarization resistance of the cell. The total resistance of the cell as measured by EIS is the same as the DC resistance measured by I-V. The variation of the impedance response with the AC frequency of the perturbation is more clearly seen in a Bode plot, which is a plot of the imaginary component of the impedance versus the frequency, and is shown in the bottom plot of Figure 7.

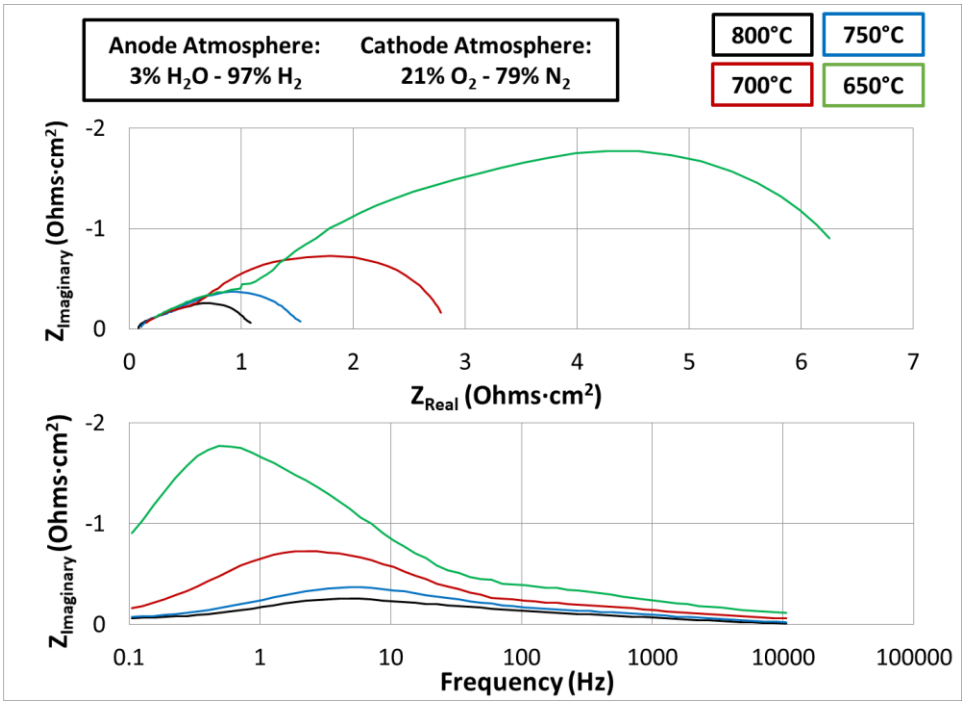

Figure 7: Typical EIS response from an SOFC at varying temperatures.

Just as I-V data can be fit with a polarization model to separate the individual cell polarizations, EIS data can be fit to separate the contributions of individual cell processes to the overall impedance measurement. In order to do this, each cell process needs to be represented by an equivalent circuit element, which are added together to make an equivalent circuit model (ECM). The selection of the equivalent circuit model is critically important for achieving a physically relevant fit, and has been the subject of substantial research [34,37,42,43,45,47,59–66]. In many recent works, the use of the distribution of relaxation times (DRT) transformation has been utilized to help identify individual cell processes from EIS data [34,44,63–65,67–72]. This powerful technique dramatically improves the separation of the processes compared to analysis of Bode plots, but cannot be relied upon exclusively to deconvolute cell processes; results are very sensitive to initial data quality, and several mathematical transforms are possible, all with

qualitatively different results [64,65,72–75].

In this research, the ECM developed by Leonide et al. has been used, because this model was developed for cells with very similar architecture to those used in this research [44]. This model is reproduced below in Figure 8. The highest frequency responses are on the left, and the lowest frequency responses are on the right. Each element corresponds with a physical process within the cell: R_{Ohmic} is the Ohmic resistance, the two parallel RQ elements model the anodic charge transfer resistance, the Gerischer (Ge) element models the cathodic charge transfer resistance, and the finite-length Warburg (FLW) element models the anodic gas diffusion. An additional parallel RQ element can be used to model cathodic gas diffusion when very low oxygen partial pressures are used at the cathode, but this condition was not relevant to this work.

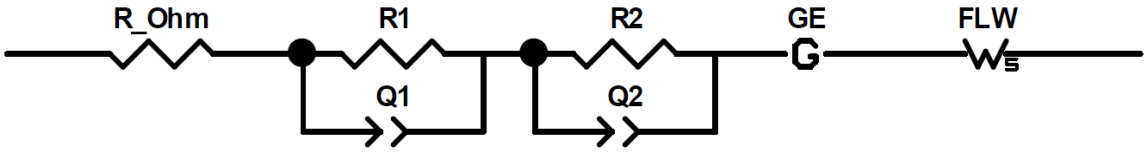

Figure 8: ECM for anode-supported SOFCs utilizing Ni-YSZ anodes, thin YSZ electrolytes, and thin composite cathodes [37]**.**

Even with a suitable ECM, the impedance of individual processes can overlap substantially at certain experimental conditions. And because there are many free parameters in the ECM, it is possible to achieve a high-quality fit that has no physical relevance. To practically separate these impedance responses, EIS measurements need to be recorded under a wide range of cell temperatures, anode fuel gas mixtures, and cathode fuel gas mixtures. After recording measurements, the accuracy of the fit can be ensured by batch fitting [62,66]. Measurement quality is also critically important to EIS

data fitting, and can be easily checked utilizing the linear Kramers-Kronig relationship with freely available software such as Lin-KK [70,76–78]. These prior works were used as the basis for fitting of EIS data used in this work. An example of a fitted EIS measurement utilizing these methods is shown in Figure 9. More detail on the practical execution of EIS fitting is detailed in Section 4.3.

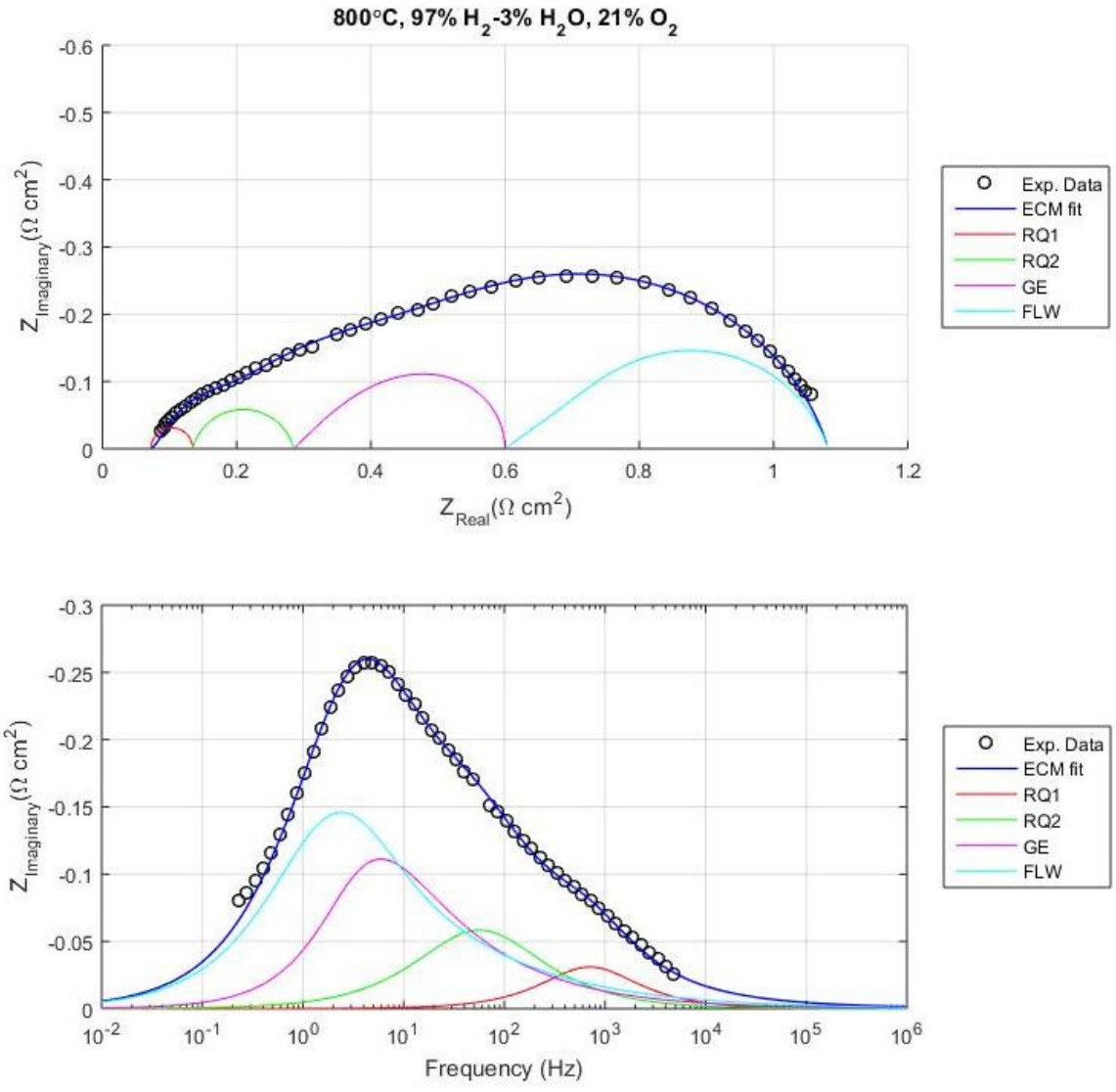

Figure 9: Example of a fitted EIS measurement from a Ni-YSZ/YSZ/LSM-YSZ anode-supported SOFC.

2.4 Infiltration of nickel nanoparticles into solid oxide fuel cell anodes

Liquid infiltration is a simple and controllable method for introducing nanoparticle into porous substrates, and has been extensively researched for improving both the fuel and oxygen electrodes of SOFCs. Several review articles have been published detailing the effect of different infiltrated materials on electrode performance [6,7,79,80]. While many different materials can feasibly be infiltrated into SOFC electrodes, studying the infiltration of nickel is of great interest because of nickel's high catalytic activity, relative affordability compared to precious metal catalysts, and stability with YSZ. This section will briefly summarize the performance and stability of infiltrated nickel nanoparticles and methods for depositing nickel nanoparticles.

Infiltration of nickel enables the manufacturing of the electrode at much lower temperatures than are required for conventional sintering, allowing for the production of nanoscale features that would be unstable at sintering temperatures [81]. New SOFC anode architectures have been developed by utilizing infiltration to deposit all of the required nickel within a porous ceramic substrate. These electrodes have three key advantages over conventional Ni-YSZ cermets: lower nickel content, improved redox tolerance, and better initial performance. Nickel infiltrated YSZ substrates require lower nickel content than Ni-YSZ cermets because infiltrated nickel only needs to connect on the surface of YSZ grains, essentially a 2-D surface, while the nickel in Ni-YSZ cermets needs to connect in three dimensions. This means than infiltrated nickel is percolated at about 9 vol. %, while Ni-YSZ requires about 30 vol. % to percolate [22,82]. This reduction of nickel volume reduces material costs, and also is the reason for improved

redox tolerance. During redox cycles of SOFCs, the nickel oxidizes, resulting in a 34% increase in volume. In traditional Ni-YSZ cermets, this volume expansion forms cracks and dramatically reduces cell performance, while electrodes produced by infiltration of nickel into a porous ceramic substrate show much better stability [12,83].

Performance improvement is due to the smaller feature size of infiltrated nickel structures compared to that of conventionally sintered Ni-YSZ cermets. Infiltrated nickel nanoparticles have feature sizes of about 100 nm, compared to the average feature size in Ni-YSZ cermets, which is about 1 μm. Thus, infiltrated nickel electrodes have TPB densities of around 10-30 μm μm^{-3}, compared to 1-10 μm μm^{-3} for Ni-YSZ cermets [11–13,25,84]. Hua et al. measured a 72% reduction (5 $\Omega \cdot cm^2$ for Ni-YSZ vs. 1.4 $\Omega \cdot cm^2$ for the infiltrated electrode) in anode resistance at 700°C while flowing pure H_2 when comparing a conventionally produced anode to a nickel and YSZ infiltrated YSZ substrate with the same geometry [13].

While the performance of infiltrated nickel electrodes is very good, the performance stability is not. While Ni-YSZ cermet anodes have stable electrochemical performance for thousands of hours at operating temperatures, the performance of infiltrated nickel electrodes degrades rapidly within the first 100 hours of operation [33,85]. This is attributed to the smaller features of infiltrated nickel electrodes, which rapidly coarsen during operation, while Ni-YSZ cermets coarsen much more slowly. The coarsening behavior of infiltrated nickel in porous substrates not only reduces the TPB density of the electrode, but also lowers its electrical conductivity [10,22,82]. Simultaneous infiltration of nickel with sintering inhibitors, such as YSZ and GDC,

improves the stability of infiltrated nickel [82].

The most commonly utilized method for liquid infiltration of nickel nanoparticles into a porous substrate is to simply dissolve a nickel nitrate salt ($Ni(NO_3)_2$) into a solvent, infiltrate the resulting solution into the substrate, then evaporate the solvent and decompose the nickel nitrate into nickel oxide in a furnace. The key properties of the infiltration solution are the solvent choice, the metal ion concentration, surfactant or chelating agent selection and concentration, and the viscosity of the resulting solution. Published work includes infiltration solutions utilizing water, ethanol, and ethylene glycol as solvents [21,86–89]. The molarity of the metal cations in solution can be varied over a wide range of concentrations based on the desired results, though usually researchers aim to use as high a metal cation concentration as possible to minimize the number of infiltration cycles required. Various works also include additional organic chemicals, such as citric acid, urea, and surfactants, which change the precipitation and evaporation behavior of the solution [14,90–92]. Increasing the concentration of dissolved ions in the infiltration solution increases the viscosity, which needs to be kept low enough to penetrate the porous substrate. Penetration of the infiltration solution into the porous substrate can be aided by reducing the solution viscosity and/or surface tension. This can be done chemically by the addition of surfactants, or physically by heating the solution or infiltrating in a vacuum. For more detail on the interplay between these variables, see recently published works by Yoon et al. and Dowd Jr. et al. [90,92]. Research has also been conducted on alternative infiltration techniques, such as microwave-assisted infiltration and metal plating via the Tollens reaction, but these

techniques have not been thoroughly explored, and are not utilized in this work [93–96].

2.5 Approaches for activating infiltrated nickel nanoparticles

Despite the substantial performance improvement due to nickel infiltration and the relative ease of execution, infiltration of nickel into Ni-YSZ cermets has been little explored. The possible reasons behind this lack of research were discussed previously in Section 1. So, this work aims to explore nickel infiltration of Ni-YSZ anodes as a cheap and simple method for improving SOFC anode performance. However, unless a substantial volume of nickel is infiltrated into the Ni-YSZ cermet, nickel nanoparticles will not connect with one another, and are thus not fully utilized. Two different approaches are proposed for activating the infiltrated nickel nanoparticles in Ni-YSZ cermets: in-situ spreading of nickel nanoparticles, and simultaneous infiltration of nickel with a conducting oxide.

2.5.1 In-situ spreading of nickel nanoparticles

Recent work by Jiao and Shikazono has demonstrated the dramatic impact that the electrochemical potential has on the morphology of nickel in SOFCs [23,97]. Specifically, when nickel on YSZ is exposed to low potentials, the equilibrium contact angle between nickel and YSZ decreases, causing nickel to spread. This effect was experimentally observed, and a thermodynamic model was also developed to model the contact angle as a function of the fuel gas mix humidity. The results of this thermodynamic model, with new calculations done for 750°C and 700°C, are shown in Figure 10. The Ni-YSZ contact angle decreases with increasing fuel gas mix humidity. This is because the surface tension of nickel decreases with increasing oxygen activity,

which increases dramatically at high humidity according to Equation 3. Oxygen activity actually does not discernably increase until the humidity in the fuel gas mix exceeds 80%. Correspondingly, the Ni-YSZ contact angle does not fall below 90° until the humidity is 95% at 800°C. As the humidity increases beyond 95%, the contact angle decreases rapidly. This implies that at 800°C, infiltrated nickel nanoparticle will spread quickly if the humidity exceeds 95%. At lower temperatures or lower humidity, though, nickel spreading will likely be negligible. Extrapolating these results to temperatures lower than 700°C, it is clear that nickel nanoparticles will not reach contact angles less than 80°, suggesting that they will not spread even at extreme humidity. At humidities higher than those shown in Figure 10 (> 99.4% H_2O at 800°C), nickel oxidizes, which likely causes nickel nanoparticles to coarsen upon later reduction.

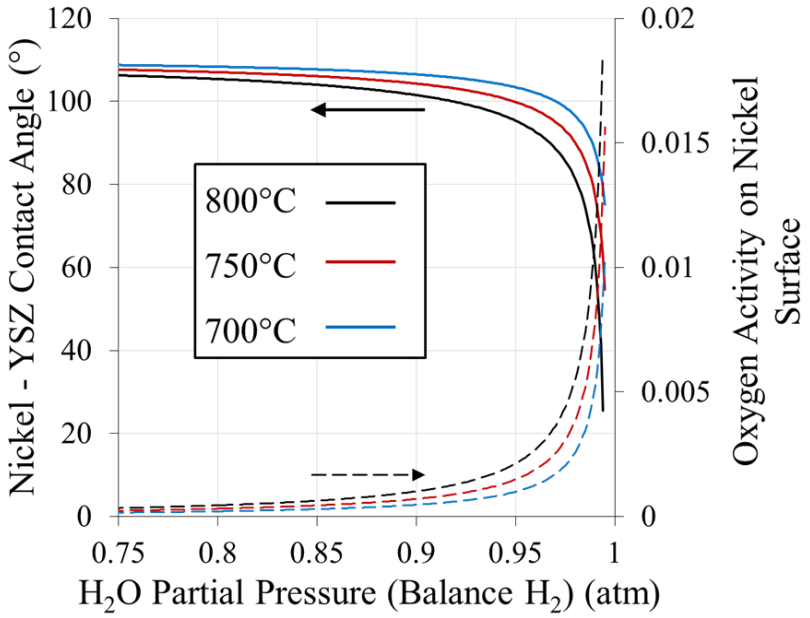

Figure 10: Contact angle between nickel and YSZ (solid lines) as function of the fuel gas mix humidity. Oxygen activity at the nickel surface (dotted lines) is directly related to the fuel gas mix humidity, shown on the secondary axis.

Assuming linear concentration gradients, the partial pressures of H_2 and H_2O at the anode-electrolyte interface can be estimated at any current density and bulk vapor concentrations of H_2 and H_2O [38]. The concentration gradients of hydrogen and water vapor in Figure 11 are calculated using Equations 7 and 8 assuming an initial gas mix of 50% H_2 – 50% H_2O with the current density i equal to $i_{limit,a}$. It is clear from Figure 11 that when the current density approaches the anodic mass transfer limited current density, a maximum of 10% of the anode's thickness is exposed to water vapor concentrations greater than 95%. This localizes nickel spreading to just a small region near the anode-electrolyte interface. At current densities less than 95% of the anodic limiting current density, the humidity at the anode-electrolyte interface is always less than 95%, and thus infiltrated nickel nanoparticles do not spread.

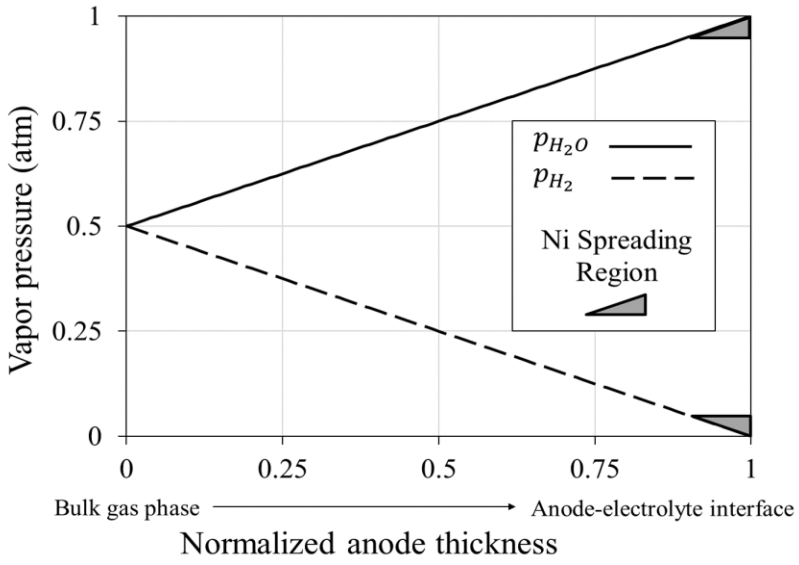

Figure 11: Concentration gradients of water vapor and hydrogen through the anode thickness during the application of anodic mass transfer limited current

During electrochemical testing, a dramatic increase in cell polarization at high current densities indicates that the anodic mass transfer limited current density has been

reached. This is due to the increase of the anodic concentration polarization when almost all the hydrogen has been consumed at the anode-electrolyte interface. Figure 12 shows the variation of the anodic concentration polarization as a function of the current density relative to the anodic mass transfer limited current density. In conditions with low bulk water vapor partial pressure, anodic concentration polarization increases quickly before slowing to a linear increase. This continues until the current density reaches about 90% of the limiting current density, at which point the polarization increases dramatically, thereby causing the cell potential to fall drastically. When the bulk water vapor content is high, the anodic concentration polarization is initially less and increases linearly at a slower rate, until the current density reaches about 90% of the limiting current density, and then the concentration polarization again increases dramatically, causing cell potential to fall.

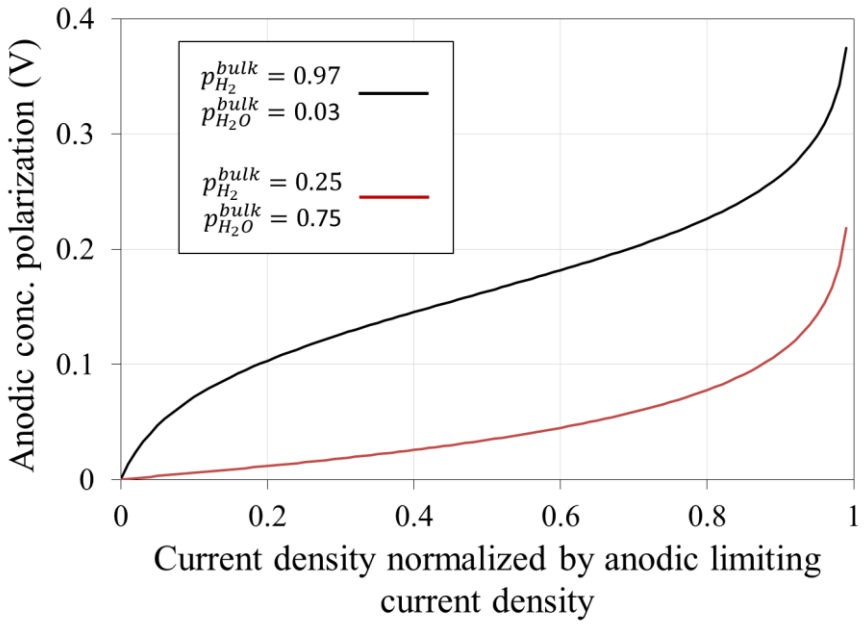

Figure 12: Anodic concentration polarization versus the current density, normalized versus the limiting current density.

Thus, from the previous descriptions, it is clear that the humidity at the anode-electrolyte interface, the current density, and the cell potential are all intrinsically linked. For this research, the terms high current density, high humidity at the anode-electrolyte interface, and low cell potential are all synonymous. Cells tested at high current densities have been exposed to high humidity at the anode-electrolyte interface, leading to low cell potentials; cells maintained at low current densities have only been exposed to low humidity at the anode-electrolyte interface and kept at high potentials. In this work, 'high humidity' corresponds to conditions where the humidity at the anode-electrolyte interface is higher than 95%, and 'low humidity' corresponds to conditions less humid. 'Extreme humidity' occurs when the cell potential is allowed to drop to 0 mV, indicating that the anodic limiting current density has been reached, resulting in near 100% water vapor at the anode-electrolyte interface.

2.5.2 Simultaneous infiltration of nickel with a conducting oxide

By infiltrating nickel simultaneously with a conducting oxide into Ni-YSZ cermet anodes, nickel nanoparticles can be connected to one another and to the percolated nickel network of the Ni-YSZ cermet without needing to be spread. Additionally, the oxide nanoparticles should also serve to stabilize nickel nanoparticles by physically constraining them. The most successful oxide for utilizing nickel nanoparticles in SOFC anodes has been GDC. At 800°C in 97% H_2 – 3% H_2O gas, GDC is a mixed ionic-electronic conductor, with a conductivity of about 1 $S \cdot cm^{-1}$ and an electronic transference number of about 50% [1,98]. This electronic conductivity is not very high compared to the conductivity of the Ni-YSZ cermet electrode (about 1000 $S \cdot cm^{-1}$), but the ionic

conductivity of GDC is about 1 order of magnitude higher than that of YSZ [1,98]. This allows GDC to conduct both ions and electrons across the short distances between nickel nanoparticles. GDC also improves the ionic conductivity of the electrode slightly, extending the distance that oxygen ions can travel before reacting [34,99]. This improves cell performance, because more TPBs are available for the electrochemical reaction. Additionally, GDC alone can serve as a catalyst for the electrochemical oxidation of hydrogen, reacting H_2 with oxygen ions and producing electrons anywhere on its surface [100].

Prior research on the simultaneous infiltration of nickel and GDC is promising. As mentioned previously, the infiltration of GDC improved the stability of infiltrated nickel nanoparticles [82,101]. The combination of nanoscale nickel and GDC catalysts has also been shown to perform better than either material alone in several different cell architectures [101–103]. Even when nanoscale features aren't used, the activation energy of the electrochemical oxidation of hydrogen in SOFC anodes is lower in anodes with nickel and GDC than in anodes with nickel and YSZ. Studies of anodes with nickel and GDC show an activation energy of between 0.5 eV to 0.85 eV [46,100,101,103–106]. This can be comparted to the activation energy of anodes with nickel and YSZ, which is reported as being between 1.1 eV to 1.8 eV by full cell measurements, model anode studies, and first-principles calculations using density-functional theory [34,37,107–109]. Because of the lower activation energy, anodes with nickel and GDC should have much better catalytic activity at low temperatures than anodes with nickel and YSZ.

The only previous work on simultaneous infiltration of nickel and GDC into Ni-

YSZ cermet anodes was reported in a study conducted at Haldor Topsøe A/S [21]. This study did not measured any gain in cell performance after anode infiltrated with nickel and GDC, but this work also does not report on the amount of infiltrant in the electrode, making replication difficult [21]. However, later work by some of the same researchers measured a dramatic improvement in anode performance after infiltration of copper and GDC [89]. They also measured the effect of infiltrating only GDC into the electrode, which demonstrated less performance improvement than the simultaneous infiltration of GDC and copper. This result qualitatively agrees with the results of other researchers, who studied the effect of GDC and Ni-GDC infiltration on metal-supported SOFCs using stainless steel – YSZ cermet anode active layers [101,102]. Recent work by Wang et al. has also demonstrated that simultaneous infiltration of 20% samarium doped ceria and nickel in metal supported SOFCs using stainless steel – YSZ cermets results in high electrode performance [110]. These works show that there is promise for Ni-GDC infiltration into Ni-YSZ cermet anodes.

3. ACTIVATION OF NICKEL NANOPARTICLES BY IN-SITU NICKEL SPREADING

In order to study the effect of high humidity on the morphology and electrochemical performance of Ni-YSZ anodes infiltrated with nickel nanoparticles, a testing plan was developed that exposes cells to different conditions at the anode-electrolyte interface. By comparing the performance of infiltrated anodes after nickel spreading at high humidity to that of infiltrated anodes without spreading, the impact of nickel spreading on the performance of nickel infiltrated cells can be studied. This section describes the preparation of cells before testing, the electrochemical testing apparatus and procedures, the results of electrochemical performance measurement, and the microstructure of cells after testing. A model describing the effect of nickel spreading on the performance of nickel infiltrated Ni-YSZ cermet anodes is then proposed based on the experimental results.

3.1 Methods and materials

3.1.1 Cell preparation

Anode-supported button cells have been purchased from Materials and Systems Research, Inc. (MSRI). Anode-supported button cells are composed of an 800 μm thick, 2.74 cm diameter NiO-YSZ anode bulk layer, a 12 μm thick NiO-YSZ anode active layer, and a 10 μm thick YSZ electrolyte. The testing conditions for several groups of cells are shown in Table 1. Cathodes for Group A were screen printed on to the electrolyte, composed of a 15 μm thick, 1.7 cm diameter LSM-YSZ cathode active layer and a 50 μm thick LSM cathode bulk layer. Cathodes from group B and C were screen

Test Temperature	Group A: Low Humidity		
	Uninfiltrated Cell A	Infiltrated Cell A1	Infiltrated Cell A2
750°C	X	X	
700°C	X		X
650°C	X		X
Test Temperature	**Group B: High Humidity**		
	Uninfiltrated Cell B	Infiltrated Cell B1	Infiltrated Cell B2
800°C	X	X	
700°C	X		X
600°C	X		X
Test Temperature	**Group C: Extreme Humidity**		
	Infiltrated Cell C1		
800°C	X		

Table 1: Cell nomenclature and electrochemical testing conditions.

printed by MSRI with the same dimensions as above, and used as purchased.

Before testing or infiltration, the as-purchased NiO-YSZ electrodes were reduced to Ni-YSZ by loading the cells into a furnace between two sealed Al_2O_3 tubes and heated to 800°C at 1°C·min^{-1}. Once at temperature, the anode was reduced by flowing 300 cm^3·min^{-1} of 95% Ar – 5% H_2 on the anode side for 12 hours, while flowing 1 L·min^{-1} of air over the cathode to protect it from any reducing gases. The apparatus was then cooled to room temperature while continuing gas flow. Electrochemical performance of one cell in groups A and B were measured after NiO reduction but without infiltration.

Other cells in each group were infiltrated before electrochemical testing. Ni-YSZ electrodes were infiltrated using repeated cycles of vacuum infiltration of an aqueous nickel nitrate solution. The aqueous $Ni(NO_3)_2$ solution was prepared by stirring 23 g

nickel nitrate (Chemsavers, 99.9%), 1.8 mL Triton-X 100 (Talas) and 20 mL distilled water at 90°C. The electrode was then infiltrated with the solution in a vacuum flask at 5 mbar absolute pressure. After letting the solution sit for 30 seconds, excess solution was wiped off the electrode surface to avoid blocking pores during further rounds of infiltration. After infiltration, the cell was heated to 100°C at 2°C·min^{-1} and held for 20 minutes to evaporate water, heated to 320°C at 2°C·min^{-1} and held for 20 minutes to decompose $Ni(NO_3)_2$ to NiO, then cooled to room temperature for further infiltration cycles. Five infiltration cycles were used in this research, resulting in the infiltration of an additional 3-4 wt. % nickel, compared to the overall initial cell weight. An example microstructure of an untested cell after nickel nanoparticle infiltration is shown in Figure 13.

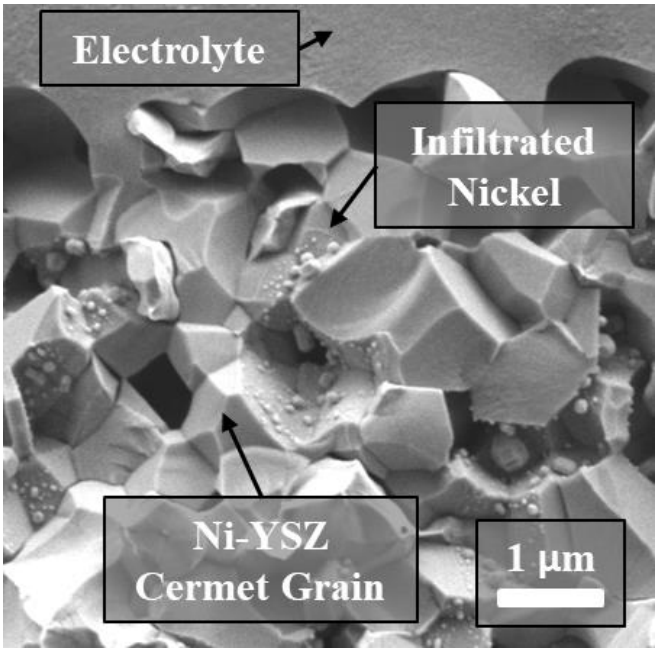

Figure 13: Anode active layer of a nickel nanoparticle infiltrated Ni-YSZ cermet after exposure to 5% H2 – 95% Ar at 800°C

3.1.2 Electrochemical testing preparation and apparatus

To prepare for electrochemical testing, metallic meshes were attached to the electrodes using conductive inks. Nickel ink (Fuel Cell Materials) was used to attach the nickel mesh (Alfa Aesar, 99.5%) to the anode, and silver ink (Alfa Aesar) was used to attach the silver mesh (Alfa Aesar, 99.9%) to the cathode. Nickel lead wires (Alfa Aesar, 99.55) and silver lead wires (Alfa Aesar, 99.9%) were attached to the nickel and silver meshes, respectively. The cell was then loaded into the electrochemical test stand, shown in Figure 14. This electrochemical test stand was developed to effectively seal both the anode and cathode sides of the cell, while putting minimal mechanical load onto the cell. This prevents any issues that might occur if high mechanical load is placed onto the pre-reduced anode, which has much lower mechanical strength than the NiO-YSZ composite. The cell is loaded between an Al_2O_3 tube and a machined Al_2O_3 plate with mica gaskets above and below the cell. The whole assembly is then lightly compressed using springs attached to the Al_2O_3 alignment rods on both the cathode and anode sides. A sealing glass paste (Fuel Cell Store) was applied around the edges of the cell to ensure a leak-proof gas seal. A K-type thermocouple placed approximately 1 cm away from the cell was used to measure the cell temperature.

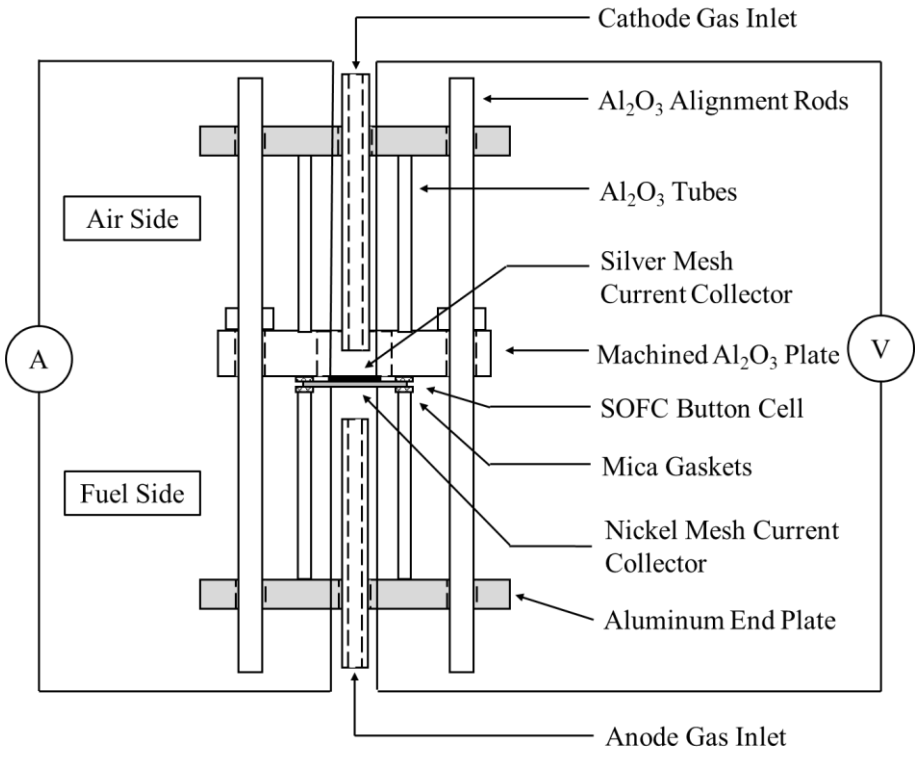

Figure 14: Schematic of the electrochemical testing stand.

3.1.3 Electrochemical testing procedure

The electrochemical test stand was then heated to 800°C at 1°C·min^{-1} inside a vertical clamshell tube furnace, and held for 12 hours to cure the glass paste. 300 cm^3·min^{-1} of 95% Ar – 5% H_2 was flowed on the anode side and 1 L·min^{-1} of air was flowed on the cathode side during heat up. Before testing, an electrochemical pretesting procedure was conducted. To ensure the quality of the gas seal, the OCV was monitored for 24 hours. Next, performance stability was ensured by applying 0.5 A·cm^{-2} current at 800°C for 24 hours or until the cell performance was constant. Electrochemical performance was measured using a Parstat 2273A potentiostat and impedance analyzer (Ametek, Inc.) with a Kepco power booster.

After the electrochemical pretesting procedure, the cell temperature was changed to the desired testing temperature at $1°C \cdot min^{-1}$. Testing temperatures for all cells tested are shown in Table 1. Performance was measured using I-V scans conducted galvanodynamically at a rate of $5\ mA \cdot s^{-1}$, and EIS measurements conducted with a 30 mV AC wave between 35 mHz – 105 kHz. Cells from "Group A: Low Humidity" were never exposed to anodic mass transfer limited current densities during all measurements to prevent exposure to high humidity. Cells from "Group B: High Humidity" were measured until the anodic limiting current density was clearly approached, approximately 400 mV at 800°C. The cell from "Group C: Extreme Humidity" was measured down to 0 V potential, exposing the anode active layer to nearly 100% H_2O.

Measurements were recorded at several cathode oxygen contents and several anode fuel gas mixes. Cathode oxygen concentrations for testing were pure O_2 and dry air (21% O_2). Cathode gas was dried using a desiccant before it entered the test stand. The anode fuel gas mixture was varied between 97% H_2 – 3% H_2O and 25% H_2 – 75% H_2O, with measurements recorded at several gas mixtures in between. Hydrogen was humidified using gas washing bottles filled with water and submerged in a heated water bath. Gas lines after the water bath were heated to 130°C to avoid condensation of water within the tube. Water bath temperature and cell OCV were both monitored to measure gas humidity.

Before measuring performance with 21% O_2 on the cathode, a 'nickel spreading procedure' was conducted using I-V scans with 100% O_2 on the cathode and 97% H_2 – 3% H_2O on the anode. This was done so that the contribution of cathodic diffusion to

overall cell polarization could be safely neglected. Thus, as the current density increases, any dramatic decrease in cell potential is due to anodic concentration polarization. In this way, the exposure of infiltrated nickel nanoparticles to humidity before further characterization is easily controlled. During this procedure, cells from Group A never experience high humidity, as the anodic mass transfer limited current density is never reached. Cells from Group B were tested down to 400 mV, at which point the anodic mass transfer limiting current density has clearly been reached, exposing nickel nanoparticles in the anode active layer to high humidity. Infiltrated cell C1 was measured down to 0 V, exposing infiltrated nickel nanoparticles to nearly 100% H_2O. Thus, all subsequent I-V represent cell performance after nickel nanoparticles have been modified by exposure to different humidities.

3.1.4 Microstructural characterization

Microstructural characterization of the Ni-YSZ cermet anode before infiltration was conducted using dual focused ion beam sectioning and 3D digital reconstruction. The 3D model of the anode can then be used to measure the TPB length, the volume of nickel, YSZ, and pore phases, and the tortuosity of each phase. These properties can be later used to correlate the microstructure of the anode with the electrochemical performance.

Additional characterization of nickel nanoparticle infiltrated anodes was conducted using analysis of images of fracture cross-sections, captured by scanning electron microscope (SEM) before and after electrochemical testing. This was done to measure the size, density, volume, and added TPB of infiltrated nickel nanoparticles. Particle size can be described both by the median and the average: an increase in the

median shows that the population of very small nickel nanoparticles is substantially decreased, while an increase in the average shows that particle size is larger overall. A decrease in particle density shows that nanoparticles have either coarsened together or coarsened with the nickel grains during testing. These properties can be used to compare the effects of electrochemical testing on nickel nanoparticles, as well as be compared to the properties of the Ni-YSZ cermet before infiltration.

These characterization methods, crucial for this work, were developed and implemented by Yanchen Lu [111].

3.2 Performance of uninfiltrated and nickel infiltrated cells without nickel spreading – Group A

The electrochemical performance of the uninfiltrated and infiltrated cells from Group A is shown in Figure 15. It is immediately clear that there is no performance improvement when comparing the performance of infiltrated cells with the uninfiltrated cell. Infiltrated cell A1 showed almost identical performance compared to un-infiltrated cell A at 750°C, while infiltrated cell A2 showed slightly worse performance than the uninfiltrated cell at 700°C and 650°C. It appears that the infiltration procedure may have adversely impacted infiltrated cell A2 and caused the observed degradation in performance.

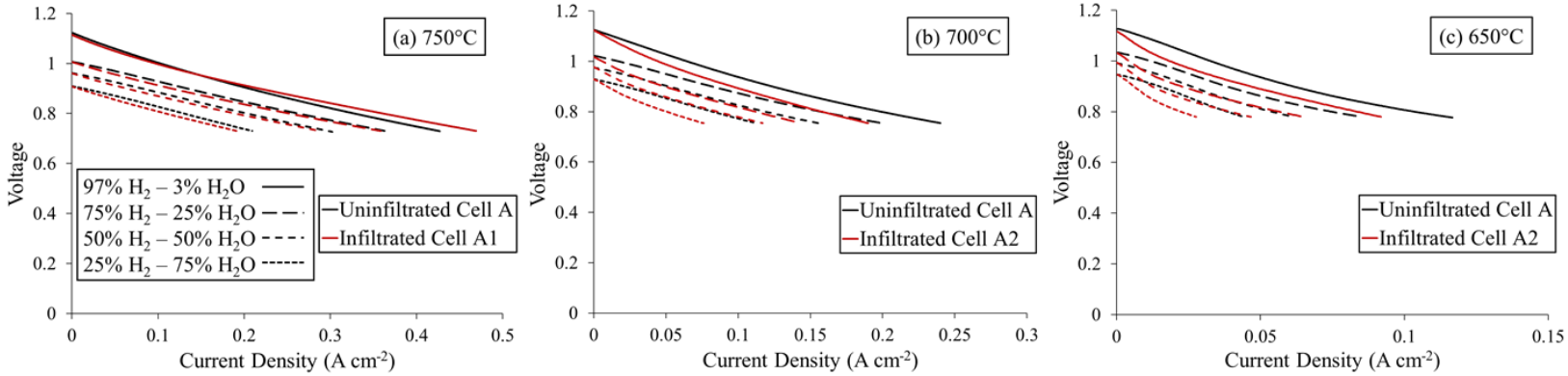

Figure 15: Electrochemical performance of Group A cells with 21% O2 on the cathode while varying the anode gas mix humidity at (a) 750°C, (b) 700°C, and (c) 650°C.

This result is attributed to the lack of connectivity between nickel nanoparticles without any spreading. Because the minimum potential observed by the cell is only 700 mV, and the maximum current density less than 1 $A \cdot cm^{-2}$, nickel nanoparticles in the anode active layer would only experience humidities near 30% according to Equations 7 and 8 (assuming that the anodic mass transfer limit is near 3 $A \cdot cm^{-2}$, as it is for other cells from MSRI). After exposure to 30% humidity, nickel nanoparticles will have no discernable change according to the nickel spreading model that was previously plotted in Figure 10, and are still not connected with one another.

3.3 Performance of uninfiltrated and nickel infiltrated cells with nickel spreading – Groups B and C

The electrochemical performance of the uninfiltrated and infiltrated cells from Group B is shown in Figure 16. Before performance measurements, Uninfiltrated Cell B, Infiltrated Cell B1, and Infiltrated Cell C1 have been all exposed to the nickel spreading procedure at 800°C, while Infiltrated Cell B2 has been exposed to the nickel spreading procedure at 700°C. Comparing the performance of Uninfiltrated Cell B to Infiltrated Cell B1 and B2, there is a clear performance improvement at all temperatures, with the improvement increasing as temperature is reduced. At 800°C, shown in Figure 16a, the performance of the Infiltrated Cell B1 compared to Uninfiltrated Cell B continues to improve until the cell reaches its maximum power density just before hitting the anodic mass transfer limited current density, after which the polarization increases rapidly, causing a sharp drop in the power density. The improvement in maximum power density

due to nickel infiltration after nickel spreading at 800°C is 18.8%, as reported in Table 2.

At lower temperatures, the performance of Uninfiltrated Cell B is compared with that of Infiltrated Cell B2. At 700°C and 600°C, shown in Figure 16b and Figure 16c respectively, no obvious mass transfer limit is ever reached, implying that the maximum power density is limited by charge transfer kinetics. This corresponds with an improvement in maximum power density as cell temperature is reduced, as reported in Table 2. This is indicative of an improvement in the anodic charge transfer kinetics, which have a larger impact on cell performance at lower operating temperatures. This improvement is due to the connection of nickel nanoparticles to one another by the nickel spreading procedure, which activates their TPB.

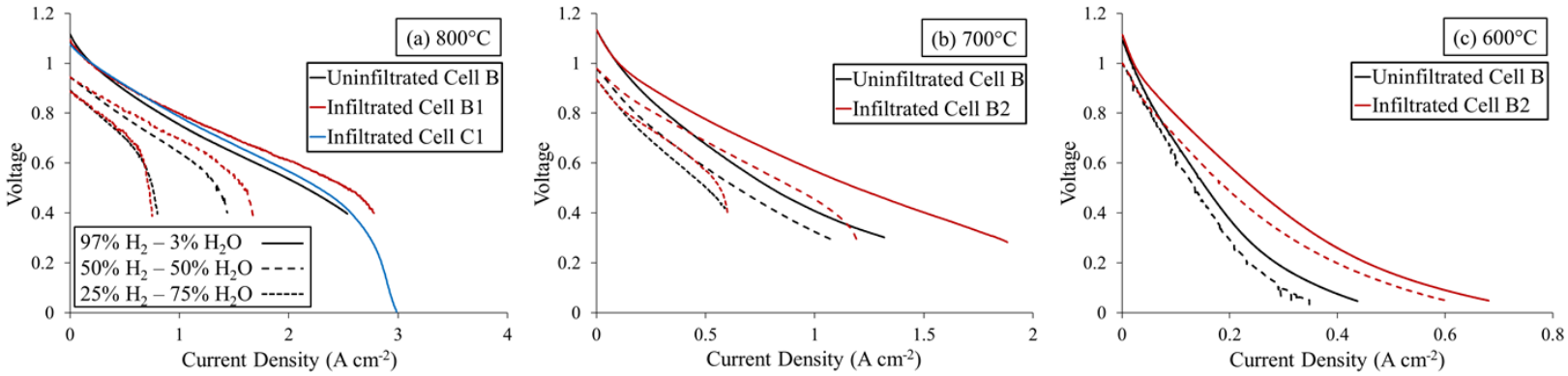

Figure 16: Electrochemical performance of Group B and C cells with 21% O2 on the cathode while varying the anode gas mix humidity at (a) 800°C, (b) 700°C, and (c) 600°C.

The trend of performance improvement decreasing with increasing anode gas humidity requires a different explanation. A simple reason is that the cells do not reach as high current densities in high p_{H_2O} atmospheres compared to those tested in low p_{H_2O} atmospheres, resulting in less polarization difference between the infiltrated and uninfiltrated cells. Qualitatively, it also appears that overall anode polarization is less at higher water vapor pressures, corroborating more detailed examinations of anode reaction kinetics [37,41,45,107]. Because the anode polarizations are lower at higher p_{H_2O}, improving the anodic charge transfer kinetics will have less effect than at conditions with lower p_{H_2O}.

Testing Temperature	**Cell**	**Maximum Power Density (W·cm^{-2}) at Different Anode Gas Mixtures**		
		3% H_2O – 97% H_2	**50% H_2O – 50% H_2**	**75% H_2O – 25% H_2**
800°C	Uninfiltrated Cell B	1.078	0.701	0.408
	Infiltrated Cell B1	1.281	0.831	0.414
	Change	+18.8%	+18.5%	+1.5%
700°C	Uninfiltrated Cell B	0.408	0.335	0.255
	Infiltrated Cell B2	0.606	0.455	0.289
	Change	+48.5%	+35.8%	+13.3%
600°C	Uninfiltrated Cell B	0.078	0.068	n/a
	Infiltrated Cell B2	0.123	0.099	n/a
	Change	+57.7%	+45.6%	n/a

Table 2: Maximum power densities of uninfiltrated and infiltrated cells from Group B after nickel spreading at various temperatures and anode gas compositions.

Even though cells from Group A and Group B were processed in the same manner, infiltration had a dramatic effect on the electrochemical performance for Group B but not for Group A. This suggests that the added TPBs due to the infiltrated nanoparticles had been activated during the nickel spreading procedure for Group B cells only, specifically during the high current density exposure with pure O_2 on the cathode side, resulting in a substantial improvement in cell performance. The only difference between these two groups was the testing condition; cells from Group B were exposed to higher current densities and thus higher humidity than cells from Group A.

The electrochemical performance of Infiltrated Cell C1 can be compared with that of Uninfiltrated Cell B, which was tested at the same temperature and has the same cathode (see Figure 16a). Whereas cells from group B showed significant performance improvement at 800°C, Infiltrated Cell C1 shows less improvement versus the uninfiltrated cell. This is evidence that exposure to extreme humidity can negate improvement due to the infiltrated nanoparticles, causing the cell performance to return back to that of an uninfiltrated cell.

3.4 Microstructure of infiltrated cells after electrochemical testing

The microstructures of all infiltrated cells after electrochemical testing are shown in Figure 17, alongside the microstructure of an untested infiltrated cell. When qualitatively compared with each other, it is clear that exposure to increasing humidity during testing results in the coarsening of nickel nanoparticles, when observed at room temperature. The quantitative microstructural data reported in Table 3 corroborates this observation. Infiltrated Cells B1 and C1, which were both exposed to nickel spreading

conditions at 800°C, show larger particle size and lower particle density than other cells; this is evidence of nickel spreading at these conditions. For the case of Infiltrated Cell C1, which was exposed to extreme humidity at the anode-electrolyte interface, nanoparticle density has been dramatically reduced.

Other cells, which were maintained at lower temperatures and lower humidity, do not show strong statistical evidence of coarsening. The microstructures of the untested cell, Infiltrated Cell A1, and Infiltrated Cell A2, as seen in Figure 17a–c, are very similar. This is supported by the quantitative nanoparticle characterization results reported in Table 3. This demonstrates that the cells not exposed to spreading conditions at 800°C have comparable microstructures.

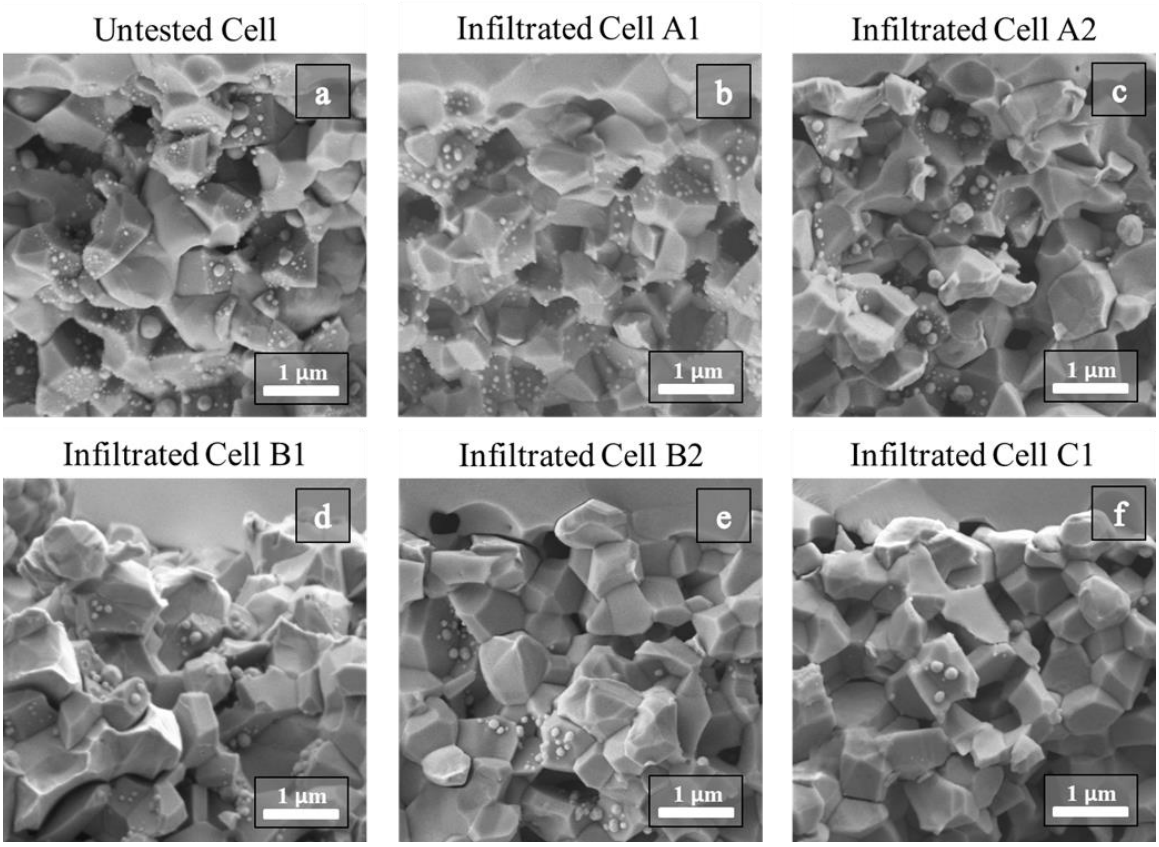

Figure 17: Fracture cross-section SEM image of the anode active layer of (a) an infiltrated but untested cell (same cell as Figure 13), and images after electrochemical testing from (b) Infiltrated Cell A1, (c) Infiltrated Cell A2, (d) Infiltrated Cell B1, (e) Infiltrated Cell B2, and (f) Infiltrated Cell C1.

Cell	Infiltration Weight Gain (wt. %)	Median Particle Size (nm)	Average Particle Size (nm)	Particle Density ($\#\cdot\mu m^{-2}$)
Untested	3.2%	45.5	54.3	26.1
A1	3.1%	58.7	60.4	14.6
A2	2.8%	53.9	81.9	17.2
B1	3.6%	75.0	93.5	8.1
B2	3.7%	52.5	67.0	15.1
C1	3.0%	85.4	89.3	1.4

Table 3: Measured statistics of infiltrated nickel nanoparticles.

Additional investigation of cells exposed to extreme humidities was done after more closely examining the microstructure of Infiltrated Cell C1. A high magnification SEM image of the AAL from the fracture cross-section of Infiltrated Cell C1 is shown in Figure 18. In this image, an interesting nanostructure can be seen on the surface of a YSZ grain. Further investigation using TEM on cells exposed to extreme humidity revealed that this nanostructure is composed of YSZ. It is postulated that this YSZ nanostructure is caused by the space-charge effect at YSZ/YSZ interfaces, as theoretically proposed by Zhang and Virkar [112]. The space charge effect causes the formation of nano-voids due to Yttria segregation at the YSZ/YSZ interfaces, reducing the ionic conductivity of the Ni-YSZ cermet. While scientifically interesting, this investigation determined that exposure to extreme humidity rapidly degrades the anode, and should be avoided.

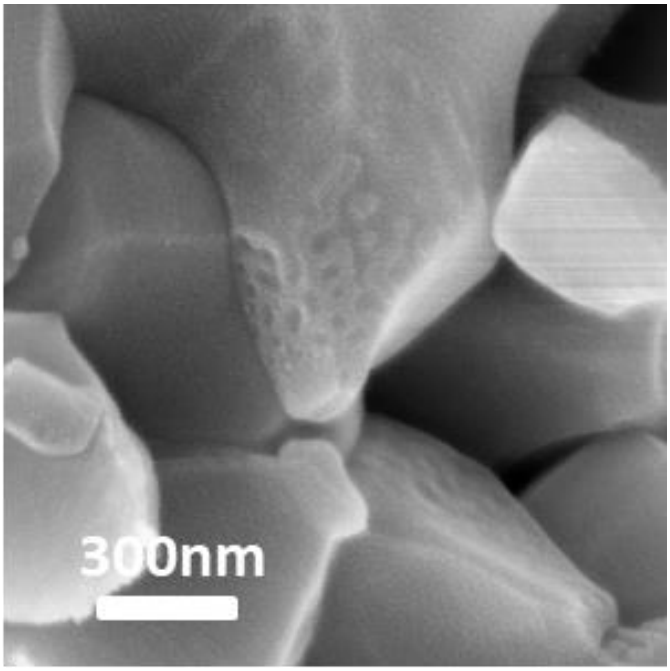

Figure 18: High magnification SEM image of the AAL from the fracture cross-section of Infiltrated Cell C1 after exposure to extreme humidity at 800 °C.

3.5 Discussion of nickel spreading mechanism

The proposed spreading mechanism of infiltrated nickel nanoparticles at high temperature during electrochemical testing is shown schematically in Figure 19. As deposited, nickel nanoparticles are isolated on YSZ, and thus do not contribute active TPBs. At the testing temperature and low current density (cell group A) nanoparticles do not spread significantly due to lack of exposure to high humidity. After cooling, these nanoparticles do not change appreciably. At high current densities (cell group B), infiltrated nanoparticles are exposed to humidity higher than 95% and begin to spread. This causes some nanoparticles to connect to each other and to nickel grains, activating their TPBs and improving cell performance. Upon cooling, percolating nanoparticles contract to higher contact angles, reducing surface coverage of the YSZ, thereby decreasing the number and increasing the diameter of particles, leading to particle coarsening. At extreme current densities and humidity (Infiltrated Cell C1), nickel nanoparticles wet the YSZ almost completely, with the contact angle between nickel and YSZ approaching 20°. When the surface coverage of the YSZ grains by the deposited Ni nanoparticles is very high, the active TPB density actually decreases [22]. Upon cooling, there is significant coarsening, as well as a decrease in the total volume of the Ni nanoparticles. The loss of volume can have two mechanisms: the formation of nickel hydroxide vapor phase species at extreme local humidity conditions, and the transport of nickel atoms to the larger nickel grains of the Ni-YSZ cermet.

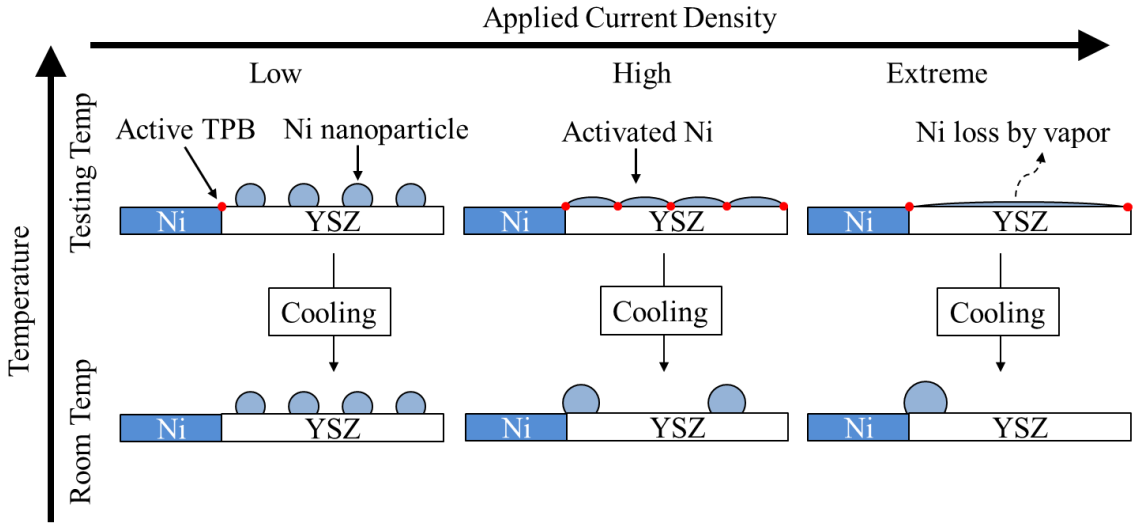

Figure 19: Schematic diagram of the infiltrated nickel nanoparticle evolution during electrochemical testing and after cooling due to nickel spreading and coarsening.

The obvious issue with connecting nickel nanoparticles via in-situ spreading is that the nickel nanoparticles are inherently degraded. After spreading and connecting with one another, nickel nanoparticles will always coarsen, resulting in a decrease in the TPB density of the electrode. Eventually, all nickel nanoparticles will simply coarsen with the nickel grains of the Ni-YSZ cermet, and then no performance improvement is expected compared to an uninfiltrated cell.

4. ACTIVATION OF INFILTRATED NICKEL NANOPARTICLES BY SIMULTANEOUS INFILTRATION WITH GADOLINIUM-DOPED-CERIA

The activation of infiltrated nickel nanoparticles in Ni-YSZ cermet electrodes by simultaneous infiltration with GDC has also been investigated. The effect of GDC infiltration on SOFC anodes both with and without nickel nanoparticles was studied by comparing the performance and microstructures of cells infiltrated with only nickel, only GDC, and nickel-GDC. The resistances of individual cell processes from these cells were quantified using EIS fitting, enabling direct comparison between cells of the impact that infiltration has on anodic charge transfer resistance and anodic mass transfer resistance. The stability of infiltrated nanoparticles was tested by exposing one cell of each kind to a humid atmosphere without current, and by exposing another cell of each kind to anodic mass transfer limited current and then measuring the performance of these cells at constant current for 120 hours.

4.1 Materials and methods

4.1.1 Cell preparation

In this study, anode-supported SOFC button cells were purchased from SOFCMAN Energy (Ningbo, China). Cells are composed of a 400 μm thick, 3 cm diameter NiO-YSZ anode bulk layer, a 5 μm thick NiO-YSZ AAL, an 8 μm thick dense YSZ electrolyte, a 15 μm thick and 1.6 cm diameter LSM-YSZ composite cathode active layer, and a 30 μm thick LSM cathode current collector layer. As mentioned before, in order to have enough porosity for effective anode infiltration, the NiO-YSZ anode needs to be reduced to Ni-YSZ. This was done in the same manner as described previously in

Section 3.1.1.

The infiltration solutions of Ni, GDC, and Ni-GDC were prepared separately by dissolving stoichiometric amounts of $Ni(NO_3)_2 \cdot 6H_2O$ (Chemsavers), $Gd(NO_3)_3 \cdot 6H_2O$ (Alfa Aesar), and $Ce(NO_3)_3 \cdot 6H_2O$ (Alfa Aesar) in ethanol at 70°C with stirring. The composition and molarity of these precursors in each solution is shown in Table 4. The successful formation of nickel, GDC, and Ni-GDC from the infiltration solution was verified by x-ray diffraction of powders produced by exposure of the liquid infiltration solution to the anode operating environment (800°C while flowing 2% H_2 – 98% Ar at 300 $cm^3 \cdot min^{-1}$ for 8 hours). Infiltration was conducted using the same procedure as described in Section 3.1.1. Each infiltration solution was used to infiltrate three cells for environmental stability tests, performance measurements, and electrochemical stability tests; these processes will be detailed in the following sections. To ensure that the infiltration procedure is consistent, the weight gain of cells was measured after infiltration. The weight gain of each infiltrated cell is shown in Table 4. The reported value is the average plus/minus the standard deviation. The weight gain between cells with the same infiltration solution has low deviation, demonstrating good repeatability.

Cells:	Ni infiltrated	GDC infiltrated	Ni-GDC infiltrated
Precursor molarity:	1M Ni	2M GDC	2M Ni, 2M GDC
Rounds of infiltration:	5	1	1
Weight gain:	1.60 ± 0.02%	1.26 ± 0.05%	1.29 ± 0.04%

Table 4: Details of infiltration procedure and resulting weight gain for nickel, GDC, and Ni-GDC infiltrated cells.

4.1.2 Microstructural characterization

To characterize the microstructure of the infiltrated cells before testing, one cell of each kind (uninfiltrated, nickel infiltrated, GDC infiltrated, and Ni-GDC infiltrated) was heated to 800°C while flowing 2% H_2 – 98% Ar gas at 300 $cm^3 \cdot min^{-1}$ and held for 8 hours before returning to room temperature under gas flow. This process reduces infiltrated NiO to Ni and forms GDC from the precursor oxides. Each cell was then fractured into three pieces to observe the microstructure after exposure to different conditions: one piece was imaged as is, the second piece was heated to 800°C while flowing 2% H_2 – 98% Ar gas at 300 $cm^3 \cdot min^{-1}$ and held for 48 hours, and the third piece was heated to 800°C while flowing 25% H_2 – 75% H_2O at 300 $cm^3 \cdot min^{-1}$ and held for 48 hours. Hydrogen gas was humidified using a water filled gas washing bottle submerged in a heated water bath, as described previously in Section 3.1.3. In this way, the effects of time and gas humidity on the stability of the infiltrants at 800°C can be observed. SEM was then used to image the fracture cross-sections from each cell piece from the uninfiltrated, nickel infiltrated, GDC infiltrated, and Ni-GDC infiltrated cells. SEM images were recorded using a field emission Zeiss SUPRA 55-VP scanning electron microscope (Carl Zeiss AG, Germany).

To observe the detailed interaction between nickel and GDC infiltrants in the Ni-GDC infiltrated cell, high magnification images and elemental dot maps were collected by transmission electron microscopy (TEM) using an FEI ThermoFisher Scientific Inc., USA Tecnao Osiris equipped with an energy dispersive x-ray (EDX) detector and operated at 200 keV in scanning transmission electron microscopy (STEM) mode.

Electron transparent TEM samples were prepared by a conventional lift-out technique using a Gallium focused ion beam (FIB) in an FEI Quanta 3D FEG Dual Beam SEM/FIB.

The porosity of the Ni-YSZ cermet electrodes after infiltration and electrochemical testing was also investigated. The porosity was measured using polished cross-section images recorded by SEM. Polished cell cross-sections were prepared by infiltrating epoxy into fractured cells, curing the epoxy at room temperature, and polishing the epoxied samples. In order to get a good measure of the porosity across the entire electrode, images were recorded every 50 microns throughout the entire thickness of the electrode. At each depth, three images were recorded to ensure results were representative of the entire electrode. Avizo 3D (ThermoFisher Scientific Inc., USA) was used to segment out the pore phase and obtain the area fraction to calculate the porosity in each image. The porosity of all three images at each anode depth were then averaged to get the reported values. A useful way to interpret the effect of infiltration on the porosity of the cell is to plot the pore occupation ratio, which is a measurement of the fraction of available pore volume that is occupied by any infiltrants. The pore occupation ratio was calculated by Equation 13:

$$Pore\ Occupation\ Ratio = \frac{Porosity\ of\ Uninfiltrated\ Cell - Porosity\ of\ Infiltrated\ Cell}{Porosity\ of\ Uninfiltrated\ Cell} = \frac{Volume\ of\ Infiltrant}{Porosity\ of\ Uninfiltrated\ Cell} \quad (13)$$

This characterization work was conducted by Yanchen Lu.

4.1.3 Electrochemical testing preparation and apparatus

In preparation for electrochemical testing, a silver mesh (Alfa Aesar, USA) was then adhered to the cathode surface using silver ink (Alfa Aesar, USA) and dried in air at

80°C. Nickel ink (Fuel Cell Materials, USA) was then painted onto the anode surface and the cell was placed on top of the nickel mesh current collector (Alfa Aesar, USA) before assembling the full electrochemical testing stand, which was shown previously in Figure 14. As before, the anode and cathode electrodes were gas sealed using glass paste around the edge of the cell. Mica gaskets were also placed on the top and bottom surfaces of the cell before placing the cell and gaskets between the fuel side Al_2O_3 tube and the machined Al_2O_3 plate. The cathode side tube and end cap were then placed on top of the machined Al_2O_3 plate, using the Al_2O_3 rods to ensure alignment between the air and fuel side tubes. The entire assembly was then spring-loaded between two aluminum end plates using Al_2O_3 rods for rigidity and to compress the mica gaskets. Nickel lead wires (Alfa Aesar, USA) on the anode side and silver lead wires (Alfa Aesar, USA) on the cathode side were protected by feeding them through small Al_2O_3 tubes. Al_2O_3 tubes were also used for inlet and outlet gas tubes on both anode and cathode sides. Cell temperature was monitored during electrochemical testing using a K-type thermocouple placed in the cathode side chamber approximately 1 cm away from cell.

After assembly, the electrochemical testing stand was placed in a furnace and heated to 800°C, as measured by the cathode side thermocouple, at $1°C \cdot min^{-1}$. During heating, 1 $L \cdot min^{-1}$ of dry air was flowed on the cathode side and 300 $cm^3 \cdot min^{-1}$ of the 5% H_2 – 98% Ar gas mixture was flowed on the anode side. Once at the set temperature, the cell was held under open circuit condition for 12 hours to allow time for the glass paste to cure, and then the anode gas mixture was changed to 97% H_2 – 3% H_2O. The quality of the gas sealing was then evaluated by monitoring the cell's open circuit potential for the

following 12 hours. The performance of each cell was then stabilized by applying 0.5 $A \cdot cm^{-2}$ of current for 48 hours.

4.1.4 Electrochemical testing procedure

Two cells of each type were measured for their performance and electrochemical stability. Cell performance was measured at temperatures of 800°C, 750°C, and 700°C. I-V scans and EIS were used to evaluate cell performance. I-V scans were recorded from OCV to 700 mV at a rate of 5 $mA \cdot s^{-1}$. EIS scans were recorded at open circuit conditions using an AC amplitude of 30 mV between 200000 Hz and 0.02 Hz with 12 data points recorded per decade. For one uninfiltrated cell, a large set of measurements were recorded while varying the anode side gas mixture, the cathode side gas mixture, and the cell temperature. The full set of operating conditions for I-V and EIS measurements are shown below in Table 5. All measurements were recorded with a flowrate of 300 $cm^3 \cdot min^{-1}$ over the anode and 1 $L \cdot min^{-1}$ over the cathode.

Temperatures	**$pO_2 - pN_2$**	**$pH_2 - pH_2O$**
800°C	100% O_2	97% H_2 – 3% H_2O
	10% O_2 - 90% N_2	
	21% O_2 - 79% N_2	
750°C	21% O_2 - 79% N_2	97% H_2 – 3% H_2O
		90% H_2 – 10% H_2O
700°C		82% H_2 – 18% H_2O
		75% H_2 – 25% H_2O
650°C		50% H_2 – 50% H_2O
		25% H_2 – 75% H_2O

Table 5: Operating conditions for I-V and EIS measurements used for the full cell performance characterization of an uninfiltrated cell.

After performance measurement, each cell was exposed to anodic mass transfer limited current. By drawing anodic mass transfer limited current, the anode active layer is exposed to high humidity, causing the spreading of nickel nanoparticles and accelerating the degradation of infiltrated nickel nanoparticles, as shown by the work presented in Section 3. Anodic mass transfer limited current was applied both by I-V scans and galvanostatic measurements, which were conducted while flowing 97% H_2 – 3% H_2O over the anode and 100% O_2 over the cathode at 800 °C. First, an I-V scan was conducted down to 400 mV, reaching the anodic mass transfer limited current density. Next, 8 minutes of galvanostatic current was applied at the anodic mass transfer limited current density. Then, a second I-V scan down to 400 mV was recorded. Afterwards, another 16 minutes of galvanostatic current was applied at the anodic mass transfer limited current density. Finally, a third I-V scan down to 400 mV was recorded to monitor any changes in the anodic mass transfer limited current density that may have occurred during the prior measurements.

The stability of infiltrated nickel, GDC, and Ni-GDC nanoparticles were further tested by a 120-hour galvanostatic measurement at 1 $A \cdot cm^{-2}$ current density. The electrochemical performance during this measurement and microstructures after testing are compared to evaluate the stability of the infiltrated materials.

4.2 Microstructure of infiltrated cells

The microstructures of the uninfiltrated and infiltrated cells after being reduced at 800°C and exposed to 2% H_2 – 98% Ar for 8 hours are shown in Figure 20a-d. This exposure reduces the infiltrated NiO to nickel, and forms GDC from the precursor oxides.

When analyzing the infiltrated microstructures, three factors should be considered: particle size, surface coverage, and connectivity. The particle size of infiltrated nickel in Figure 20b is about 30–50 nm. Infiltrated nickel nanoparticles homogenously cover the surfaces of YSZ particles, and are clearly not connected with one another. Infiltrated nickel nanoparticles are likely not stable on the surface of nickel grains, because there is no surface energy difference between nickel nanoparticles and the nickel grains, so they will simply coarsen. The particle sizes of infiltrated GDC and infiltrated Ni-GDC are shown in Figure 20c and Figure 20d, respectively. They are similar, though quantification is not simple because of the high degree of connectivity between particles. This connectivity is clearly due to the GDC, and is hopefully beneficial for the stability of the infiltrated microstructure as well as the electrochemical performance. Infiltrated GDC and Ni-GDC also show more uniform coverage than infiltrated nickel, and seem to deposit across the intersections between nickel and YSZ grains. This is unlike infiltrated nickel, which are only visible on YSZ grains. From these microstructures, it appears that GDC is a good candidate for connecting nickel nanoparticles. This should activate the TPB of infiltrate nickel nanoparticles, as the GDC facilitates the ambipolar diffusion of both oxygen ions and electrons between nickel nanoparticles and the Ni-YSZ cermet substrate.

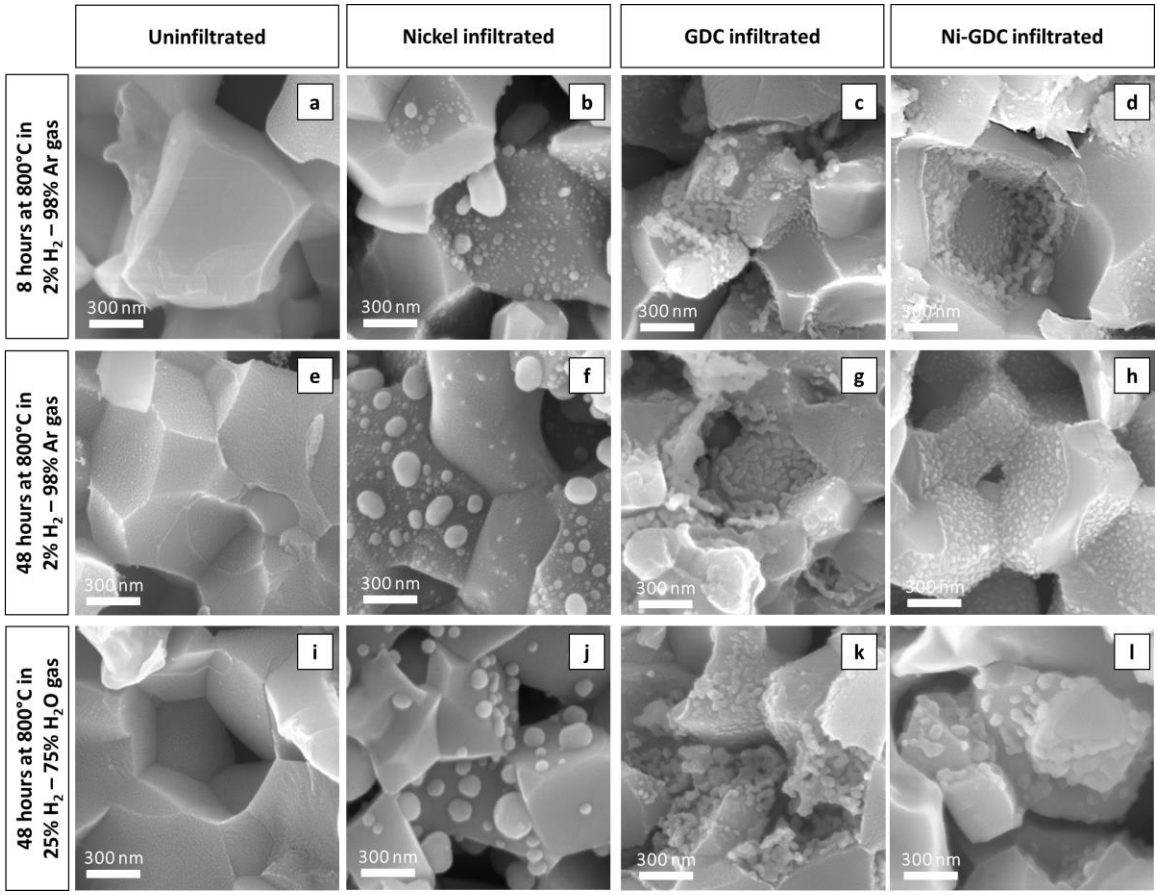

Figure 20: Microstructures of uninfiltrated, nickel infiltrated, GDC infiltrated, and Ni-GDC infiltrated Ni-YSZ anodes (a-d) after exposure at 800°C to 2% H_2 – 98% Ar for 8 hours, (e-h) 2% H_2 – 98% Ar for 48 hours, and (i-l) 25% H_2 – 75% H_2O for 48 hours.

The environmental stability of the uninfiltrated and infiltrated microstructures was studied by exposing cells at 800°C to 2% H_2 – 98% Ar and 25% H_2 – 75% H_2O for 48 hours. The resulting microstructures are shown in Figure 20e-h and Figure 20i-l, respectively. By comparing the microstructures of infiltrated cells exposed to these conditions, the effects of time at operating temperature and exposure to humidity on the infiltrated structures can be observed. Quick study of the uninfiltrated cell shows that there is no significant degradation of the Ni-YSZ cermet even after exposure to 75%

humid hydrogen for 48 hours. This is expected, because the Ni-YSZ cermet has been sintered at temperatures greater than 1350°C, and are thus very stable in these environments. In comparison, infiltrated nickel shows clear degradation. After 48 hours in dry hydrogen (2% H_2 – 98% Ar) at 800°C, the particle size of infiltrated nickel has obviously increased; some nanoparticles with diameter less than 30 nm are still visible, but their density has been decreased. After 48 hours in humidified hydrogen (25% H_2 – 75% H_2O) at 800°C, no particles with diameter less than 100 nm remain. The presence of humidity clearly exacerbates the coarsening behavior that is obvious even in dry hydrogen. As the infiltrated nickel nanoparticles coarsen, the coverage of nickel nanoparticles on the YSZ surface decreases and the distance between infiltrated nickel nanoparticles increases. This makes it less likely that infiltrated nickel TPBs will be able to actively participate in the electrochemical reaction.

Infiltrated GDC and infiltrated Ni-GDC demonstrate much better stability than infiltrated nickel. Even after exposure to humidified hydrogen, infiltrated GDC is not obviously degraded in any way. Infiltrated Ni-GDC shows no obvious degradation after exposure to dry hydrogen, but an increase in the particle size is clear after exposure to humidified hydrogen. The extent of this coarsening is not nearly as severe as is seen in the nickel infiltrated cell, as the infiltrated Ni-GDC structures maintain diameters less than 100 nm. Also, the infiltrated Ni-GDC maintains good connectivity even after this coarsening, so the TPBs of the infiltrated Ni-GDC can still be utilized for the electrochemical reaction of the electrode.

While infiltrated Ni-GDC shows promising improvements to the stability and

connectivity of the infiltrated material compared to the nickel infiltrated cell, it is not obvious from the SEM images how the infiltrated nickel and infiltrated GDC interact with one another. In order to distinguish between the two phases, STEM imaging and elemental dot mapping by EDX were conducted on an electron-transparent sample from the anode active layer of the Ni-GDC cell after infiltration and exposure to 2% H_2 – 98% Ar for 8 hours at 800°C. Results of this procedure are shown in Figure 21. From just the bright-field image (Figure 21a), it can be seen that nanoparticles with diameters less than 50 nm are deposited on all of the surfaces of the pore. The combined elemental dot map (Figure 21b) shows that both nickel and GDC nanoparticles are deposited by infiltration, and that they are obviously connected with one another on the surface of YSZ grains. GDC surrounds many nickel nanoparticles, physically constraining them and preventing infiltrated nickel from coarsening, explaining the improvement in nanoparticle stability observed previously. Contrast of the individual elemental dot maps of nickel (Figure 21c) and GDC (Figure 21d) makes it clear that nickel and GDC have different deposition behavior during infiltration: nickel nanoparticles are only visible on surface of YSZ grains, while GDC is deposited on both nickel and YSZ grains. This is positive, because it means that infiltrated GDC connects infiltrated nickel nanoparticles to one another as well as to the nickel of the Ni-YSZ cermet, enabling their TPBs to contribute to the electrochemical reaction.

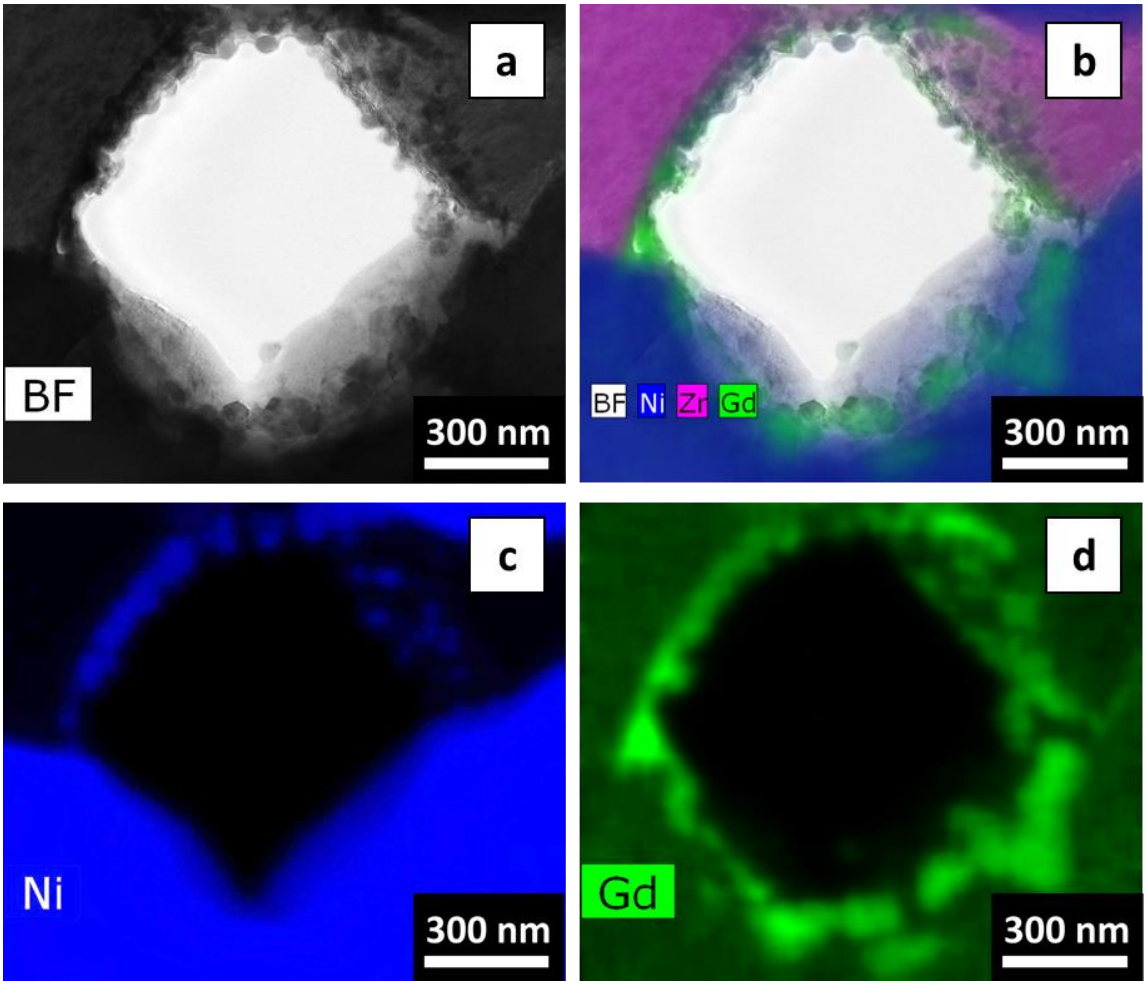

Figure 21: (a) STEM bright-field image of the anode active layer of the Ni-YSZ cermet anode after infiltration with nickel and GDC, (b) the elemental dot maps of Ni, Zr, and Gd, superimposed on the bright-field image, and the individual elemental dot maps of (c) Ni and (d) Gd.

The impact of infiltration on the porosity of the electrode was evaluated by measuring the porosity of uninfiltrated and infiltrated electrodes throughout the thickness of each electrode by analysis of SEM images of polished cell cross-sections after electrochemical testing. The resulting porosity profiles for the uninfiltrated, nickel infiltrated, GDC infiltrated, and Ni-GDC infiltrated cells are shown in Figure 22a. Each data point corresponds to the average porosity measured from three images, and the error

bars report the maximum and minimum measured porosity between the three images. The uninfiltrated cell has a uniform porosity of about 20% throughout the electrode thickness as well as within the anode active layer (AAL). Infiltration results in a decrease of the porosity throughout the electrode, but this decrease is not uniform. Infiltrant clearly fills pores near the surface of the anode more than pores in the middle of the electrode, which likely occurs due to the presence of some excess solution on the surface during the infiltration procedure. While the deposition of infiltrant is fairly similar between all of the infiltrated cells, infiltration of GDC causes a slightly greater decrease in porosity than either Ni or Ni-GDC, especially near the anode-electrolyte interface. This is especially clear in the profile of the pore occupation ratio, shown in Figure 22b. Infiltrated GDC occupies approximately 30% of the available pore volume in the anode active layer, compared to about 20% for the Ni and Ni-GDC infiltrated electrodes. This increase in the occupied pore volume will result in an equal decrease of the H_2-H_2O effective diffusivity, as shown by Equation 11. This corresponds to an equal decrease in the anodic mass transfer limited current density, calculated by Equation 9, and a corresponding increase in the anodic mass transfer polarization.

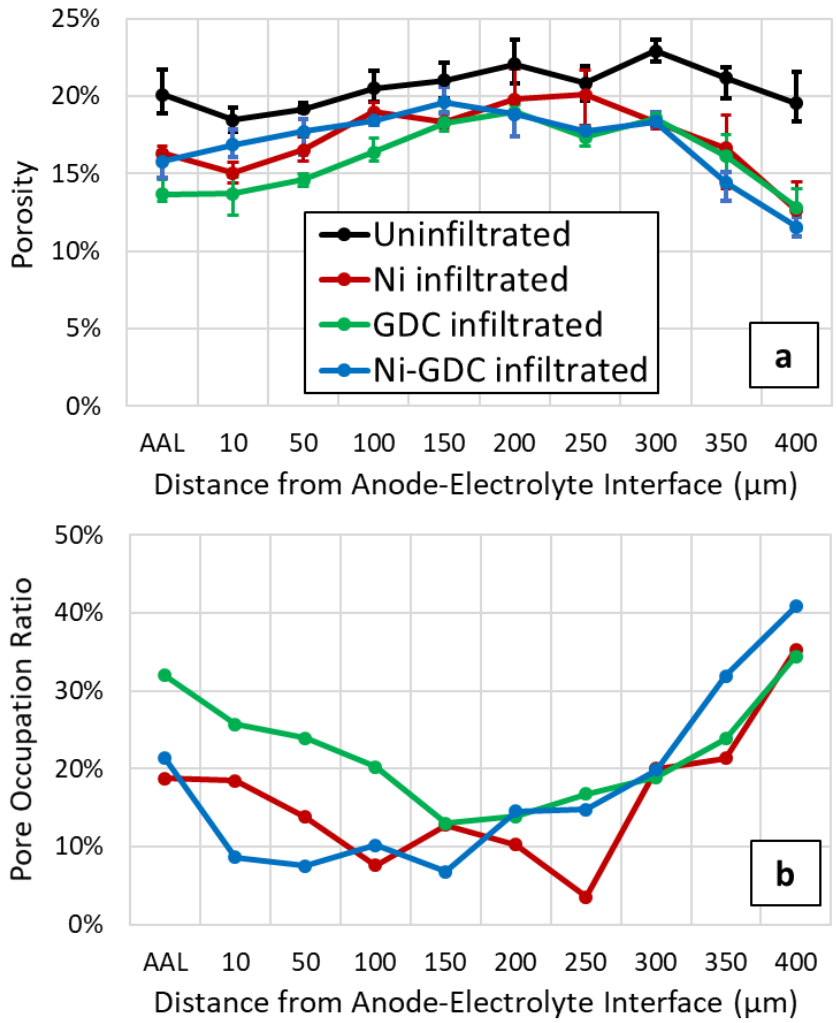

Figure 22: Variation of the (a) porosity and (b) pore occupation ratio throughout the entire thickness of uninfiltrated and infiltrated Ni-YSZ cermet electrodes.

4.3 Full performance characterization of an uninfiltrated cell by EIS fitting

The characterization of SOFCs by modeling of EIS data has been pursued for many years, but has only seen success as a reliable and consistent method for full cell performance characterization in the last decade. The biggest reason that EIS modeling was mistrusted in the past, and the biggest challenge to overcome when using it today, is the potential for misinterpretation of the impedance response. This is especially the case

for the characterization of full cells, which have many distinct cell processes with overlapping frequency ranges. Each cell process is modeled with its own equivalent circuit element, leading to a large number of degrees of freedom. This is a problem because there are enough free parameters to make nearly any EIS data look well fitted but there is no assurance that the result is actually representative of the physical processes occurring in the electrode. Physically relevant EIS modeling can be achieved through best practices: proper experimental apparatus design and EIS measurement procedure, recording measurements at a wide range of operating conditions, process identification and ECM selection utilizing DRT, and validation of the EIS modeling results by I-V simulation and comparison to literature. Experimental design and EIS measurement procedures were described previously in Section 4.1. The rest of this section describes the methods used in this work for practically achieving physically relevant full cell characterization of an uninfiltrated cell by EIS fitting.

Recording cell measurements under a wide variety of operating conditions is vital for acquiring physically relevant results by EIS fitting. For this work, cell measurements were recorded at all of the operating conditions identified in Table 5. Variation of the cell operating conditions has a dramatic effect on the I-V and impedance response of the cell, as can be seen in Figure 23 through Figure 25. Figure 23 shows the cell response at 800 °C with 21% O_2 – 79% N_2 flowing over the cathode while varying the anode fuel gas mixture. As the humidity of the anode fuel gas mix increases, the I-V measurement becomes less curved, and this is mirrored by the large reduction of the polarization resistance seen in the EIS measurement. Cell polarization resistance decreases until the

humidity of the anode gas mixture reaches 50%, before increasing again. From observation of the Bode plot in Figure 23, this decrease in polarization resistance is due to changes across the entire frequency range of the EIS response.

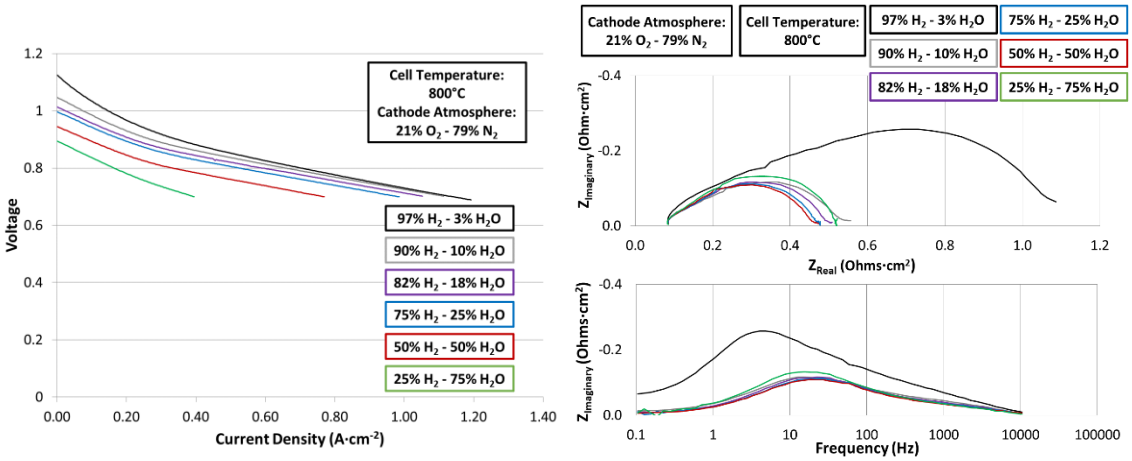

Figure 23: I-V and EIS measurements of an uninfiltrated cell while varying the anode fuel gas mixture.

Figure 24 shows the cell response at 800 °C with 97% H_2 – 3% H_2O flowing over the anode while varying the cathode gas mixture. As the oxygen concentration over the cathode is increased, the polarization resistance of the cell continuously decreases. From observation of the Bode plot, the change in the impedance response is centered around about 10 Hz, with no effect at all on the impedance response at frequencies greater than 1000 Hz. This suggests that there are no cathode processes that impact cell impedance at frequencies greater than 1000 Hz.

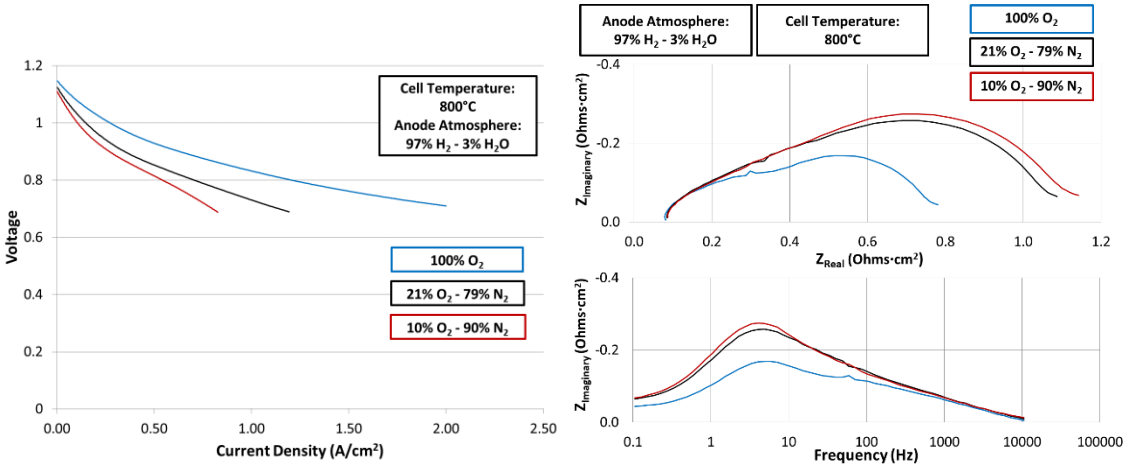

Figure 24: I-V and EIS measurements of an uninfiltrated cell while varying the cathode gas mixture.

Figure 25 shows the cell response while flowing 97% H_2 – 3% H_2O over the anode and 21% O_2 – 79% N_2 over the cathode and varying the operation temperature of the cell. Compared to the two previous figures, it is clear that operation temperature has the most dramatic effect on cell performance. As cell temperature is decreased, the I-V performance of the cell is continuously decreasing, and the total resistance of the cell is continuously increasing. From observation of the Bode plot, the change of cell temperature impacts the cell response at all frequencies.

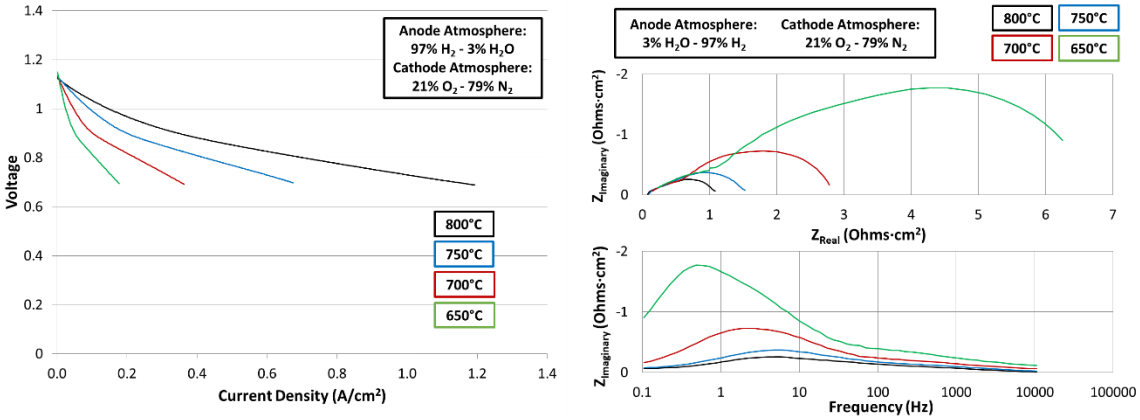

Figure 25: I-V and EIS measurements of an uninfiltrated cell while varying cell temperature.

After measurements were recorded, EIS data was prepared for fitting by removing the contribution of inductance from the data and checking the quality of the data using Lin-KK, removing any data points with high error [70,76–78]. High error corresponds to any error greater than 1%. When checking the quality of EIS measurements using Lin-KK, special attention should be paid to check for common systematic errors: drift of the impedance response when recording low frequency data points, noisy data around 50-60 Hz caused by AC power supplies, and high frequency noise due to inductive effects and equipment noise [47]. Systematic errors can be addressed by design of the experimental apparatus, equipment selection, and using proper measurement procedures [47]. Induction removal was done by using a linear fit of the measured EIS data to measure the inductance, then subtraction of the inductance from the measured data. The formula for the impedance response of an inductor, $Z_{inductor}$, is shown below:

$$Z_{Inductor} = i\omega L \tag{14}$$

where ω is the frequency and L is the inductance. From observation of this formula, it should be simple to measure the inductance of any given EIS data just by measuring the slope of the imaginary impedance of any measured EIS data versus frequency at frequencies where the inductance dominates the impedance response of the cell. The measurement of the inductance is show below:

$$L = \frac{\Delta Z''_{measured}}{\Delta\omega}\Bigg|^{\omega > 10^4\ Hz} \tag{15}$$

where $Z''_{measured}$ is the imaginary component of the measured EIS data. The slope is measured at frequencies greater than 10^4 Hz because the typical inductance of the

electrochemical testing apparatus used in this work is about $1x10^{-6}$ H, so the inductive response of the testing apparatus only becomes apparent at frequencies greater than 10^4. Once the inductance has been determined, the impedance response of the inductor can be calculated, and simply subtracted from the measured EIS to get the processed EIS data, Z_{data}:

$$Z_{data} = Z_{measured} - Z_{Inductor} \tag{16}$$

This procedure was found to produce identical results as experimentally measuring the inductance of the lead wires using the method described by Boigues Muñoz et al. and can be implemented without requiring any physical experiment [42]. The results of both of these techniques for inductance correction can be seen compared to the raw EIS data in Figure 26. The corrected and uncorrected data begin to diverge at approximately 10^2 Hz; at lower frequencies, the inductive response is too small to be measured. From comparing the corrected and uncorrected data, it can be seen that at high frequencies (between 10^3 Hz and 10^4 Hz), the inductive and capacitive components of the cell impedance response overlap significantly. Removing the inductance leaves only the capacitive response, enabling better analysis of the cell performance.

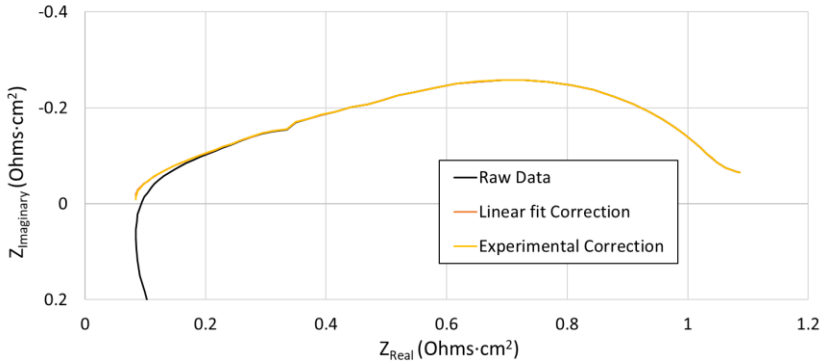

Figure 26: EIS before and after inductance correction, both by linear fit as well as subtraction of the experimentally measured lead wire inductance.

In order to identify the relative contributions of individual cell processes to the overall EIS measurement, the DRT transform was used to observe the frequency domains and relative resistances of each process. DRT was conducted in MATLAB using the freely available software "DRTTOOLS", which utilizes the Tikhonov regularization to conduct the transform [71]. A regularization parameter of 10^{-3} was used for all transforms [74]. The DRT spectra when varying the anode fuel gas mixture, the cathode gas mixture, and the cell temperature can be seen in Figure 27, Figure 28, and Figure 29, respectively. Unlike in the Nyquist and Bode plots shown previously, five distinct processes can be clearly observed. These processes have been identified in the plots, with arrows showing their functional dependencies. The direction of the arrows corresponds to decreasing H_2 partial pressure over the anode (balanced by increasing H_2O partial pressure) (Figure 27), decreasing oxygen concentration over the cathode (Figure 28), and decreasing cell operation temperature (Figure 29). These processes, listed in order of high frequency to low, are: $P_{1(a)}$ and $P_{2(a)}$, which are anodic charge transfer processes, $P_{3(c)}$, the cathodic charge transfer process, $P_{4(a)}$, the anodic mass transfer process, and $P_{5(c)}$, the cathodic mass transfer process. The frequency ranges, functional dependencies, representative equivalent circuit elements, and physical meanings of these processes are described in Table 6. When observing the DRT figures, note that $P_{3(c)}$ and $P_{4(a)}$ both have oscillations at frequencies higher than their peak maximum [67,74,75]. Also, the frequency max of $P_{4(a)}$ in the DRT is about an order of magnitude higher than it is in the Bode plot due to the nature of the DRT transform [75].

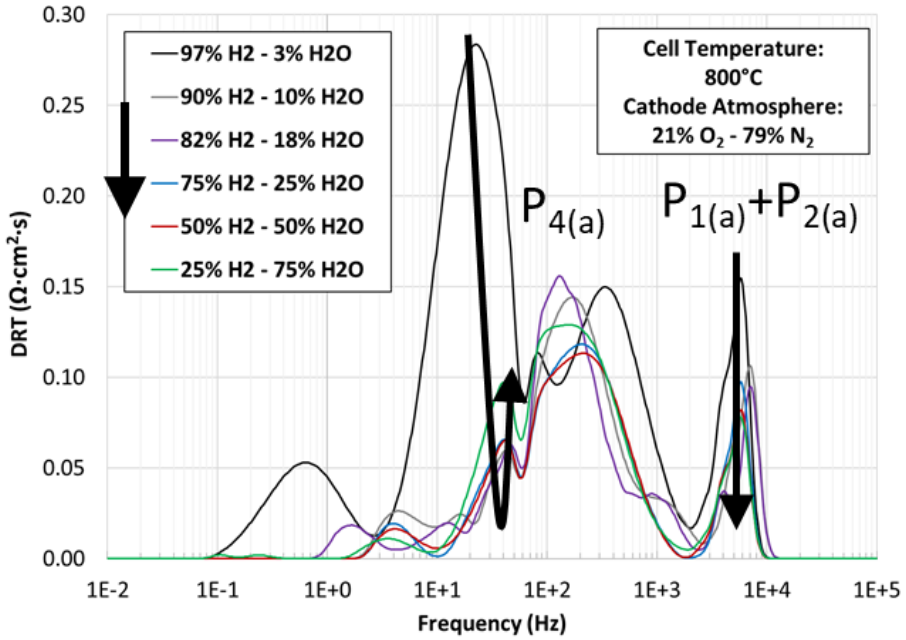

Figure 27: DRT of uninfiltrated cell EIS data while varying the anode fuel gas mixture. Arrows show process behavior with increasing water vapor concentration.

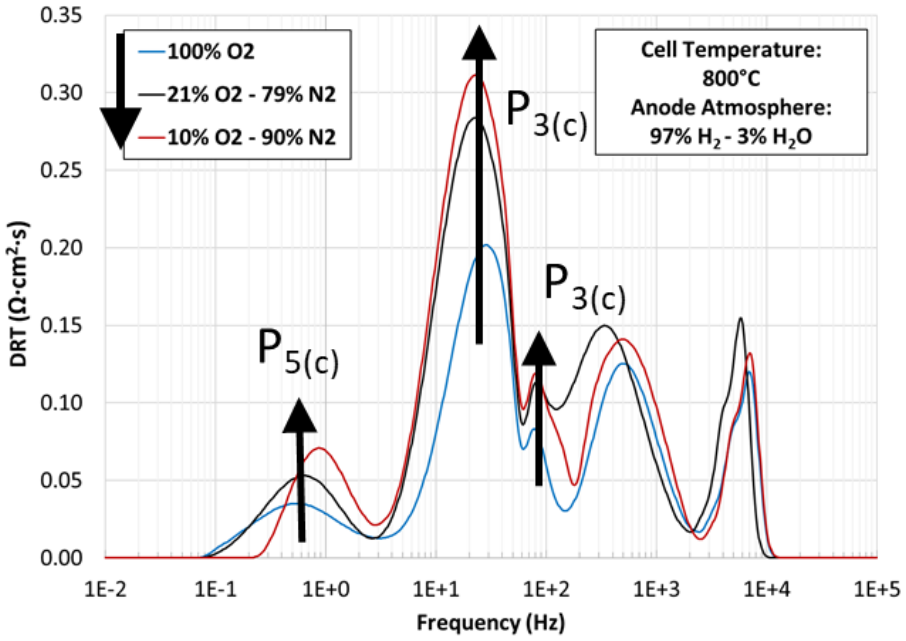

Figure 28: DRT of uninfiltrated cell EIS data while varying the cathode gas mixture. Arrows show process behavior with decreasing oxygen concentration.

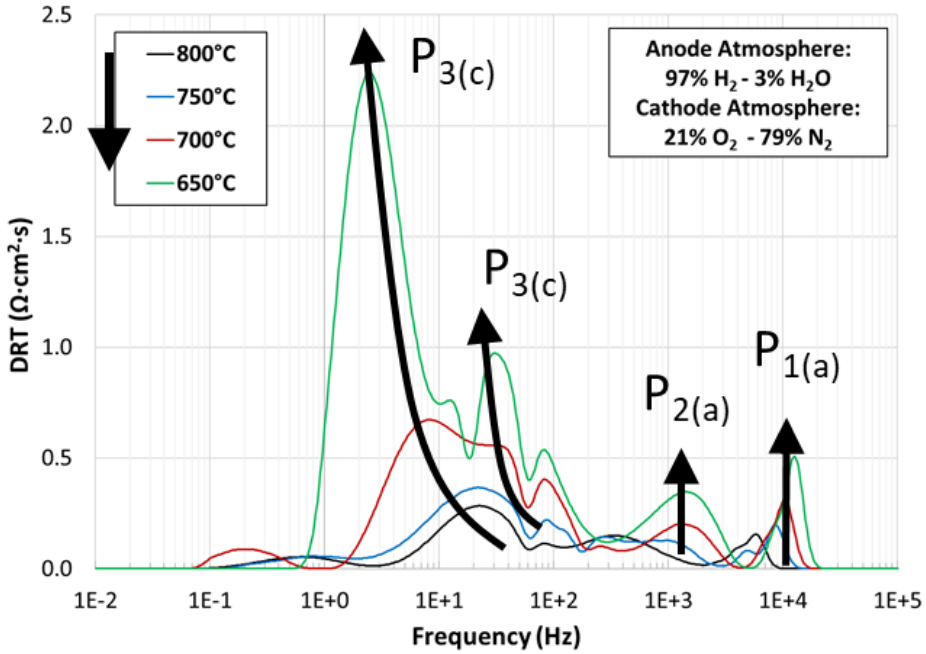

Figure 29: DRT of uninfiltrated cell EIS data while varying cell temperature. Arrows show process behavior with decreasing cell temperature.

Process	Frequency range	Dependencies	Equivalent circuit element	Physical meaning
$P_{1(a)}$ $P_{2(a)}$	3 to 20 kHz 400 to 3000 Hz	T (strong), pH_2-pH_2O	RQ+RQ or TLM	Ionic transport, charge transfer reactions, and gas conversion within the AAL [34,42–45,110]
$P_{3(c)}$	1 to 300 Hz	T (strong), pO_2	Ge or PET de Levie	Oxygen disassociation reactions at cathode TPBs and O^{2-} diffusion in the cathode [44,61,113,114]
$P_{4(a)}$	1 to 10 Hz	pH_2-pH_2O	FLW	Gas diffusion through the anode [42–44,110]
$P_{5(c)}$	0.1 to 5 Hz	pO_2	RQ	Gas diffusion through the cathode [44,61,113]

Table 6: Cell processes identified by DRT and their relevant frequency ranges, functional dependencies, equivalent circuit elements, and physical meanings.

These identified processes agree strongly with those identified previously by Leonide et al., which was conducted using these same techniques on cells with similar

architecture, so the ECM proposed by those researchers is used here to model the EIS response of the cell [44]. This ECM was previously shown in Figure 8. EIS data was fit with this ECM using a complex non-linear least squares minimization function written in MATLAB. This MATLAB function is provided in Appendix 4, with an example run script provided in Appendix 5.

When fitting EIS data at many operating conditions a batch fitting procedure was used. Batch fitting minimizes the error of the ECM fit on several sets of EIS data from different operating conditions, while respecting the physical limitations that govern the change of cell resistances when the operating conditions are varied. Respecting these physical limitations can be done with a few simple rules: 1) when the anodic fuel gas mixture is changed, cathode resistances are held constant, 2) when the cathodic gas mixture is changes, anode resistances are held constant, 3) when the operating temperature is changed, mass transfer resistances are not allowed to vary substantially. The third rule may not be intuitive, but it is widely reported that gas diffusion resistance is independent of temperature, and this has been observed experimentally in my own work as well. Practical application of these batch fitting rules is shown schematically in Figure 30, Figure 31, and Figure 32. Through this batch fitting process, each individual EIS fit respects the physical limitations that separate anodic and cathodic processes, as well as the different functional dependencies of charge transfer and mass transfer processes documented in Table 6. This method produces measurements that are physically relevant over a wide range of cell operating conditions.

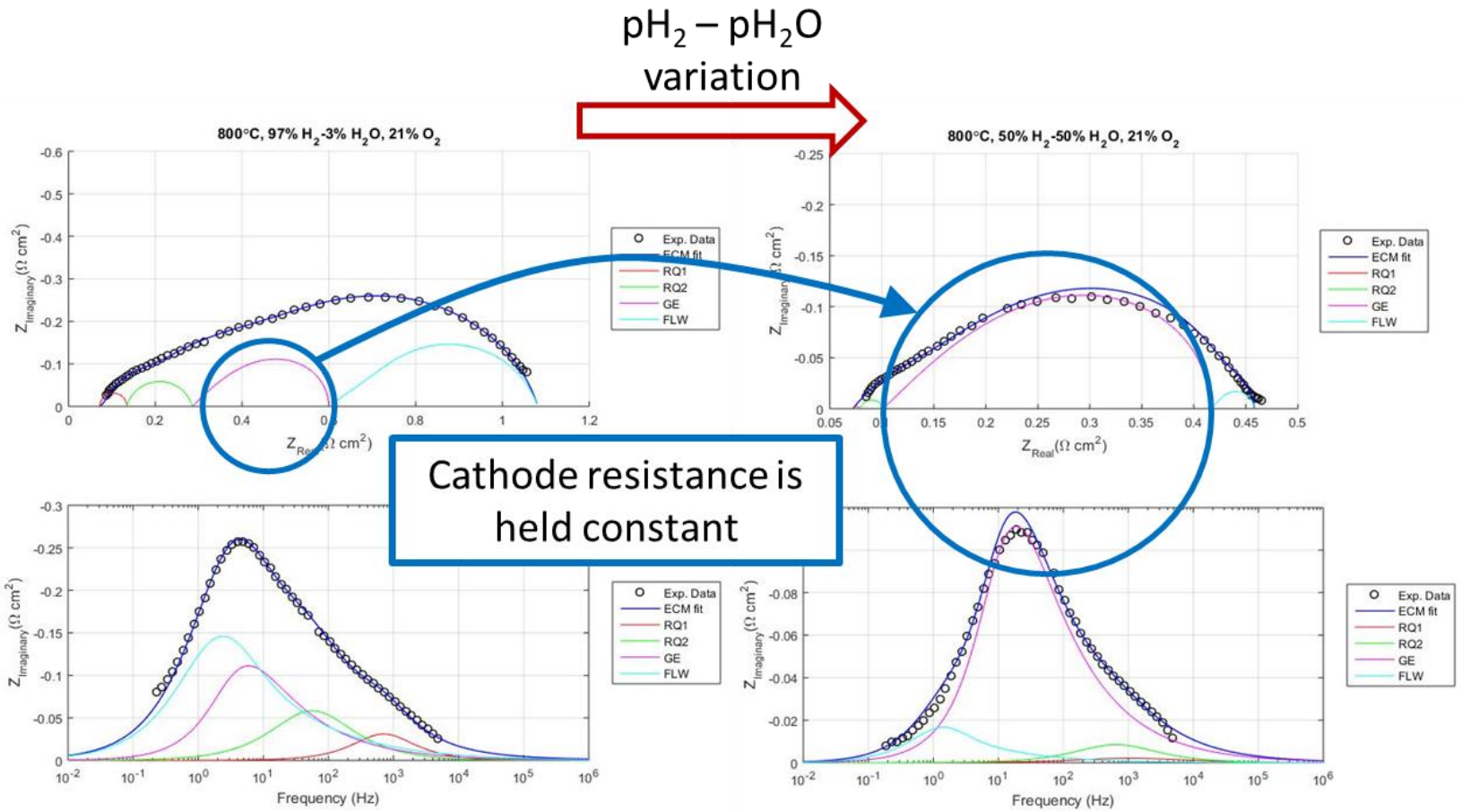

Figure 30: Variation of the anode fuel gas mixture during batch fitting of EIS data.

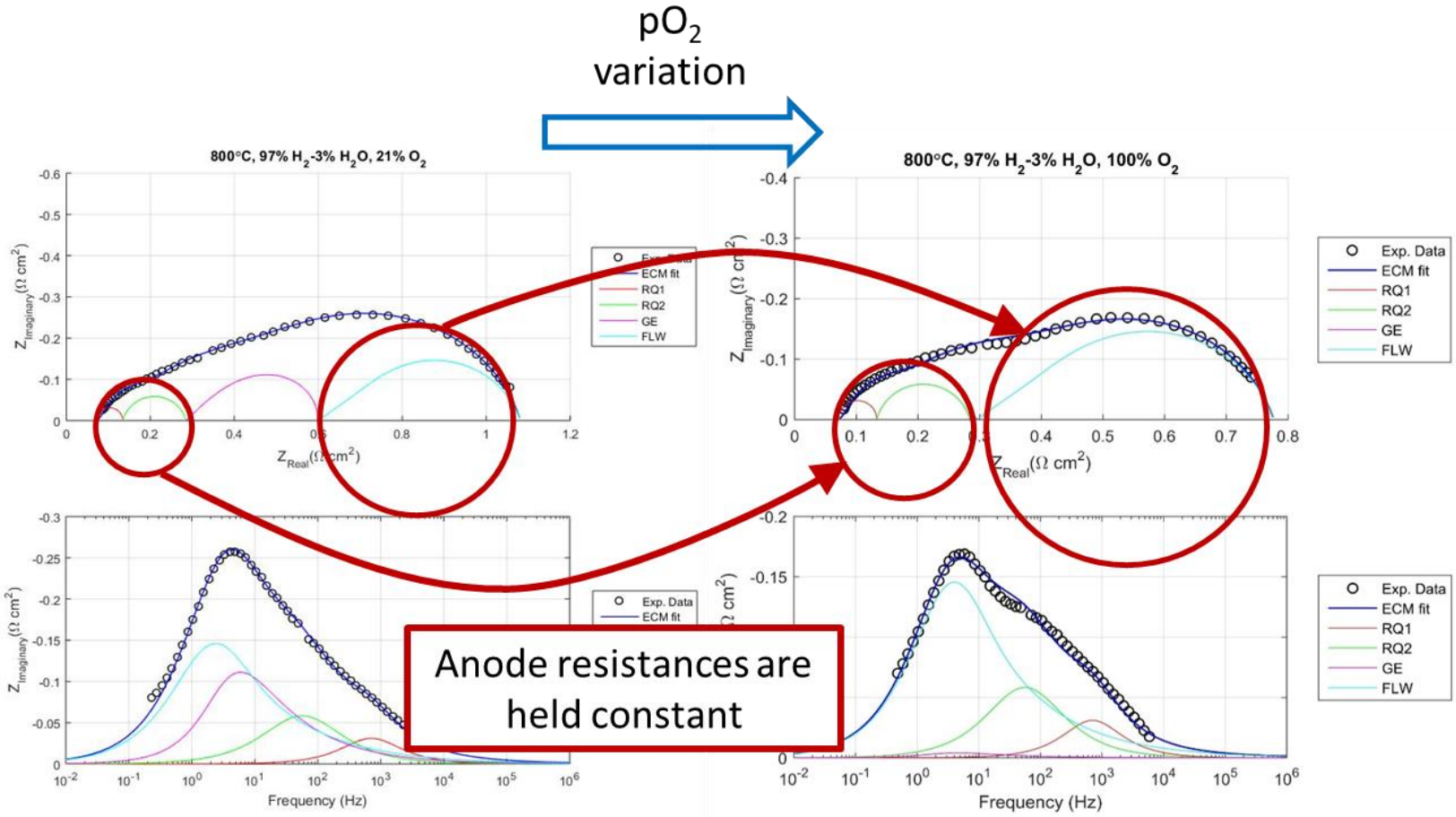

Figure 31: Variation of the cathode gas mixture during batch fitting of EIS data.

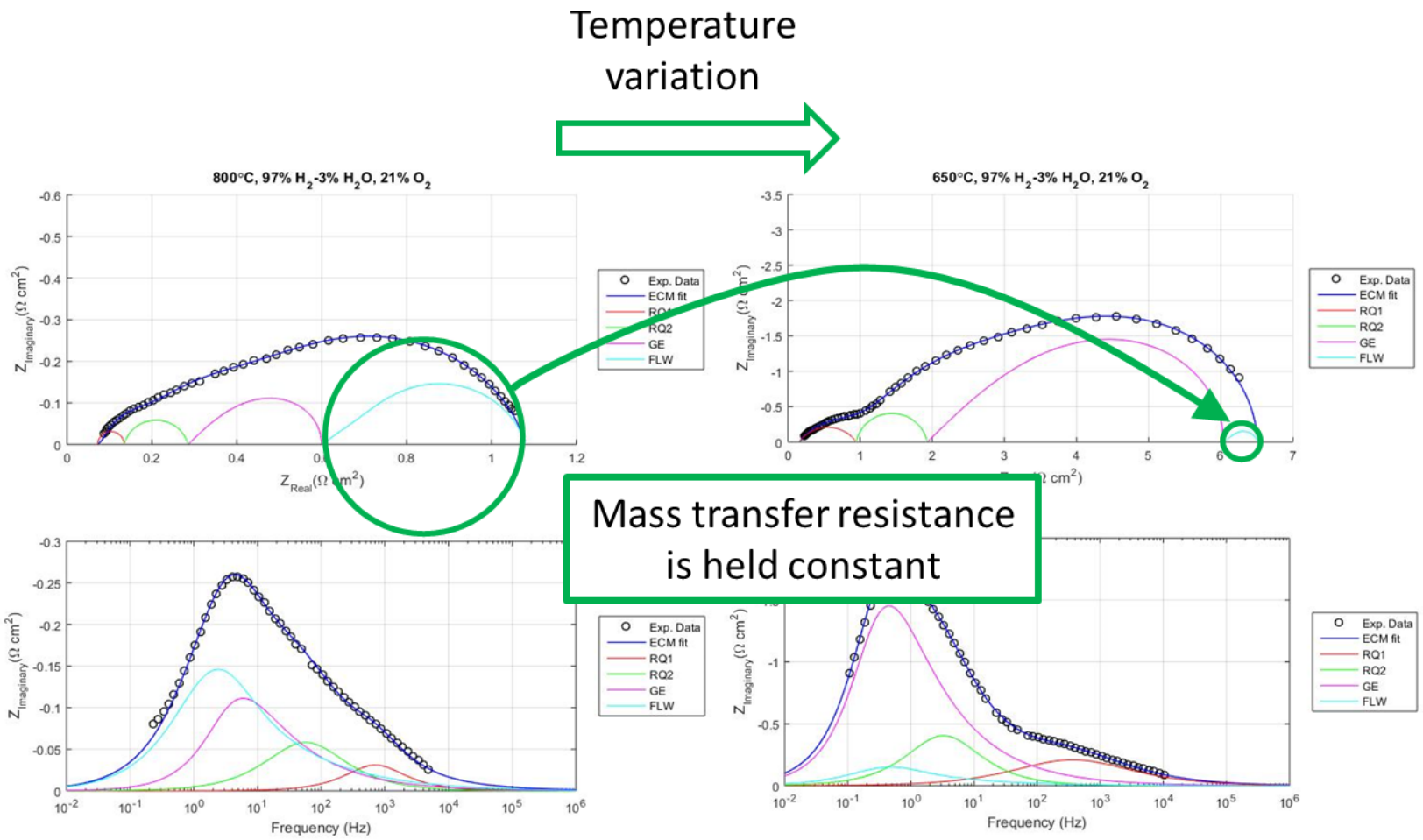

Figure 32: Variation of operating temperature during batch fitting of EIS data.

Validation of the fitted resistance values from the EIS fitting procedure is the last step for ensuring that the results are physically relevant. Two methods for validation are I-V simulation and ensuring that the fitted resistances vary with the expected Arrhenius behavior. I-V simulation is done by using Equation 5 to calculate the I-V response, using the EIS fitting result to fill all free parameters. The free parameters for I-V simulation are the Ohmic resistance, R_{Ohmic}, the exchange current density, i_0, and the anodic mass transfer limited current density, $i_{limit,a}$. R_{Ohmic} is simply the high frequency intercept of the EIS measurement. Exchange current density, i_0, is related to the total charge transfer resistance by the formula [57]:

$$i_0 = \frac{RT}{nF}(R_{Ge} + R_1 + R_2) \tag{17}$$

where R, T, and F have their usual meanings, n is the number of electrons participating in the electrochemical reaction, and R_{Ge}, R_1, and R_2 are fitted resistances representing the cathodic and anodic charge transfer processes. Anodic mass transfer limited current density, $i_{limit,a}$, is related to the anodic mass transfer resistance by the formula [57]:

$$i_{limit,a} = \frac{RT}{2F}\frac{1}{R_{FLW}}\left(1 + \frac{p^0_{H_2}}{p^0_{H_2O}}\right) \tag{18}$$

Where R,T, and F have their usual meanings, $p^0_{H_2}$ and $p^0_{H_2O}$ are the partial pressures of hydrogen and water in the bulk vapor phase, and R_{FLW} is the fitted anodic diffusion resistance. Cathodic mass transfer polarization can be ignored here because it is a negligible component of cell polarization at these operating conditions [37]; for reference, observe how small the contribution of cathodic mass transfer polarization is at potentials greater than 700 mV in Figure 5.

The comparison between simulated I-V and experimental I-V at several different operating conditions can be seen in Figure 33. Note that the choice of the parameter n, which is used for calculating the exchange current density (Equation 17) as well as the charge transfer polarization (Equation 12), makes a clear difference in the shape of the simulated I-V. At higher temperatures, experimental I-V curves show less curvature, and the 'n=1' simulated I-V fits much better, while at lower temperatures, the experimental I-V shows more curvature, and the 'n=2' simulated I-V fits well. Overall, the resistances measured by EIS can be used to simulate the I-V behavior of the cell with little error.

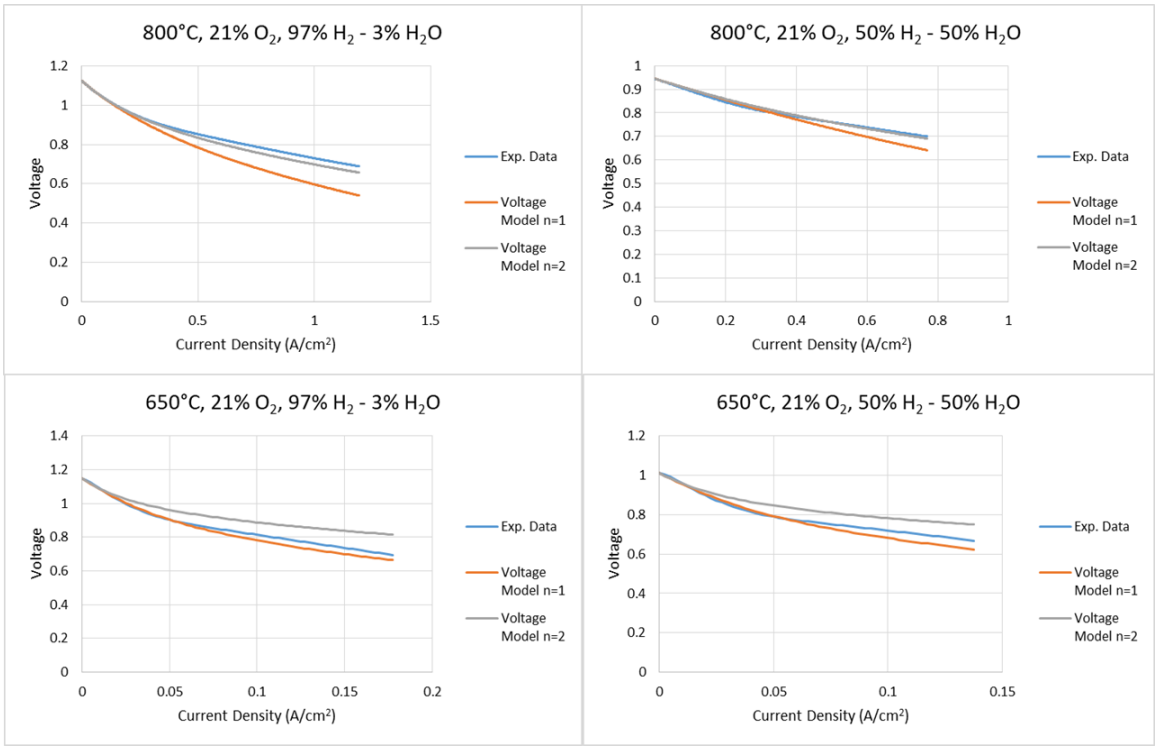

Figure 33: Validation of EIS fitting result by comparison of experimental and simulated I-V curves.

By plotting the natural log of the resistances versus 1/T, it can be validated whether or not cell resistances follow the expected Arrhenius behavior. This plot is

shown in Figure 34. At this operating condition (97% H_2 – 3% H_2O flowing over the anode, 21% O_2 – 79% N_2 flowing over the cathode), cathodic charge transfer (R_{Ge}) is the largest contributor to cell resistance at all temperatures less than 800°C. At 800°C, the anodic mass transfer resistance (R_{FLW}) is the largest resistance, however, anodic mass transfer resistance does not change with temperature, so is not a large contributor to overall cell resistance at temperatures of 700°C and below. The expected Arrhenius behavior of other cell resistances is confirmed by their linearity. The slope of these lines is equal to their activation energy, which is noted on the plot in units of electron-volts.

The activation energies of the cathodic charge transfer and anodic charge transfer reactions identified by this work, 1.55 eV and 1.3 eV, respectively, match well with previously published works. The experimentally measured activation energy for LSM-YSZ composite cathodes has been reported in the range of 1.54 eV to 1.67 eV, matching well with the 1.55 eV shown here [61,113]. The activation energy of hydrogen oxidation in Ni-YSZ electrodes has been reported in the range of 1.1 eV to 1.8 eV [34,44,63,107,115]. Experimental measurements of the activation energy of the hydrogen oxidation reaction using the same ECM as this work on anode-supported SOFCs have reported activation energies in the range of 1.1 eV to 1.3 eV [34,44,63]. This result is on the high end at 1.3 eV, but close enough for confidence in the result. The activation energy of the Ohmic resistance, 0.63 eV, is lower than the 0.8 eV to 0.9 eV reported by other researchers [1,67,116–118]. This difference is not very substantial, due to the relatively small contribution that Ohmic resistance has to overall cell resistance. Overall, comparison of these results to those of other researchers demonstrates the success of this

technique.

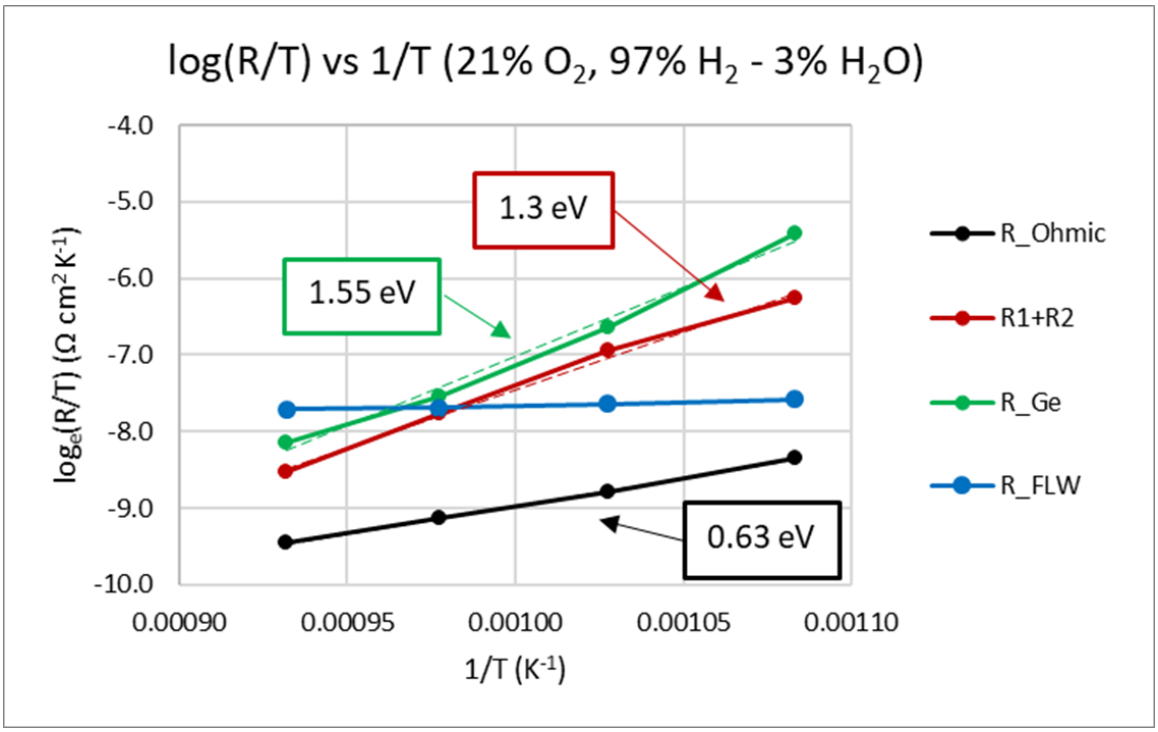

Figure 34: Arrhenius plot of the EIS fitted resistances showing the activation energy of each resistance.

4.4 Electrochemical performance of uninfiltrated, nickel infiltrated, GDC infiltrated, and Ni-GDC infiltrated cells

Electrochemical performance measurements from the uninfiltrated, nickel infiltrated, GDC infiltrated, and Ni-GDC infiltrated cells can be seen in Figure 35. Quantitative performance data from the I-V and EIS measurements is also reported in Table 7. These results show conclusively that Ni-GDC infiltration results in the best cell performance at all temperatures. One clear trend when comparing the performance of the Ni-GDC infiltrated cell to the uninfiltrated cell is that the improvement in performance increases as the operation temperature decreases; as the cell temperature is decreased

from 800°C to 750°C and 700°C, the improvement of both the power as measured by the I-V and the improvement of the polarization resistance as measured by the EIS increase. This is indicative of an improvement in the charge transfer kinetics of the anode, because charge transfer resistance increases quickly when the cell temperature is lowered. The performance of nickel infiltrated and GDC infiltrated cells also follow this trend, indicating that nickel infiltration and GDC infiltration also improve the anodic charge transfer kinetics, but to a lesser extent than infiltration of the Ni-GDC composite. Also, both cells infiltrated with GDC (GDC infiltrated and Ni-GDC infiltrated) show a slight decrease in the measured Ohmic resistance. This is because the infiltration of GDC increases the phase fraction of both the ionic and electronic conducting materials, decreasing the interfacial resistance at the anode-electrolyte interface and decreasing overall cell Ohmic resistance. This increase of the ionic and electronic conducting phase fractions are at the expense of the pore phase fraction, causing a decrease of the effective diffusivity of the anode fuel gas mixture, and an increase of the mass transfer resistance.

When analyzing the I-V performance measurements, it is not easy to distinguish between the effects of nickel infiltration and GDC infiltration, as both cells have nearly identical I-V performance at all temperatures. However, observation of the EIS plots reveals a distinctly different impedance response between the nickel infiltrated cell and the GDC and Ni-GDC infiltrated cells. When examining the Bode plots presented in Figure 35g-i, both cells infiltrated with GDC show an obvious reduction in the impedance response at frequencies greater than 1000 Hz, which is not visible for the nickel infiltrated cell. This is clear evidence that GDC improves the charge transfer kinetics in

the anode active layer in a way that simply infiltrating nickel does not. Additionally, both cells with GDC show an increase in a height and a left-shift to slower frequencies of the anodic mass transfer peak at ~0.5 Hz. This is clearly visible at 800°C, where overall cell performance is anodic mass transfer dominated, as seen in Figure 35g. This increase in anodic mass transfer resistance is due to the filling of pores by the addition of infiltrated material. Despite similar weight gain, the nickel infiltrated cell shows a smaller impact on the anodic mass transfer. This is partially because the nickel is about 25% more dense than GDC, and consumes less pore volume when infiltrated to the same weight gain as GDC.

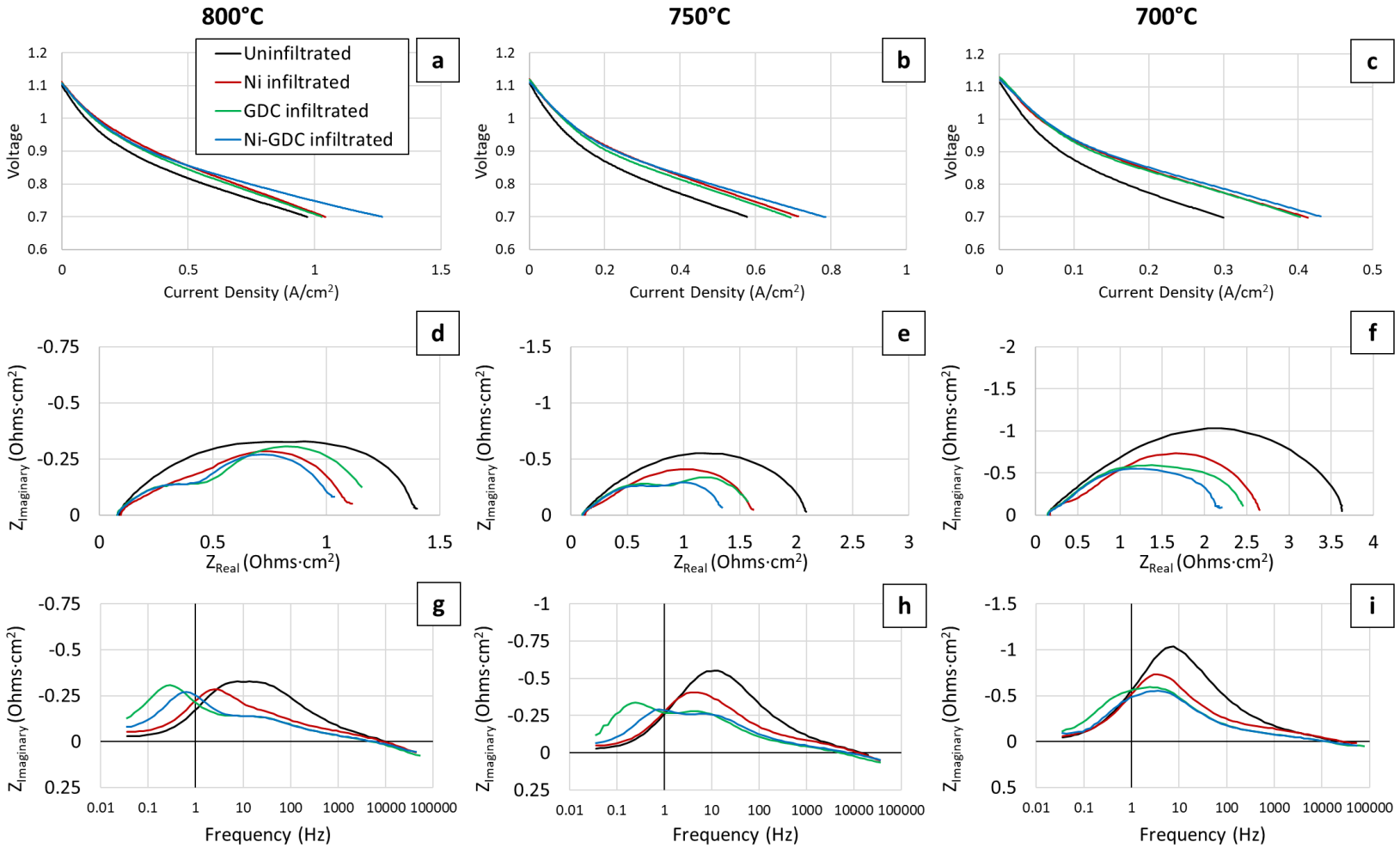

Figure 35: (a-c) I-V and (d-i) EIS measurements of uninfiltrated, Ni infiltrated, GDC infiltrated, and Ni-GDC infiltrated cells at 800°C, 750°C, and 700°C. All measurements were recorded while flowing 97% H_2 – 3% H_2O over the anode and 21% O_2 – 79% N_2 over the cathode.

Measurement:	Temperature:	Uninfiltrated	Ni infiltrated		GDC infiltrated		Ni-GDC infiltrated	
		Value:	Value:	Change:	Value:	Change:	Value:	Change:
R_{Pol} ($\Omega \cdot cm^2$)	**800°C**	1.31	1.02	-22%	1.08	-18%	0.95	-27%
	750°C	1.97	1.49	-24%	1.47	-26%	1.23	-38%
	700°C	3.47	2.49	-28%	2.31	-33%	2.05	-41%
R_{Ohmic} ($\Omega \cdot cm^2$)	**800°C**	0.09	0.09	+5%	0.08	-14%	0.08	-10%
	750°C	0.12	0.12	+7%	0.10	-15%	0.11	-8%
	700°C	0.16	0.17	+5%	0.14	-13%	0.15	-5%
Power density at 750 mV ($W \cdot cm^{-2}$)	**800°C**	0.57	0.65	+14%	0.63	+11%	0.74	+30%
	750°C	0.34	0.44	+30%	0.42	+25%	0.47	+39%
	700°C	0.17	0.25	+47%	0.25	+46%	0.27	+56%

Table 7: Performance data from I-V and EIS measurements of uninfiltrated, Ni infiltrated, GDC infiltrated, and Ni-GDC infiltrated cells. All measurements were recorded while flowing 97% H_2 – 3% H_2O over the anode and 21% O_2 – 79% N_2 over the cathode.

While the EIS measurements do show a clear decrease of the anodic charge transfer resistance and a clear increase of the anodic mass transfer resistance after all infiltrations, it is not possible to quantify those changes from the I-V and EIS information presented in Figure 35 and Table 7 alone. One straightforward way to quantify the impact

of infiltration on the anodic mass transfer resistance is to conduct an I-V until the anodic mass transfer limited current density is reached. This was conducted at 800°C while flowing 97% H_2 – 3% H_2O over the anode and 100% O_2 over the cathode to prevent any cathodic mass transfer limitation. These measurements are shown in Figure 36. While all infiltrated cells have better performance than the uninfiltrated cell at current densities less than 1.5 $A \cdot cm^{-2}$, the infiltrated cells become mass transfer limited at lower current densities than the uninfiltrated cell. The GDC infiltrated cell shows the worst anodic mass transfer kinetics, while the nickel infiltrated and Ni-GDC infiltrated cells have a similar behavior. The measured anodic mass transfer limited current density, which is defined here as the current density at 400 mV, can be compared with the porosity measurement reported in Section 3.2. This comparison is shown in Table 8. These two measurements show good agreement, so both methods are suitable for quantifying the effect of infiltration on anodic mass transfer. This is useful information because SOFC stacks cannot be operated up to anodic mass transfer limited current densities, and thus cannot be characterized in that manner.

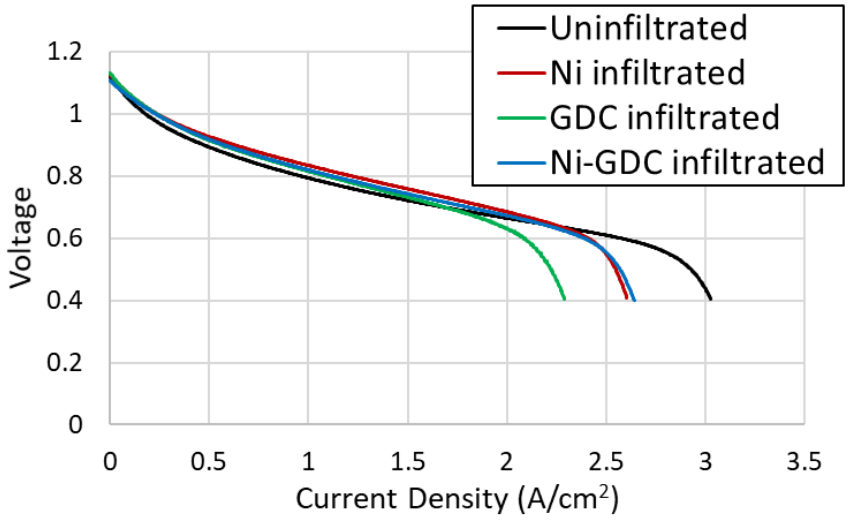

Figure 36: I-V scans showing the anodic mass transfer limited current density of uninfiltrated, Ni infiltrated, GDC infiltrated, and Ni-GDC infiltrated cells. Scans were recorded at 800°C while flowing 97% H_2 – 3% H_2O over the anode and 100% O_2 over the cathode.

Cell:	Uninfiltrated	Ni infiltrated		GDC infiltrated		Ni-GDC infiltrated	
	Value:	Value:	Change:	Value:	Change:	Value:	Change:
Current density at 400 mV ($A \cdot cm^{-2}$) (800°C, 97% H_2 - 3% H_2O, 100% O_2)	3.04	2.61	-14%	2.30	-24%	2.64	-13%
Average porosity	20.6%	17.4%	-15.8%	16.3%	-20.9%	17.1%	-17.3%

Table 8: Changes in anodic mass transfer limited current density and average porosity after infiltration with Ni, GDC, and Ni-GDC.

Quantification of the anodic charge transfer resistance requires the use of EIS fitting with an equivalent circuit model. This procedure was previously described in detail in Section 4.3. The results from EIS fitting on an uninfiltrated cell were used as initial guesses to fit the ECM to the EIS measurements from the uninfiltrated and infiltrated cell data shown in Figure 35. Also, the initial guess for the anodic mass transfer resistance of each cell was calculated from the anodic mass transfer limited current density measurements shown in Figure 36 using Equation 18.

The results of the EIS fitting are summarized in Figure 37. Figure 37a shows the impact of infiltration on the anodic charge transfer resistance. While nickel infiltration does slightly improve the anodic charge transfer compared to the uninfiltrated cell, the introduction of GDC has caused the activation energy of the anodic charge transfer reaction to decrease from 1.29 eV to 0.74 eV. This result is supported by the literature review of the anodic charge transfer reaction between nickel and GDC previously discussed in Section 2.5.2; cells with nickel and GDC report activation energies for the anodic charge transfer reaction as being between 0.5 eV to 0.85 eV, and this result is in agreement with those measurements. This change in the activation energy of the anodic charge transfer resistance can be compared to the change in Ohmic resistance after GDC infiltration, shown in Figure 37b; while GDC does decrease the Ohmic resistance slightly, there is no change in the activation energy for oxygen ion conduction. These effects make sense based on the microstructure of the infiltrated cells. Infiltrated GDC is on the surface of the nickel and YSZ cermet grains. Anodic charge transfer reactions occur on the surfaces of the electrode materials, while oxygen ion diffusion occurs mostly

through the bulk of YSZ grains and at YSZ/YSZ grain boundaries within the electrolyte. Thus, infiltrated GDC is structured in a way that substantially improves anodic charge transfer kinetics and only slightly improves Ohmic resistance.

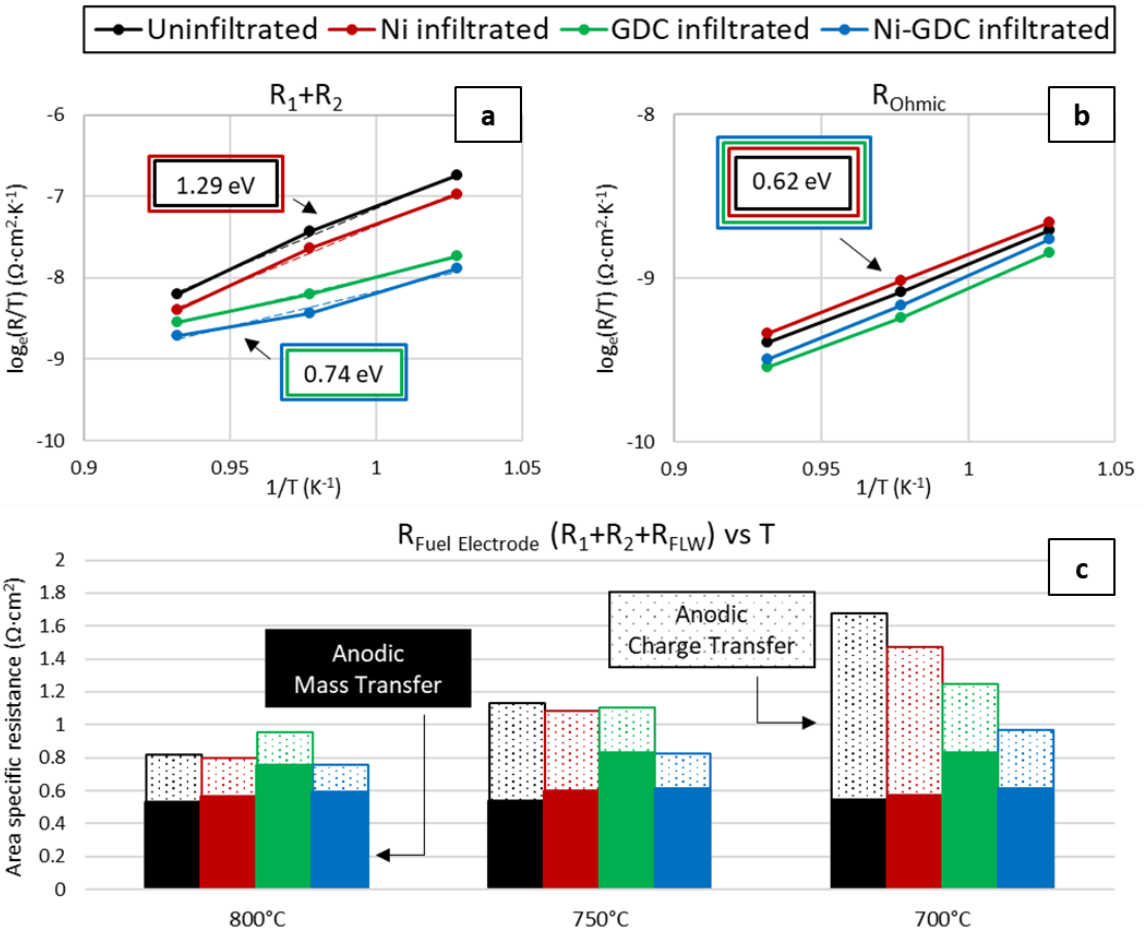

Figure 37: Cell performance measurements from EIS modeling of uninfiltrated, Ni infiltrated, GDC infiltrated, and Ni-GDC infiltrated cells. (a) Arrhenius plot of the anodic charge transfer resistance. (b) Arrhenius plot of the Ohmic resistance. (c) Comparison of the relative contributions of anodic charge transfer and anodic mass transfer to the overall fuel electrode resistance at 800°C, 750°C, and 700°C.

The mechanism by which infiltrated GDC improves the kinetics of the anodic charge transfer reaction has been explored in detail by other researchers [100,119–122]. Because GDC has higher oxygen ion diffusivity than YSZ, GDC enables faster transport of oxygen ions to TPBs than YSZ. Furthermore, because GDC is a mixed ionic-electronic

conductor, the charge transfer reaction can also occur anywhere on the surface of GDC, effectively creating a ‘two-phase charge-transfer boundary’ or 2PB. Electrochemical reactions at these 2PBs can occur in parallel with the Ni-YSZ and Ni-GDC TPBs. In this work, the composite of infiltrated nickel and infiltrated GDC demonstrates the best performance, showing that the GDC and the nickel nanoparticles are both useful for improving the performance of the electrode. This is in agreement with the results of other researchers, who have also shown that the combination of GDC and metallic nanoparticle TPBs results in better performance than either alone [119–122]. This conclusion is somewhat disputed, with a detailed patterned anode study by Chueh et. al. demonstrating that the performance of GDC is totally unaffected by the presence of Pt nanowires, indicating that the Pt-GDC TPBs are not useful compared to the GDC 2PB [100]. Regardless, it is clear from this work that the infiltration of GDC within the Ni-YSZ electrode results in the reduction of the activation energy for the anodic charge transfer reaction, improving electrode performance.

The relative contributions of anodic charge transfer and anodic mass transfer resistances to the resistance of the fuel electrode are shown in Figure 37c. At 800°C, charge transfer kinetics are rapid, and anodic mass transfer resistance dominates the resistance of the electrode. As the operation temperature of the cell is reduced, the anodic mass transfer resistance does not change, while the anodic charge transfer begins to increase substantially. At 700°C, the impact of infiltration on the anodic charge transfer resistance can be clearly observed; the anodic charge transfer resistance of the Ni-GDC infiltrated cell is approximately 1/3 of that of the uninfiltrated cell. Also note that the

impact of anodic mass transfer is not negligible even at lower temperatures, as the difference in total fuel electrode resistance between the GDC and Ni-GDC infiltrated cells is almost entirely due to mass transfer. Reducing GDC loading in both the GDC infiltrated and Ni-GDC infiltrated cells may result in even better cell performance. It is difficult to model this precisely, because it is not known what the minimum useful loading of infiltrated GDC is. This question deserves further study. With that being said, if the volume of infiltrated GDC was halved, the negative impact of GDC infiltration on the anodic mass transfer resistance would also be halved, as seen in Equations 9 and 11.

EIS fitting of the uninfiltrated, nickel infiltrated, GDC infiltrated, and Ni-GDC infiltrated cells was validated using comparison of experimental and simulated I-V data. This comparison is shown in Figure 38. Because the cell temperature shown here is relatively high, the ‘n=2’ I-V model fits the best. The simulated and experimental I-V all show good agreement, demonstrating that the resistances measured by EIS fitting are representative of the cell performance.

The repeatability of cell performance with infiltration is crucial for proving its performance improvement. During the course of this work, several cells of each kind were tested. I-V measurements demonstrating repeatable cell performance are shown in Figure 39. Only one GDC cell was successfully tested, so its repeatability is not shown here, but from the results of the other infiltrated cells, it is expected to demonstrate repeatable performance as well.

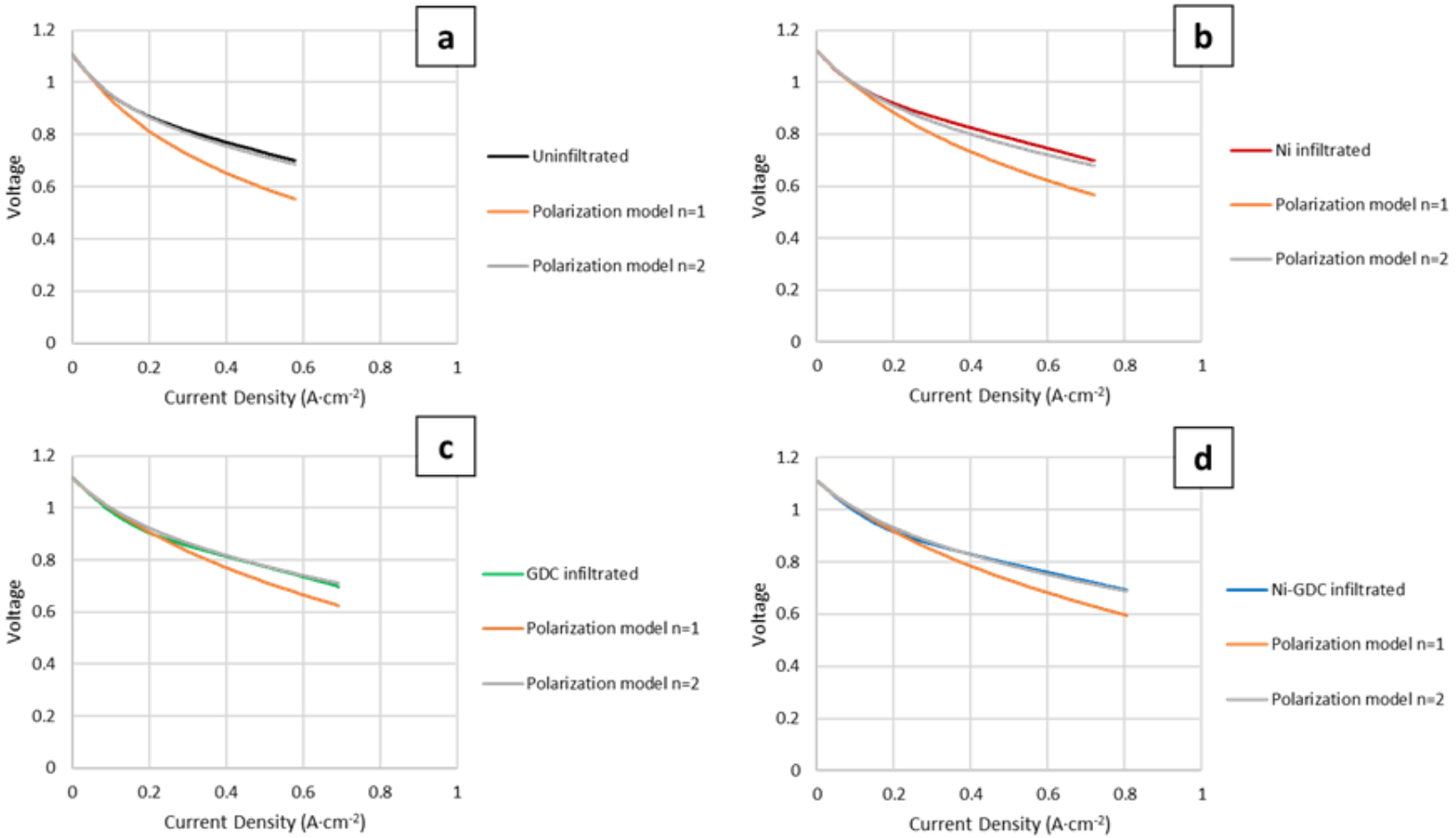

Figure 38: Validation of EIS fitting of (a) uninfiltrated, (b) Ni infiltrated, (c) GDC infiltrated, and (d) Ni-GDC infiltrated cells by comparison of experimental and simulated I-V curves.

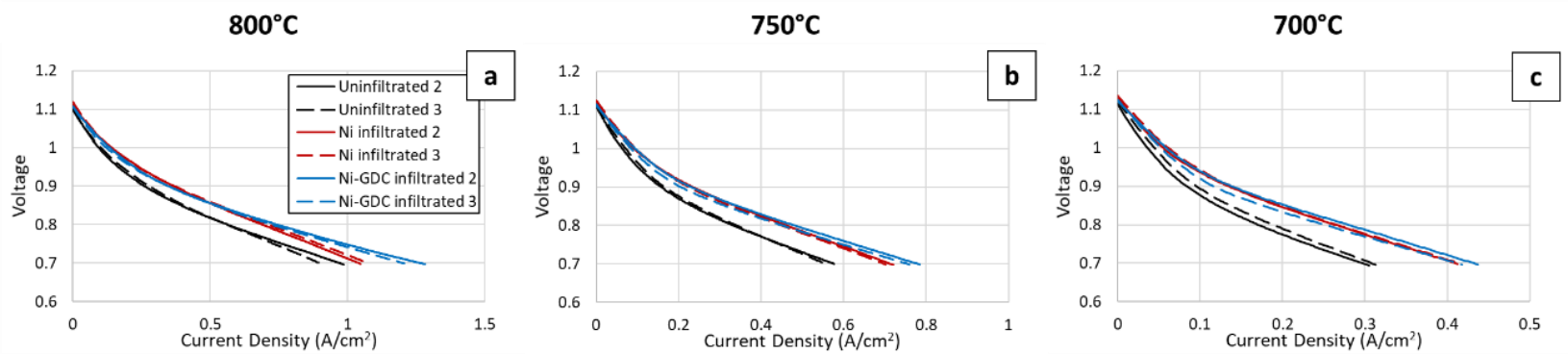

Figure 39: Repeatability of uninfiltrated and infiltrated cell performance.

3.4 Durability of infiltrated materials after exposure to anodic mass transfer limited currents and 120 hours of constant current

The stability of the uninfiltrated and infiltrated cells was investigated by exposing cells to accelerated degradation under anodic mass transfer limited current, and then testing cells at 1 $A \cdot cm^{-2}$ current for 120 hours. Electrochemical data from the anodic mass transfer limited current exposure tests are shown in Figure 40. As can be seen in the I-V-t plots, anodic mass transfer limited current exposure was conducted using three I-V scans up to the anodic mass transfer limit in addition to 24 minutes of constant current at the anodic mass transfer limit. The constant current measurements are useful, as the slope of the voltage measurement during constant current allows for straightforward analysis. The result from the uninfiltrated cell (Figure 40a) shows no obvious change in the cell performance during this procedure. The result from the nickel infiltrated cell (Figure 40b) shows a slight increase in cell voltage during constant current, indicating a small improvement in mass transfer kinetics. This may be due to the coarsening of nickel nanoparticles, because reducing the density of nickel nanoparticles makes them less likely to constrict gas flow in the small pores of the anode active layer. In comparison, the results from the GDC and Ni-GDC infiltrated cells (Figure 40c and Figure 40d, respectively) show a decrease in cell voltage during constant current. A possible reason for this is because GDC nanoparticles are more stable, so during high current they may agglomerate rather than coarsen as nickel nanoparticles do. Agglomerated structures have very high surface roughness compared to coarsened structures, which could make gas diffusion more tortuous and increase resistance.

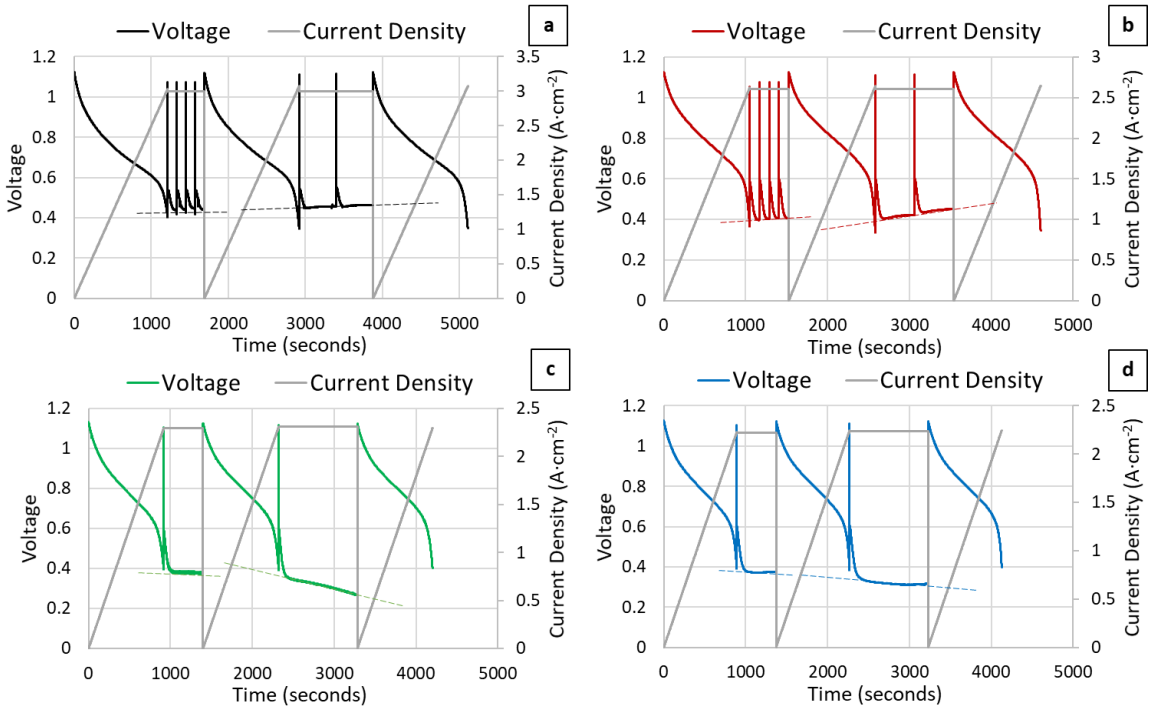

Figure 40: I-V-t plots of the anodic mass transfer limited current exposure test from (a) an uninfiltrated cell, (b) a Ni infiltrated cell, (c) a GDC infiltrated cell, and (d) a Ni-GDC infiltrated cell. Exposure tests were conducted at 800°C while flowing 97% H_2 – 3% H_2O over the anode and 100% O_2 over the cathode.

After exposure to anodic mass transfer limited current, cells were galvanostatically tested at a constant current of 1 $A \cdot cm^{-2}$ for 120 hours. The measured voltage during the application of current is shown in Figure 41. During this time, all cells experience performance improvement, which is attributable to changes in the cathode. Improvement in the performance of LSM-YSZ composite cathodes under cathodic polarization is well documented in the literature [123–126]. Comparing the change in performance between cells over time shows the stability of infiltrants within the anode. While the nickel infiltrated and GDC infiltrated cells show nearly identical performance initially, after about 50 hours of constant current the GDC infiltrated cell demonstrates better performance than the nickel infiltrated cell. By 120 hours, the performance of the

nickel infiltrated cell has degraded to be nearly equal to the performance of the uninfiltrated cell. The Ni-GDC infiltrated cell maintained the best performance throughout the entire duration of the test.

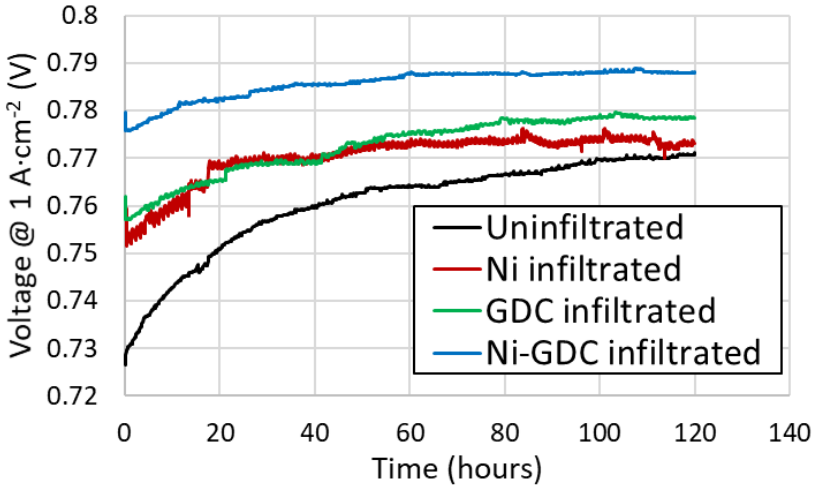

Figure 41: Voltage during 1 A cm^{-2} constant current. This was conducted at 800°C while flowing 97% H_2 – 3% H_2O over the anode and 21% O_2 – 79% N_2 over the cathode.

The microstructures of the infiltrated cells corroborate the results from the electrochemical stability tests. The microstructures of the nickel infiltrated, GDC infiltrated, and Ni-GDC infiltrated electrodes within the anode active layer after electrochemical stability testing are shown in Figure 42. Two regions of interest are shown: a region under the cathode, which is electrochemically active during cell operation, and a region not under the cathode, which is electrochemically inactive and does not experience any electrochemical reactions. These regions are shown on a schematic of the cell cross-section in Figure 42a. The microstructures before exposure to the electrochemical stability tests (Figure 42b-d) all demonstrate successful infiltration of nano-scale features. However, after the exposure to anodic mass transfer limited current

and 120 hours of constant current, the microstructures differ dramatically. The nickel infiltrated cell has completely lost all nickel nanoparticles with diameters less than 100 nm in the electrochemically active region, explaining why the performance of the nickel infiltrated and uninfiltrated cells was nearly equal after the 120 hours of constant current. In the electrochemically inactive region of the nickel infiltrated cell, the nanoparticles are somewhat coarsened compared to the untested cell, but particle diameter and coverage are still relatively good. It is clear from this result that exposure to high humidity within the anode active layer during current is the driving force for nickel nanoparticle coarsening.

In comparison, both the GDC infiltrated and Ni-GDC infiltrated cells show much better stability after exposure to anodic mass transfer limited current and 120 hours of constant current. Both cells maintain small particle sizes, homogenous surface coverage, and good nanoparticle connectivity in the electrochemically active region of the electrode after the experiment. When comparing the electrochemically active and inactive regions of the GDC infiltrated and Ni-GDC infiltrated electrodes, it appears that exposure to electrochemical current actually causes some wetting of GDC, as the infiltrated material is more homogenously distributed in the electrochemically active region. The stability of infiltrated GDC and Ni-GDC nanoparticles in Ni-YSZ cermet electrodes is a promising result for their use as an effective and stable catalysts in commercial SOFCs.

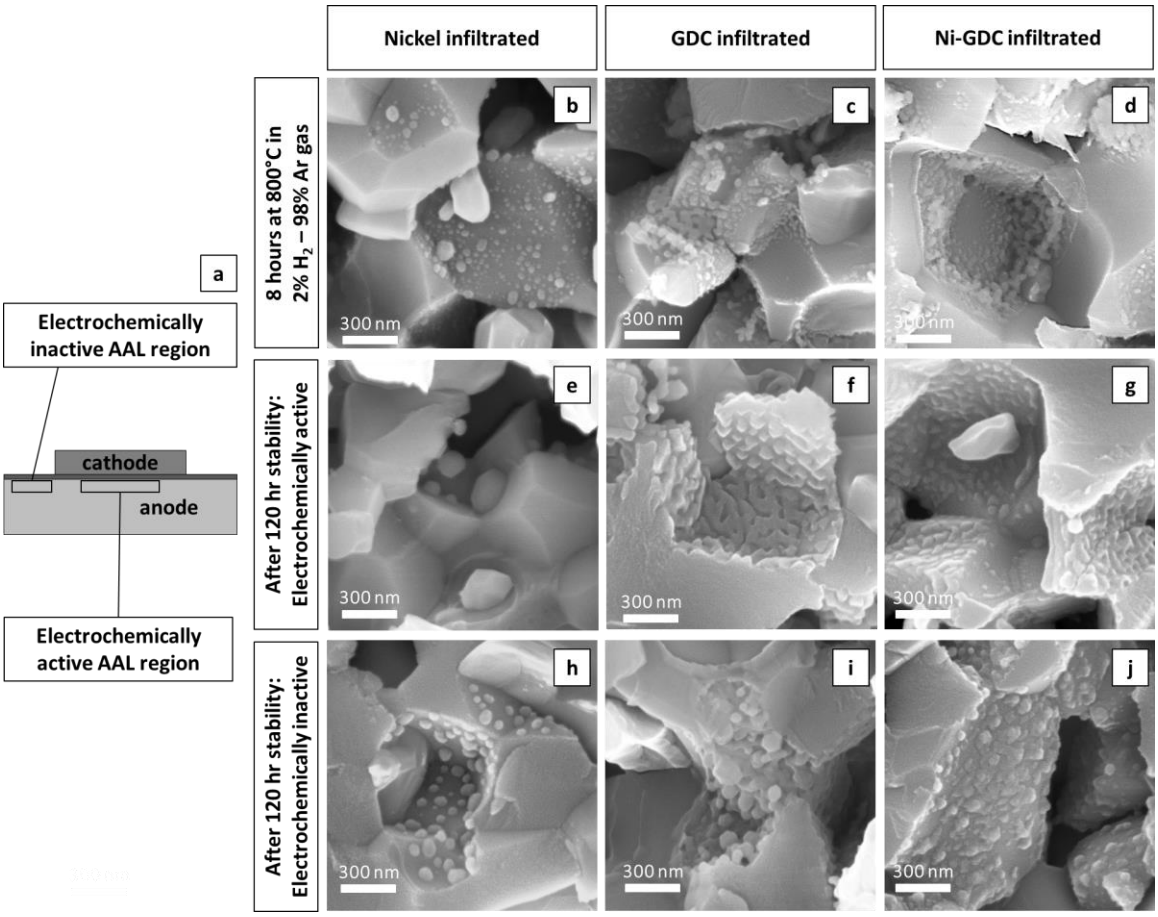

Figure 42: (a) Schematic showing the locations of electrochemically inactive and electrochemically active AAL regions. (b-j) SEM images of fracture cross-sections from infiltrated cells after exposure to anodic mass transfer limited current and 120-hour stability measurement.

5. CONCLUSIONS AND FURTHER WORK

The work presented in this dissertation has explored infiltration of nickel, GDC, and Ni-GDC into Ni-YSZ cermet anodes as a cheap and rapid means of improving electrode performance. Key issues preventing the adoption of nickel nanoparticle infiltration are the lack of connectivity between nickel nanoparticles and the instability of nickel nanoparticles during electrochemical testing. Two approaches were identified from literature (reviewed in Section 2) for connecting and activating infiltrated nickel nanoparticles in Ni-YSZ cermets: spreading nickel nanoparticles in-situ by exposure to high humidity, and connecting nickel nanoparticles by simultaneous infiltration of nickel and gadolinium-doped ceria, which is a fluorite oxide with mixed ionic electronic conductivity. The experimental work presented in Sections 3 and 4 investigates these two different means for connecting nickel nanoparticles.

Section 3 studied the behavior of infiltrated nickel nanoparticles when exposed to high humidity at anodic mass transfer limited currents, which causes nickel nanoparticles to spread and connect with each other, activating them and improving the performance of the electrode. This behavior was studied by comparing the performance of nickel nanoparticle infiltrated cells exposed to high humidity with those not exposed to high humidity. It was found that without spreading, nickel infiltration does not substantially improve cell performance, but after spreading, cell performance was improved significantly. However, in-situ nickel spreading inherently causes the coarsening of nickel nanoparticles, increasing their particle size and reducing the density of electrochemically active sites within the electrode. Thus, activation of nickel

nanoparticles by in-situ spreading is not a candidate for improving the long-term performance of Ni-YSZ cermet electrodes.

Section 4 examined the impact of nickel, GDC, and Ni-GDC infiltration on the performance of Ni-YSZ cermet electrodes. By infiltrating nickel and GDC separate from one another, and comparing the performance with that of their composite, this work clearly revealed the role that each material plays in the performance and stability of the infiltrated electrodes. All infiltrated cells showed improved performance compared with an uninfiltrated cell, with the Ni-GDC composite demonstrating the highest performance in all conditions. Qualitative analysis of the I-V and EIS measurements revealed that the introduction of GDC into the electrode results in an obvious improvement to the anodic charge transfer reaction, but infiltrated GDC also has a larger negative impact on the anodic mass transfer resistance than infiltrated nickel. This is due to the lower density of GDC than of nickel; similar weights of GDC and nickel were infiltrated, and the infiltrated GDC occupies more volume than infiltrated nickel, reducing the diffusivity of the electrode. The effect of infiltration on anodic mass transfer was quantified both by I-V as well as porosity measurement using SEM image analysis, directly supporting the electrochemical measurements with microstructural analysis.

Quantifying the impact of infiltration on the anodic charge transfer resistance required fitting the EIS data with an equivalent circuit model. This procedure enables the deconvolution of all cell resistances, but needs to be implemented with care. Detailed explanation of the EIS fitting procedure is given in Section 4.3. Results from EIS fitting show that nickel infiltration slightly improves anodic charge transfer, but does not have

any impact on the activation energy of the charge transfer reaction. Infiltration of GDC into the electrode substantially decreases the anodic charge transfer resistance, reducing the activation energy from 1.3 eV to 0.74 eV. This was measured in both the GDC and Ni-GDC infiltrated cells, with the Ni-GDC infiltrated cell demonstrating the lowest anodic charge transfer resistance of all cells tested. At 700°C, the anodic charge transfer resistance of the Ni-GDC infiltrated cell is only about 1/3 of that of the uninfiltrated cell.

The stability of the infiltrated cells during exposure to electrochemical current was also studied. As in Section 3, it was found that infiltrated nickel was prone to coarsening during electrochemical testing. After exposure to anodic mass transfer limited current and 120 hours of 1 $A \cdot cm^{-2}$ constant current at 800°C, the performance of the nickel infiltrated electrode was nearly identical to that of an uninfiltrated electrode. This was corroborated by the microstructural analysis. Before testing, nickel nanoparticles with diameters of 50 nm and less are homogenously distributed throughout the electrode, but after testing, nanoparticles have all coarsened to diameters larger than 100 nm, and are no longer evenly distributed. In comparison, infiltrated GDC and Ni-GDC structures showed no clear signs of coarsening after electrochemical testing. This was mirrored by the electrochemical measurements during constant current, which showed stable performance improvement over the entire duration of the test.

This work demonstrates that GDC and Ni-GDC infiltration are simple and effective procedures for improving the electrochemical performance of Ni-YSZ cermet electrodes. Further work should be conducted on optimizing this technique. Because infiltration negatively impacts the mass transfer kinetics of the electrode, it is important

to minimize the added volume of infiltrated material, and it is unclear what the minimum amount of GDC required for performance improvement might be. Also, the relative amounts of Ni and GDC that are infiltrated will likely affect the electrochemical performance and stability of the infiltrated structures. In general, the use of infiltration to improve the electrochemical performance of Ni-YSZ cermet electrodes for SOFCs is very promising, and should continue to be explored.

APPENDIX 1: MATLAB I-V Fitting Code (n=1)

Contents


```
function [fitted_params, res_error] = iv_fit_n1(exp_data, exp_conditions,
fit_ratio, params, lb, ub)
```

Setup

```
%Paul Gasper, 2018, Boston University

% This function fits an IV curve using various contributions to
% polarization, depending on the input conditions. The number of electrons
% contributing to the electrochemical reaction when calculated the
% activation polarization using the Butler-Volmer equation is assumed to be
% 1 for this polarization model.


%Input Data Structures:
%Experimental IV data:
%Current Density, Voltage
%   x1              y1
%   x2              y2
%   ...             ...
%   xn              yn

%Experimental Conditions:
%Temperature (Celsius), fuel pH2 (assuming pH2-pH2O balance), fuel pO2
%     data,        data,                            data

%Param guesses, lower bounds, upper bounds:
%   R0,    i0,    ias,    ics
%   data,  data,  data,   data

%Output Data Structures:
%Fitted parameters
%   R0,    i0,    ias,    ics,    Rp
%   data,  data,  data,   data,   data

%Residual error
%   data

T = exp_conditions(1)+273.15;
F = 96485.3329;
```

```
R = 8.3144598;
pH2 = exp_conditions(2);
pH2O = 1-pH2;
pO2 = exp_conditions(3);

fit_limit = int64(length(exp_data(:,1))*fit_ratio);
current = exp_data(1:fit_limit,1);
exp_voltage = exp_data(1:fit_limit,2);
ocv = ones(fit_limit,1).*exp_data(1,2);
```

Minimize the model and plot the results

```
%minimize the model function's error versus the data
A = []; Aeq = [];
b = []; beq = [];
[fitted_params, res_error] = ...
    fmincon(@polarization_model, params, A, b, Aeq, beq, lb, ub);

%calculate polarization losses vs current and plot everything
ohm_pol = ohmic(current, fitted_params(1));
act_pol = activation(current, fitted_params(2));
anode_conc_pol = anodic_conc(current, fitted_params(3));
if pO2 == 1
    fit = ocv - ohm_pol - act_pol - anode_conc_pol;
    fitted_params(5) = ((R*T)/(F*fitted_params(2)))+...
         ((R*T)/(2*F))*(1/fitted_params(3))*(1+(pH2/pH2O));
else
    cathode_conc_pol = cathodic_conc(current, fitted_params(4));
    fit = ocv - ohm_pol - act_pol - anode_conc_pol - cathode_conc_pol;
    fitted_params(5) = ((R*T)/(F*fitted_params(2)))+...
         ((R*T)/(2*F))*(1/fitted_params(3))*(1+(pH2/pH2O))+...
         ((R*T)/(4*F))*(1/fitted_params(4));
end

figure()
hold on
plot(exp_data(:,1),exp_data(:,2),'k-')
plot(current, fit, 'r-')
plot(current, ocv, 'b-')
plot(current, ocv-ohm_pol, 'b--')
plot(current, ocv-ohm_pol-act_pol, 'b-.')
plot(current, ocv-ohm_pol-act_pol-anode_conc_pol, 'b:')
legend('Data','Fit','Polarization Components','Location','south')
xlabel('Current Density (A cm^{-2})');
ylabel('Voltage');
ylim ([0 1.2])
grid on
```

```
hold off
```

Calculating total squared error of the fit

```
function err = polarization_model(params)
    if pO2 == 1
        model = ocv(1)-ohmic(current, params(1))-activation(current,
params(2))-...
                anodic_conc(current, params(3));
    else
        model = ocv(1)-ohmic(current, params(1))-activation(current,
params(2))-...
                anodic_conc(current, params(3))-cathodic_conc(current,
params(4));
    end

    err = sum((exp_voltage - model).^2);
end
```

Polarization Components Functions

```
function dat = ohmic(x, R0)
%calculated ohmic polarization at the given current values
    dat = x.*R0;
end

function dat = activation(x, i0)
    %calculated activation polarization at given current values
    dat = ((2*R*T)/F)*log(0.5*((x./i0)+sqrt(((x./i0).^2)+4)));
end

function dat = cathodic_conc(x, ics)
    %calculated cathodic concentration polarization at given current values
    dat = -((R*T)/(4*F))*log(1-(x./ics));
end

function dat = anodic_conc(x, ias)
    %calculated anodic concentration polarziation at given current values
    dat = -((R*T)/(2*F))*log(1-(x./ias)) +
((R*T)/(2*F))*log(1+((pH2.*x)./(pH2O*ias)));
end
end
```

Published with MATLAB® R2015b

APPENDIX 2: MATLAB I-V Fitting Code (n=2)

Contents


```
function [fitted_params, res_error] = iv_fit_n2(exp_data, exp_conditions,
fit_ratio, params, lb, ub)
```

Setup

```
%Paul Gasper, 2018, Boston University

% This function fits an IV curve using various contributions to
% polarization, depending on the input conditions. The number of electrons
% contributing to the electrochemical reaction when calculated the
% activation polarization using the Butler-Volmer equation is assumed to be
% 2 for this polarization model.

%Input Data Structures:
%Experimental IV data:
%Current Density, Voltage
%   x1              y1
%   x2              y2
%   ...             ...
%   xn              yn

%Experimental Conditions:
%Temperature (Celsius), fuel pH2 (assuming pH2-pH2O balance), fuel pO2
%     data,        data,                              data

%Param guesses, lower bounds, upper bounds:
%   R0,    i0,    ias,    ics
%   data,  data,  data,   data

%Output Data Structures:
%Fitted parameters
%   R0,    i0,    ias,    ics,    Rp
%   data,  data,  data,   data,   data

%Residual error
%   data

T = exp_conditions(1)+273.15;
F = 96485.3329;
R = 8.3144598;
```

```
pH2 = exp_conditions(2);
pH2O = 1-pH2;
pO2 = exp_conditions(3);

fit_limit = int64(length(exp_data(:,1))*fit_ratio);
current = exp_data(1:fit_limit,1);
exp_voltage = exp_data(1:fit_limit,2);
ocv = ones(fit_limit,1).*exp_data(1,2);
```

Minimize the model and plot the results

```
%minimize the model function's error versus the data
A = []; Aeq = [];
b = []; beq = [];
[fitted_params, res_error] = ...
    fmincon(@polarization_model, params, A, b, Aeq, beq, lb, ub);

%calculate polarization losses vs current and plot everything
ohm_pol = ohmic(current, fitted_params(1));
act_pol = activation(current, fitted_params(2));
anode_conc_pol = anodic_conc(current, fitted_params(3));
if pO2 == 1
    fit = ocv - ohm_pol - act_pol - anode_conc_pol;
    fitted_params(5) = ((R*T)/(2*F*fitted_params(2)))+...
         ((R*T)/(2*F))*(1/fitted_params(3))*(1+(pH2/pH2O));

    figure()
    hold on
    plot(exp_data(:,1),exp_data(:,2),'k-')
    plot(current, fit, 'r-', 'LineWidth', 1)
    plot(current, ocv, 'b-')
    plot(current, ocv-ohm_pol, 'b--')
    plot(current, ocv-ohm_pol-act_pol, 'b-.')
    legend('Data','Fit','Polarization Components','Location','south')
    xlabel('Current Density (A cm^{-2})');
    ylabel('Voltage');
    ylim ([0 1.2])
    grid on
    hold off
else
    cathode_conc_pol = cathodic_conc(current, fitted_params(4));
    fit = ocv - ohm_pol - act_pol - anode_conc_pol - cathode_conc_pol;
    fitted_params(5) = ((R*T)/(2*F*fitted_params(2)))+...
         ((R*T)/(2*F))*(1/fitted_params(3))*(1+(pH2/pH2O))+...
         ((R*T)/(4*F))*(1/fitted_params(4));

    figure()
    hold on
```

```
    plot(exp_data(:,1),exp_data(:,2),'k-')
    plot(current, fit, 'r-', 'LineWidth', 1)
    plot(current, ocv, 'b-')
    plot(current, ocv-ohm_pol, 'b--')
    plot(current, ocv-ohm_pol-act_pol, 'b-.')
    plot(current, ocv-ohm_pol-act_pol-cathode_conc_pol, 'b:')
    legend('Data','Fit','Polarization Components','Location','south')
    xlabel('Current Density (A cm^{-2})');
    ylabel('Voltage');
    ylim ([0 1.2])
    grid on
    hold off
end
```

Calculating total squared error of the fit

```
function err = polarization_model(params)
    if pO2 == 1
        model = ocv(1) - ohmic(current, params(1)) - activation(current,
params(2)) - anodic_conc(current, params(3));
    else
        model = ocv(1) - ohmic(current, params(1)) - activation(current,
params(2)) - anodic_conc(current, params(3)) - cathodic_conc(current,
params(4));
    end

    err = sum((exp_voltage - model).^2);
end
```

Polarization Components Functions

```
function dat = ohmic(x, R0)
%calculated ohmic polarization at the given current values
    dat = x.*R0;
end

function dat = activation(x, i0)
    %calculated activation polarization at given current values
    dat = ((R*T)/F)*log(0.5*((x./i0)+sqrt(((x./i0).^2)+4)));
end

function dat = cathodic_conc(x, ics)
    %calculated cathodic concentration polarization at given current values
    dat = -((R*T)/(4*F))*log(1-(x./ics));
end

function dat = anodic_conc(x, ias)
    %calculated anodic concentration polarziation at given current values
```

```
    dat = -((R*T)/(2*F))*log(1-(x./ias)) +
((R*T)/(2*F))*log(1+((pH2.*x)./(pH2O*ias)));
end
end
```

Published with MATLAB® R2015b

APPENDIX 3: Example Run of I-V Fitting Code

Before running, make sure the iv_fit functions are in the MATLAB path. Also, the data needs to have already been imported into the workspace. This can be done manually or using the file_import_script. Filenames are in the format of 'xTemp_pH2_pO2' (the x is used because file names cannot start with numbers in MATLAB). This example run curve fits IV measurements conducted under both pO2 and pH2 variation. The curve fitting procedure developed by Kyung Joong Yoon is used to fit curves during pO2 variation, and pH2-pH2O variation is used to evaluate anode performance at different fuel utilizations. Curve fitting can be done assuming a one electron or a two electron charge transfer reaction for the Butler-Volmer equation. The two electron reaction has less curvature than the one electron reaction. Sometimes, data fitting is much better depending on this choice.

Contents

Notes when using the iv_fit function:

The most common error is when the function tries to calculate the error at current densities greater than the Ias parameter. The error report is: "Error using barrier Objective function is undefined at initial point. Fmincon cannot continue." This is because at current densities higher than Ias, the anodic concentration polarization becomes a complex number. This error can be avoided by several means. Setting the lower bound for Ias at the highest current density of the data will always avoid this problem. If Ias is within the range of the current density for the given IV data, the fit ratio can be reduced, so that the error is not calculated at currents higher than Ias.

Evaluating the data

```
figure()

hold on
plot(x800C_97H2_100O2(:,1),x800C_97H2_100O2(:,2));
plot(x800C_97H2_21O2(:,1),x800C_97H2_21O2(:,2));
plot(x800C_97H2_10O2(:,1),x800C_97H2_10O2(:,2));
legend('97H_2 - 100_2','97H_2 - 21_2','97H_2 -
10_2','Location','northeast');
title('800\circC Cathode pO_2 Variation');
xlabel('Current Density (A cm^{-2})');
ylabel('Voltage');
hold off

% None of the curves reach the limiting current density in this data set.
```

```
% Thus, for Ias and Ics, lower bounds should always be the end of the
% curve. Upper bounds can be set to some reasonable values from previous
% experience or arbitrarily high. Guesses should be based on previous
% experience.

figure()
hold on
plot(x800C_97H2_21O2(:,1),x800C_97H2_21O2(:,2));
plot(x800C_87H2_21O2(:,1),x800C_87H2_21O2(:,2));
plot(x800C_75H2_21O2(:,1),x800C_75H2_21O2(:,2));
plot(x800C_62H2_21O2(:,1),x800C_62H2_21O2(:,2));
plot(x800C_50H2_21O2(:,1),x800C_50H2_21O2(:,2));
plot(x800C_37H2_21O2(:,1),x800C_37H2_21O2(:,2));
plot(x800C_25H2_21O2(:,1),x800C_25H2_21O2(:,2));
legend('97H_2 - 21O_2','87H_2 - 21O_2','75H_2 - 21O_2','62H_2 - 21O_2',...
    '50H_2 - 21O_2','37H_2 - 21O_2','25H_2 - 21O_2',...
    'Location','northeast');
title('800\circC Anode pH_2-pH_2O Variation');
xlabel('Current Density (A cm^{-2})');
ylabel('Voltage');
hold off
```

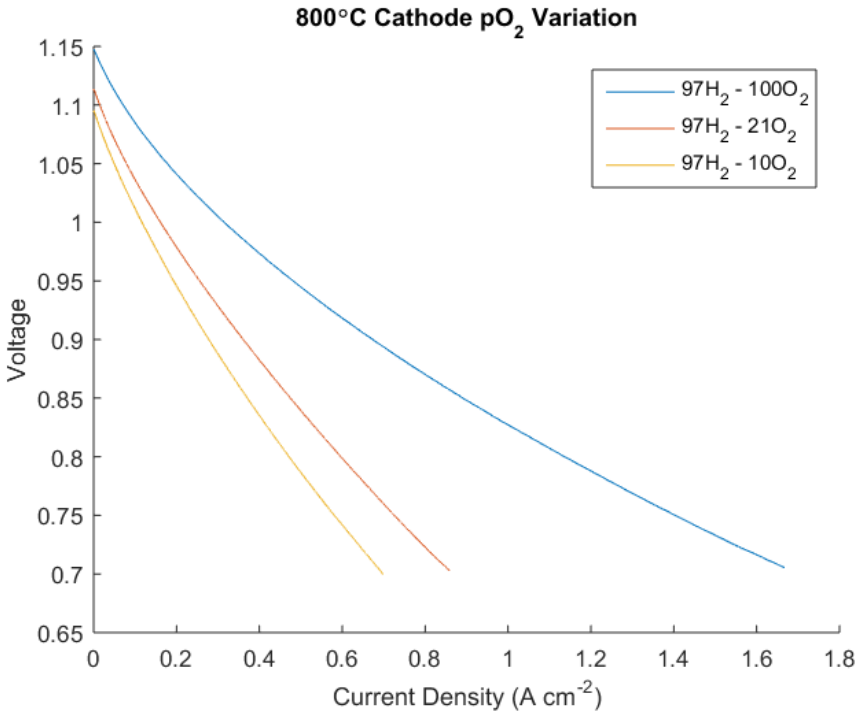
800°C Cathode pO2 Variation
97H2 - 100O2
97H2 - 21O2
97H2 - 10O2
Voltage
Current Density (A cm-2)
1.15
1.1
1.05
1
0.95
0.9
0.85
0.8
0.75
0.7
0.65
0
0.2
0.4
0.6
0.8
1
1.2
1.4
1.6
1.8

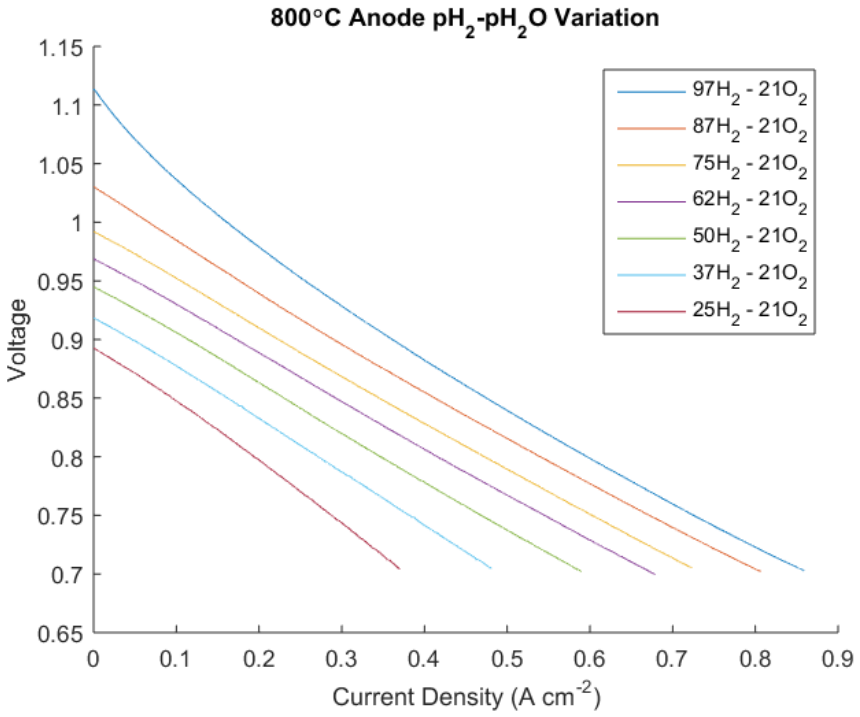
800°C Anode pH2-pH2O Variation
97H2 - 21O2
87H2 - 21O2
75H2 - 21O2
62H2 - 21O2
50H2 - 21O2
37H2 - 21O2
25H2 - 21O2
Voltage
Current Density (A cm-2)
1.15
1.1
1.05
1
0.95
0.9
0.85
0.8
0.75
0.7
0.65
0
0.1
0.2
0.3
0.4
0.5
0.6
0.7
0.8
0.9

Fitting data with pO2 variation

```
% 100O2 Fit
% The 100O2 fit is used to determine Ias and R_ohm, which then will be
% carried forward for fitting the rest of the data set.
% Set the experimental conditions (array [Temp(C), pH2, pO2])
x800C_97H2_100O2_cond = [800,0.97,1];
% Set the fit ratio (fits the given fraction of the data)
x800C_97H2_100O2_fr = 1;

% Set the guesses, lower bounds, and upper bounds:
% (array [R_ohm, i0, ias, ics])
% If the guess, lb, and ub are the same value, that parameter is set and
% cannot change.
x800C_97H2_100O2_guesses = [0.5,0.5,3.5,0];
x800C_97H2_100O2_lb = [0,0,x800C_97H2_100O2(end,1),0];
x800C_97H2_100O2_ub = [1,1,4,0];

% Run the fit and store the results:
% See the header of the iv_fit function for details on inputs and outputs
[x800C_97H2_100O2_fits, x800C_97H2_100O2_err] = ...
    iv_fit_n2(x800C_97H2_100O2,x800C_97H2_100O2_cond,x800C_97H2_100O2_fr,...
    x800C_97H2_100O2_guesses,x800C_97H2_100O2_lb,x800C_97H2_100O2_ub);
title('800\circC - 97H_2 - 100O_2');

% Save ias and R_ohm for later fits:
ias = x800C_97H2_100O2_fits(3);
R_ohm = x800C_97H2_100O2_fits(1);

% 21O2 Fit
% The 21O2 fit determines Ics for later fits at 21O2.
% Set the experimental conditions (array [Temp(C), pH2, pO2])
x800C_97H2_21O2_cond = [800,0.97,0.21];
% Set the fit ratio (fits the given fraction of the data)
x800C_97H2_21O2_fr = 1;

% Set the guesses, lower bounds, and upper bounds:
% (array [R_ohm, i0, ias, ics])
% The guess must be between the upper bound and lower bound. If the guess,
% lb, and ub are the same value, that parameter is set and cannot change.
x800C_97H2_21O2_guesses = [R_ohm,0.5,ias,3];
x800C_97H2_21O2_lb = [R_ohm,0,ias,x800C_97H2_21O2(end,1)];
x800C_97H2_21O2_ub = [R_ohm,1,ias,3];

% Run the fit and store the results:
% See the header of the iv_fit function for details on inputs and outputs
[x800C_97H2_21O2_fits, x800C_97H2_21O2_err] = ...
    iv_fit_n2(x800C_97H2_21O2,x800C_97H2_21O2_cond,x800C_97H2_21O2_fr,...
```

```
    x800C_97H2_21O2_guesses,x800C_97H2_21O2_lb,x800C_97H2_21O2_ub);
title('800\circC - 97H_2 - 21O_2');

% Save ics for later fits:
ics = x800C_97H2_21O2_fits(4);

% 10O2 Fit
% The 10O2 fit can be used to check the quality of the IV model. By using
% the ics value from 21O2, the ics value for 10O2 can be predicted and set.
% A Fickian diffusion model assumes that the ics should vary linearly with
% oxygen concentration. Thus the only free value is i0. A good fit here
% shows good predictive ability of the model.
% (A better way to do this would probably be to measure ics at some very
% low pO2 then use that to predict ics at 10% O2 and 21% O2)

% Set the experimental conditions (array [Temp(C), pH2, pO2])
x800C_97H2_10O2_cond = [800,0.97,0.10];
% Set the fit ratio (fits the given fraction of the data)
x800C_97H2_10O2_fr = 0.5;

% Set the guesses, lower bounds, and upper bounds:
% (array [R_ohm, i0, ias, ics])
% The guess must be between the upper bound and lower bound. If the guess,
% lb, and ub are the same value, that parameter is set and cannot change.
ics_10O2 = (0.1/0.9)*(0.79/0.21)*ics;
x800C_97H2_10O2_guesses = [R_ohm,0.5,ias,ics_10O2];
x800C_97H2_10O2_lb = [R_ohm,0,ias,ics_10O2];
x800C_97H2_10O2_ub = [R_ohm,1,ias,ics_10O2];

% Run the fit and store the results:
% See the header of the iv_fit function for details on inputs and outputs
[x800C_97H2_10O2_fits, x800C_97H2_10O2_err] = ...
    iv_fit_n2(x800C_97H2_10O2,x800C_97H2_10O2_cond,x800C_97H2_10O2_fr,...
    x800C_97H2_10O2_guesses,x800C_97H2_10O2_lb,x800C_97H2_10O2_ub);
title('800\circC - 97H_2 - 10O_2');
```

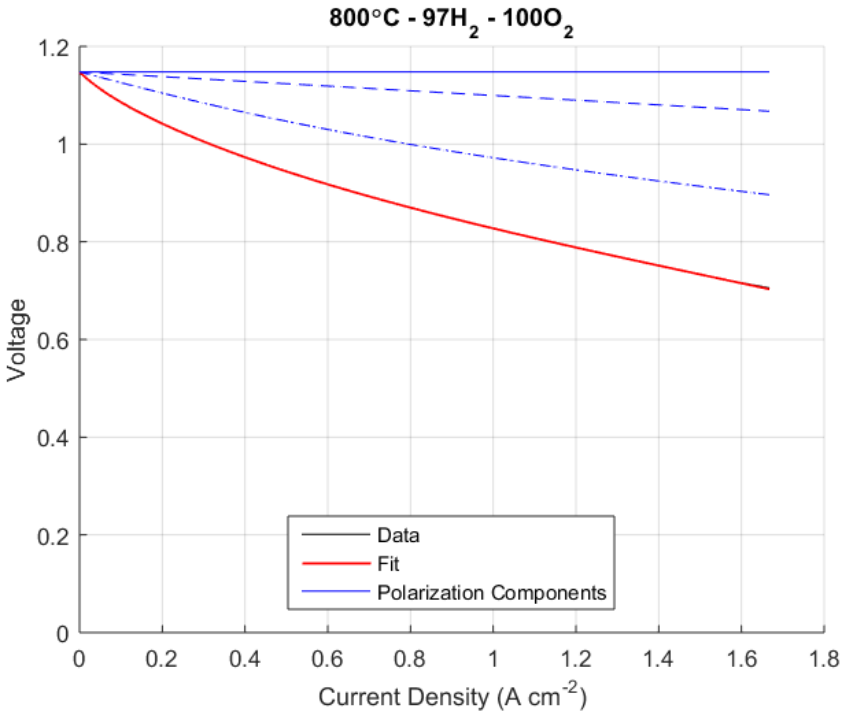
800°C - 97H2 - 100O2
Voltage
Current Density (A cm-2)
Data
Fit
Polarization Components
0
0.2
0.4
0.6
0.8
1
1.2
1.4
1.6
1.8

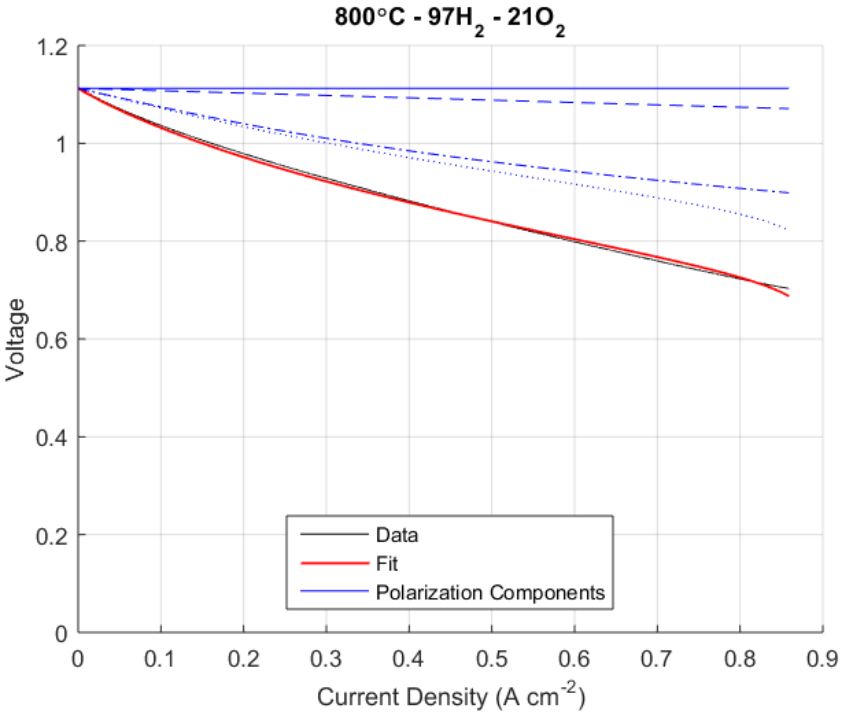
800°C - 97H2 - 21O2
Voltage
Current Density (A cm-2)
Data
Fit
Polarization Components
0
0.1
0.2
0.3
0.4
0.5
0.6
0.7
0.8
0.9
1
1.2

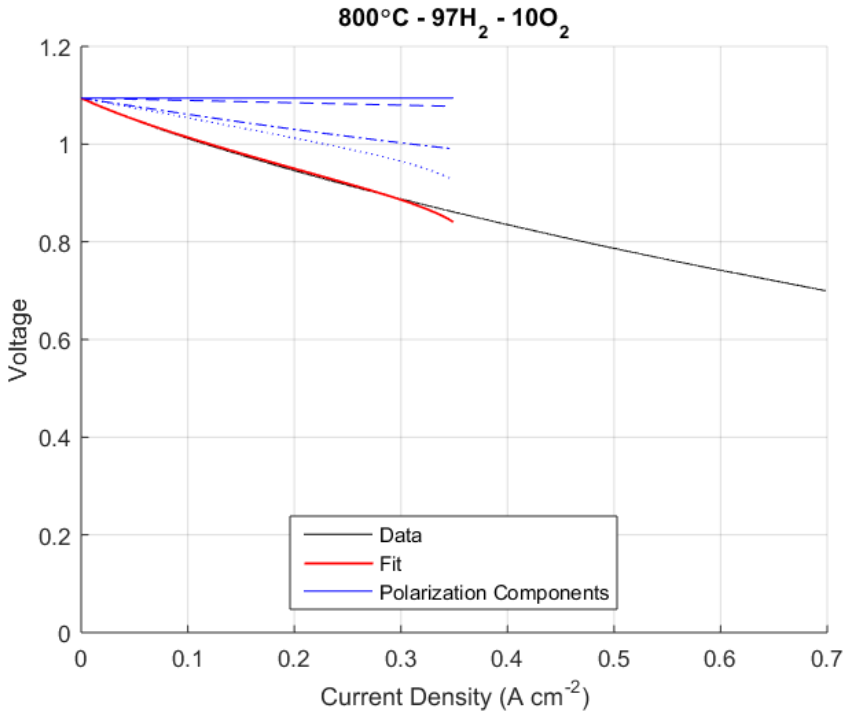
800°C - 97H2 - 10O2
1.2
1
0.8
0.6
0.4
0.2
0
Voltage
0
0.1
0.2
0.3
0.4
0.5
0.6
0.7
Current Density (A cm-2)
Data
Fit
Polarization Components

Evaluating IV fit with pO2 variation

The quality of IV fitting can be evaluated by comparing to EIS measurements. Both Rp and R_ohm can be compared if desired, but only Rp is compared here. Also, the change of i0 with pO2 is plotted.

```
Rp_fit(1:3) =
[x800C_97H2_100O2_fits(5),x800C_97H2_21O2_fits(5),x800C_97H2_10O2_fits(5)];

i0_fit(1:3) =
[x800C_97H2_100O2_fits(2),x800C_97H2_21O2_fits(2),x800C_97H2_10O2_fits(2)];

pO2 = [1,0.21,0.1];



figure()

hold on
scatter(pO2,Rp_measured(1:3), 'k', 'filled');
scatter(pO2,Rp_fit(1:3), 'k');
hold off
xlim([0 1]);
xlabel('Cathode pO_2, Balance N_2 (atm)');
ylabel('R_{Polarization} (\Omega cm^2)');
legend({'EIS Measured R_{Polarizaion}','Curve Fit R_{Polarization}'});
title('Comparing Measured and Curve Fit Polarization Resistance, pO_2
Variation');

figure()
scatter(pO2,i0_fit(1:3), 'k');
xlim([0 1]);
xlabel('Cathode pO_2, Balance N_2 (atm)');
ylabel('Exchange Current Density (A cm^{-2})');
title('Exchange Current Density versus Cathode pO_2');
```

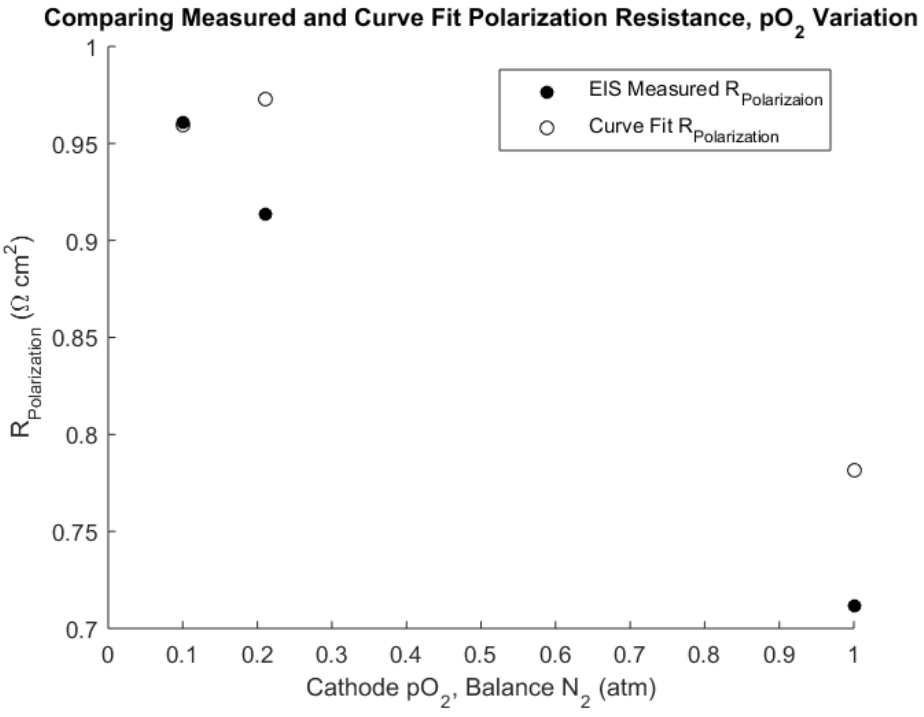
Comparing Measured and Curve Fit Polarization Resistance, pO2 Variation
EIS Measured RPolarizaion
Curve Fit RPolarization
RPolarization (Ω cm2)
Cathode pO2, Balance N2 (atm)
1
0.95
0.9
0.85
0.8
0.75
0.7
0
0.1
0.2
0.3
0.4
0.5
0.6
0.7
0.8
0.9
1

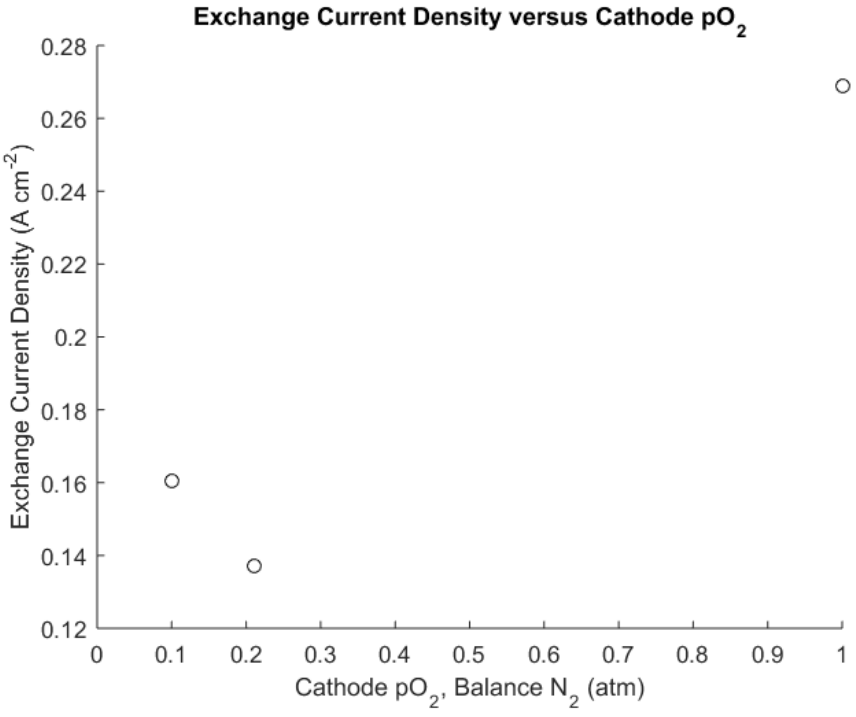
Exchange Current Density versus Cathode pO2
Exchange Current Density (A cm-2)
Cathode pO2, Balance N2 (atm)
0.28
0.26
0.24
0.22
0.2
0.18
0.16
0.14
0.12
0
0.1
0.2
0.3
0.4
0.5
0.6
0.7
0.8
0.9
1

Fitting H2-H2O variation

Curve fits with H2-H2O variation are used to determine the variation of the activation polarization with changing anode conditions. Similar to the 10O2 fit, the ias can be estimated from the H2-H2O concentration assuming Fickian diffusion. This leaves i0 as the only fitting parameter.

```
% 87H2 Fit
% Set the experimental conditions (array [Temp(C), pH2, pO2])
x800C_87H2_21O2_cond = [800,0.87,0.21];
% Set the fit ratio (fits the given fraction of the data)
x800C_87H2_21O2_fr = 1;

% Set the guesses, lower bounds, and upper bounds:
% (array [R_ohm, i0, ias, ics])
% The guess must be between the upper bound and lower bound. If the guess,
% lb, and ub are the same value, that parameter is set and cannot change.
ias_87H2 = 0.87*(ias/0.97);
x800C_87H2_21O2_guesses = [R_ohm,0.5,ias_87H2,ics];
x800C_87H2_21O2_lb = [R_ohm,0,ias_87H2,ics];
x800C_87H2_21O2_ub = [R_ohm,1,ias_87H2,ics];

% Run the fit and store the results:
% See the header of the iv_fit function for details on inputs and outputs
[x800C_87H2_21O2_fits, x800C_87H2_21O2_err] = ...
    iv_fit_n2(x800C_87H2_21O2,x800C_87H2_21O2_cond,x800C_87H2_21O2_fr,...
    x800C_87H2_21O2_guesses,x800C_87H2_21O2_lb,x800C_87H2_21O2_ub);
title('800\circC - 87H_2 - 21O_2');

% 75H2 Fit
% Set the experimental conditions (array [Temp(C), pH2, pO2])
x800C_75H2_21O2_cond = [800,0.75,0.21];
% Set the fit ratio (fits the given fraction of the data)
x800C_75H2_21O2_fr = 1;

% Set the guesses, lower bounds, and upper bounds:
% (array [R_ohm, i0, ias, ics])
% The guess must be between the upper bound and lower bound. If the guess,
% lb, and ub are the same value, that parameter is set and cannot change.
ias_75H2 = 0.75*(ias/0.97);
x800C_75H2_21O2_guesses = [R_ohm,0.5,ias_75H2,ics];
x800C_75H2_21O2_lb = [R_ohm,0,ias_75H2,ics];
x800C_75H2_21O2_ub = [R_ohm,1,ias_75H2,ics];

% Run the fit and store the results:
% See the header of the iv_fit function for details on inputs and outputs
[x800C_75H2_21O2_fits, x800C_75H2_21O2_err] = ...
    iv_fit_n2(x800C_75H2_21O2,x800C_75H2_21O2_cond,x800C_75H2_21O2_fr,...
```

```
    x800C_75H2_21O2_guesses,x800C_75H2_21O2_lb,x800C_75H2_21O2_ub);
title('800\circC - 75H_2 - 21O_2');

% 62H2 Fit
% Set the experimental conditions (array [Temp(C), pH2, pO2])
x800C_62H2_21O2_cond = [800,0.62,0.21];
% Set the fit ratio (fits the given fraction of the data)
x800C_62H2_21O2_fr = 1;

% Set the guesses, lower bounds, and upper bounds:
% (array [R_ohm, i0, ias, ics])
% The guess must be between the upper bound and lower bound. If the guess,
% lb, and ub are the same value, that parameter is set and cannot change.
ias_62H2 = 0.62*(ias/0.97);
x800C_62H2_21O2_guesses = [R_ohm,0.5,ias_62H2,ics];
x800C_62H2_21O2_lb = [R_ohm,0,ias_62H2,ics];
x800C_62H2_21O2_ub = [R_ohm,1,ias_62H2,ics];

% Run the fit and store the results:
% See the header of the iv_fit function for details on inputs and outputs
[x800C_62H2_21O2_fits, x800C_62H2_21O2_err] = ...
    iv_fit_n2(x800C_62H2_21O2,x800C_62H2_21O2_cond,x800C_62H2_21O2_fr,...
    x800C_62H2_21O2_guesses,x800C_62H2_21O2_lb,x800C_62H2_21O2_ub);
title('800\circC - 62H_2 - 21O_2');

% 50H2 Fit
% Set the experimental conditions (array [Temp(C), pH2, pO2])
x800C_50H2_21O2_cond = [800,0.50,0.21];
% Set the fit ratio (fits the given fraction of the data)
x800C_50H2_21O2_fr = 1;

% Set the guesses, lower bounds, and upper bounds:
% (array [R_ohm, i0, ias, ics])
% The guess must be between the upper bound and lower bound. If the guess,
% lb, and ub are the same value, that parameter is set and cannot change.
ias_50H2 = 0.50*(ias/0.97);
x800C_50H2_21O2_guesses = [R_ohm,0.5,ias_50H2,ics];
x800C_50H2_21O2_lb = [R_ohm,0,ias_50H2,ics];
x800C_50H2_21O2_ub = [R_ohm,1,ias_50H2,ics];

% Run the fit and store the results:
% See the header of the iv_fit function for details on inputs and outputs
[x800C_50H2_21O2_fits, x800C_50H2_21O2_err] = ...
    iv_fit_n2(x800C_50H2_21O2,x800C_50H2_21O2_cond,x800C_50H2_21O2_fr,...
    x800C_50H2_21O2_guesses,x800C_50H2_21O2_lb,x800C_50H2_21O2_ub);
title('800\circC - 50H_2 - 21O_2');
```

```
% 37H2 Fit
% Set the experimental conditions (array [Temp(C), pH2, pO2])
x800C_37H2_21O2_cond = [800,0.37,0.21];
% Set the fit ratio (fits the given fraction of the data)
x800C_37H2_21O2_fr = 1;

% Set the guesses, lower bounds, and upper bounds:
% (array [R_ohm, i0, ias, ics])
% The guess must be between the upper bound and lower bound. If the guess,
% lb, and ub are the same value, that parameter is set and cannot change.
ias_37H2 = 0.37*(ias/0.97);
x800C_37H2_21O2_guesses = [R_ohm,0.5,ias_37H2,ics];
x800C_37H2_21O2_lb = [R_ohm,0,ias_37H2,ics];
x800C_37H2_21O2_ub = [R_ohm,1,ias_37H2,ics];

% Run the fit and store the results:
% See the header of the iv_fit function for details on inputs and outputs
[x800C_37H2_21O2_fits, x800C_37H2_21O2_err] = ...
    iv_fit_n2(x800C_37H2_21O2,x800C_37H2_21O2_cond,x800C_37H2_21O2_fr,...
    x800C_37H2_21O2_guesses,x800C_37H2_21O2_lb,x800C_37H2_21O2_ub);
title('800\circC - 37H_2 - 21O_2');

% 25H2 Fit
% Set the experimental conditions (array [Temp(C), pH2, pO2])
x800C_25H2_21O2_cond = [800,0.25,0.21];
% Set the fit ratio (fits the given fraction of the data)
x800C_25H2_21O2_fr = 1;

% Set the guesses, lower bounds, and upper bounds:
% (array [R_ohm, i0, ias, ics])
% The guess must be between the upper bound and lower bound. If the guess,
% lb, and ub are the same value, that parameter is set and cannot change.
ias_25H2 = 0.25*(ias/0.97);
x800C_25H2_21O2_guesses = [R_ohm,0.5,ias_25H2,ics];
x800C_25H2_21O2_lb = [R_ohm,0,ias_25H2,ics];
x800C_25H2_21O2_ub = [R_ohm,1,ias_25H2,ics];

% Run the fit and store the results:
% See the header of the iv_fit function for details on inputs and outputs
[x800C_25H2_21O2_fits, x800C_25H2_21O2_err] = ...
    iv_fit_n2(x800C_25H2_21O2,x800C_25H2_21O2_cond,x800C_25H2_21O2_fr,...
    x800C_25H2_21O2_guesses,x800C_25H2_21O2_lb,x800C_25H2_21O2_ub);
title('800\circC - 25H_2 - 21O_2');
```

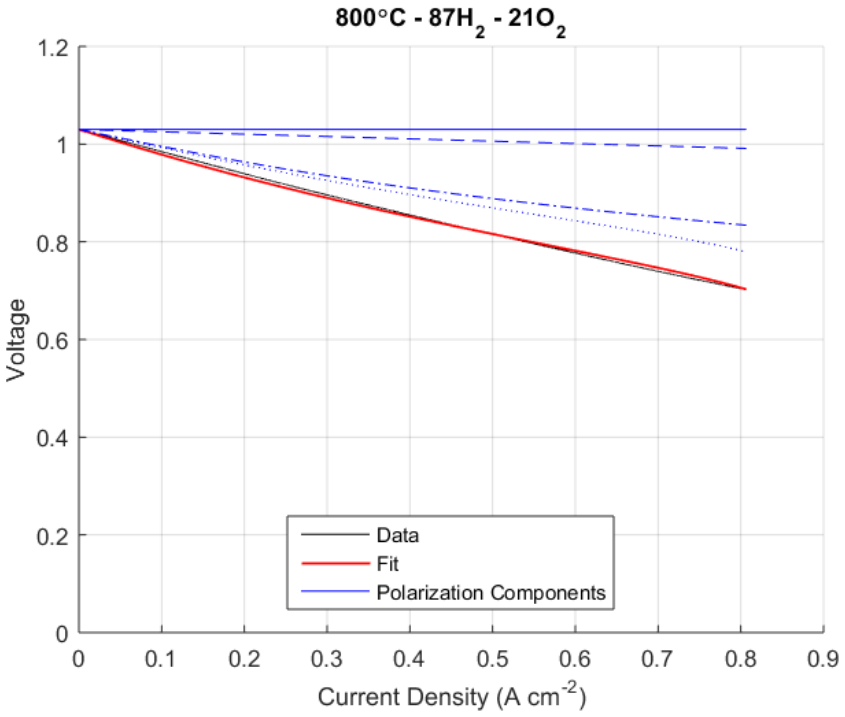
800°C - 87H2 - 21O2
Voltage
Current Density (A cm-2)
Data
Fit
Polarization Components
0
0.2
0.4
0.6
0.8
1
1.2
0.1
0.3
0.5
0.7
0.9

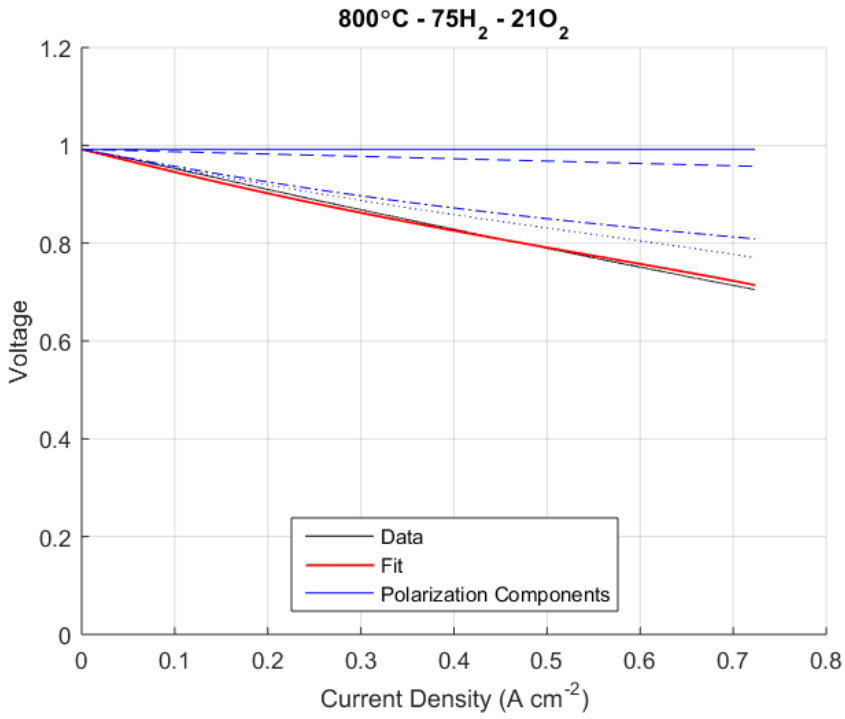
800°C - 75H2 - 21O2
Voltage
Current Density (A cm-2)
Data
Fit
Polarization Components
0
0.2
0.4
0.6
0.8
1
1.2
0.1
0.3
0.5
0.7

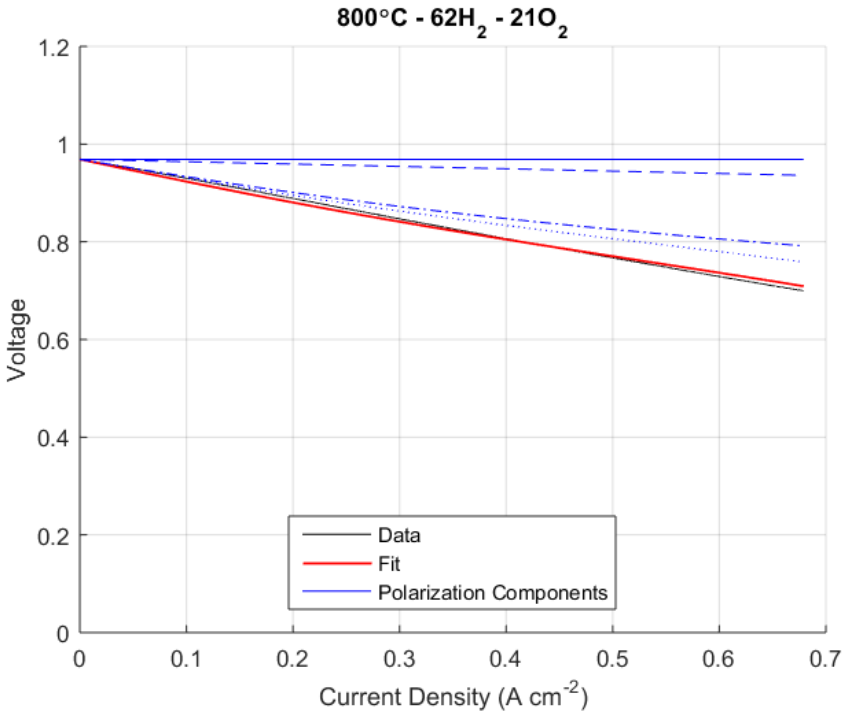
800°C - 62H2 - 21O2
Voltage
Current Density (A cm-2)
Data
Fit
Polarization Components
0
0.2
0.4
0.6
0.8
1
1.2
0.1
0.3
0.5
0.7

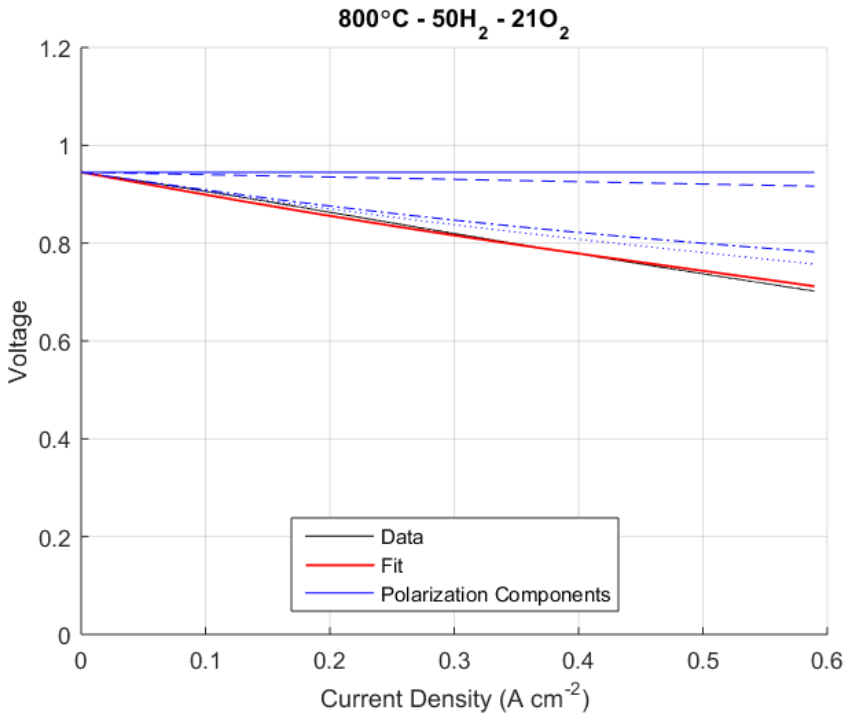
800°C - 50H2 - 21O2
Voltage
Current Density (A cm-2)
Data
Fit
Polarization Components
0
0.2
0.4
0.6
0.8
1
1.2
0.1
0.3
0.5

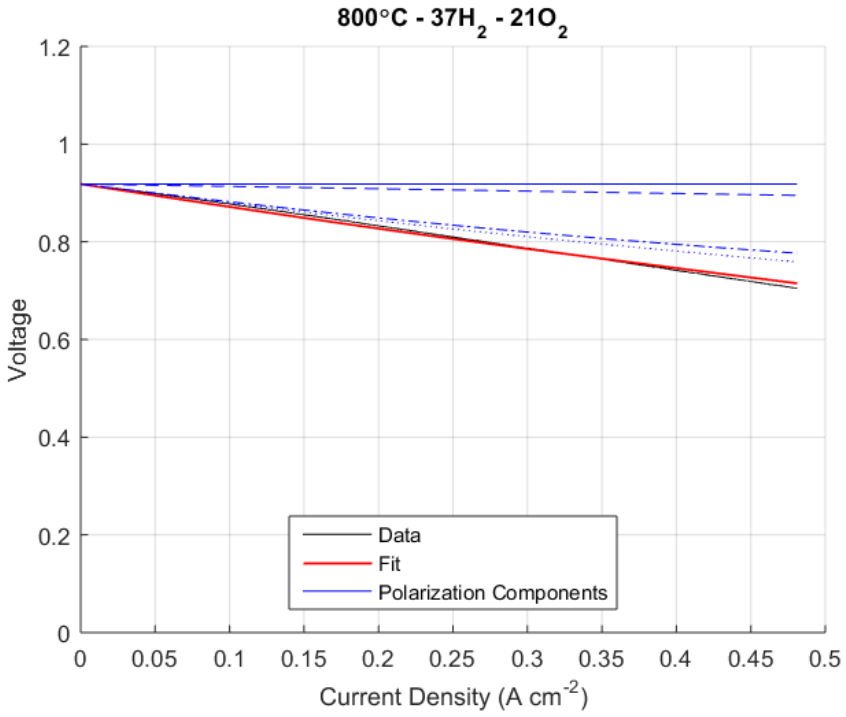
800°C - 37H2 - 21O2
Voltage
Current Density (A cm-2)
Data
Fit
Polarization Components
0
0.2
0.4
0.6
0.8
1
1.2
0.05
0.1
0.15
0.2
0.25
0.3
0.35
0.4
0.45
0.5

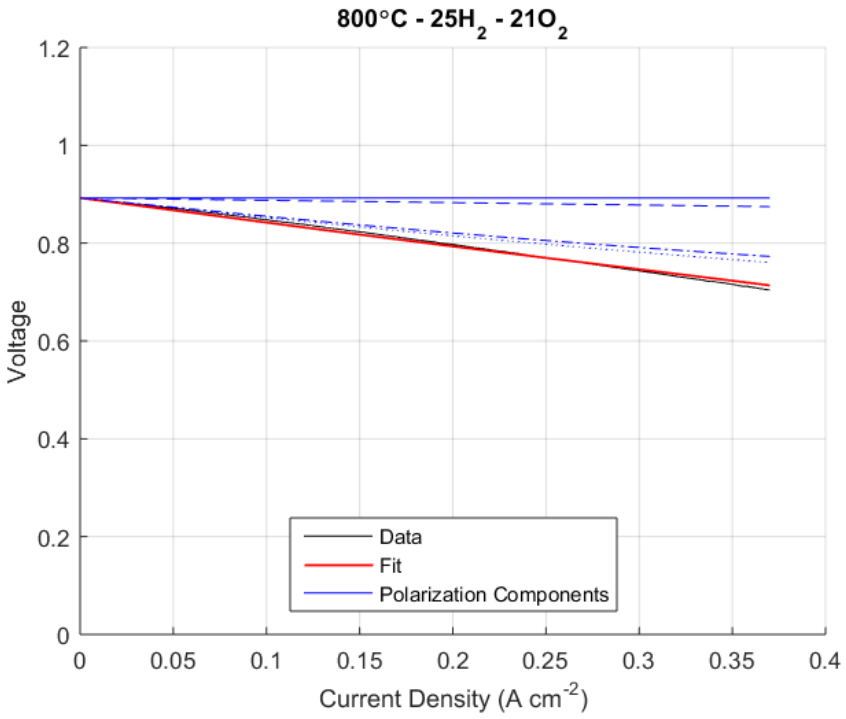
800°C - 25H2 - 21O2
Voltage
Current Density (A cm-2)
Data
Fit
Polarization Components
0
0.2
0.4
0.6
0.8
1
1.2
0.05
0.1
0.15
0.2
0.25
0.3
0.35
0.4

Evaluating IV fit with pH2 variation

The quality of IV fitting can be evaluated by comparing to EIS measurements. Both Rp and R_ohm can be compared if desired, but only Rp is compared here. Also, the change of i0 with pH2 is plotted.

```
Rp_fit(4:10) = [x800C_97H2_21O2_fits(5),x800C_87H2_21O2_fits(5),...
    x800C_75H2_21O2_fits(5),x800C_62H2_21O2_fits(5),
x800C_50H2_21O2_fits(5),...
    x800C_37H2_21O2_fits(5),x800C_25H2_21O2_fits(5)];
i0_fit(4:10) = [x800C_97H2_21O2_fits(2),x800C_87H2_21O2_fits(2),...
    x800C_75H2_21O2_fits(2),x800C_62H2_21O2_fits(2),
x800C_50H2_21O2_fits(2),...
    x800C_37H2_21O2_fits(2),x800C_25H2_21O2_fits(2)];
pH2 = [0.97,0.87,0.75,0.62,0.50,0.37,0.25];

figure()
hold on
scatter(pH2,Rp_measured(4:10), 'k', 'filled');
scatter(pH2,Rp_fit(4:10), 'k');
hold off
xlim([0 1]);
xlabel('Anode pH_2, Balance H_2O (atm)');
ylabel('R_{Polarization} (\Omega cm^2)');
legend({'EIS Measured R_{Polarizaion}','Curve Fit
R_{Polarization}'},'Location','northwest');
title('Comparing Measured and Curve Fit Polarization Resistance, pH_2-pH_2O
Variation');

figure()
scatter(pH2,i0_fit(4:10), 'k');
xlim([0 1]);
xlabel('Anode pH_2, Balance H_2O (atm)');
ylabel('Exchange Current Density (A cm^{-2})');
title('Exchange Current Density versus Anode pH_2');
```

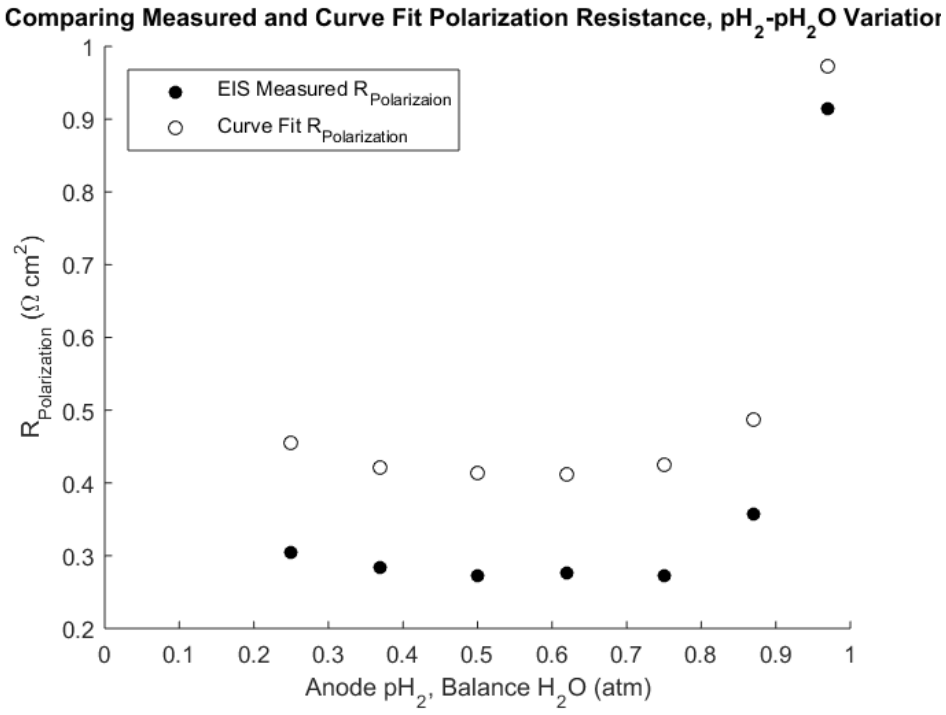
Comparing Measured and Curve Fit Polarization Resistance, pH2-pH2O Variation
EIS Measured RPolarizaion
Curve Fit RPolarization
RPolarization (Ω cm2)
Anode pH2, Balance H2O (atm)

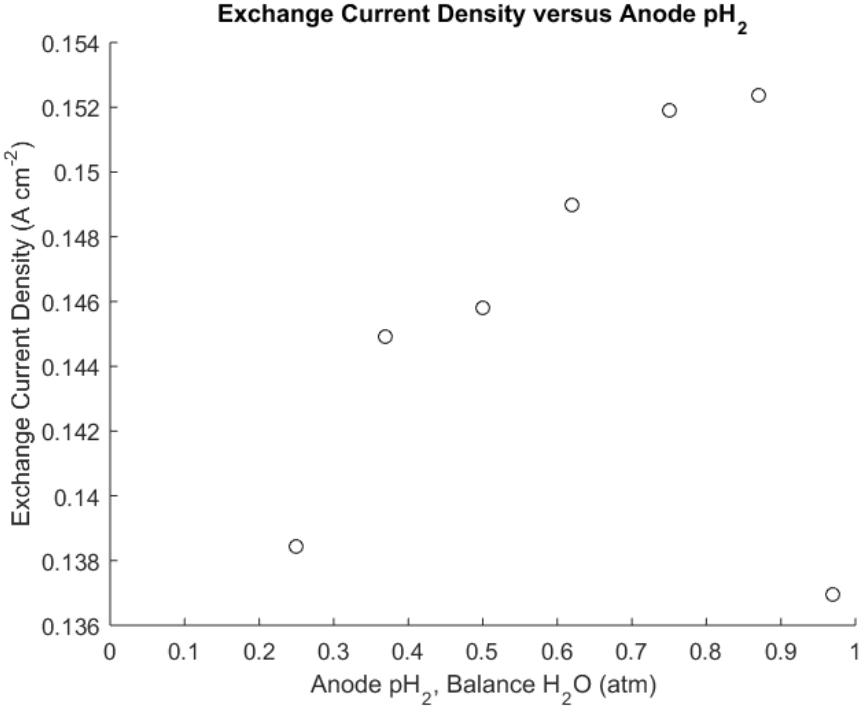
Exchange Current Density versus Anode pH2
Exchange Current Density (A cm-2)
Anode pH2, Balance H2O (atm)

Format data for export

```
% Place all the data into a table for export.
 parameters = {'R0';'i0';'ias';'ics';'Rp'};
    fittedParams = [parameters,...
        mat2cell(x800C_97H2_100O2_fits',[1,1,1,1,1],1),...
        mat2cell(x800C_97H2_21O2_fits',[1,1,1,1,1],1),...
        mat2cell(x800C_97H2_10O2_fits',[1,1,1,1,1],1),...
        mat2cell(x800C_87H2_21O2_fits',[1,1,1,1,1],1),...
        mat2cell(x800C_75H2_21O2_fits',[1,1,1,1,1],1),...
        mat2cell(x800C_62H2_21O2_fits',[1,1,1,1,1],1),...
        mat2cell(x800C_50H2_21O2_fits',[1,1,1,1,1],1),...
        mat2cell(x800C_37H2_21O2_fits',[1,1,1,1,1],1),...
        mat2cell(x800C_25H2_21O2_fits',[1,1,1,1,1],1)];
    fittedParamsTable = cell2table(fittedParams,'VariableNames',...
        {'Parameter','x800C_97H2_100O2','x800C_97H2_21O2','x800C_97H2_10O2',...
        'x800C_87H2_21O2','x800C_75H2_21O2','x800C_62H2_21O2',...
        'x800C_50H2_21O2','x800C_37H2_21O2','x800C_25H2_21O2'});

% Change the current folder for saving the results table
current_dir = cd;
cd 'G:\Dropbox\Anode Modification Research\Matlab Data Fitting\IV fitting';

% Export the results table
writetable(fittedParamsTable, 'IV fitting 800C n=2.xls');

% Return the current folder to the previous path
cd(current_dir);
clear current_dir;
```

Published with MATLAB® R2015b

APPENDIX 4: MATLAB EIS Fitting Code

Special thanks to Dr. Raymond Gasper, who developed the basic structure of this fitting code, enabling the use of simple data management and easy modification of the equivalent circuit model.

Contents


```
function [fitted_params, final_error] = fit_eis_dat_RRQRQGeFLW(exp_dat,
data_title, params, ub, lb)
%Ray Gasper, 2018, UMass Amherst
%Edit 11/19/2018 by Paul Gasper: Added bode plot
%Edit 11/20/2018 by Paul Gasper: Changed plotting to plot over a much
% larger frequency space than the data, changed automatic upper bounding to
% work for measurements with total resistance greater than 1.
%Edit 12/7/2018 by Paul Gasper: Fixed equivalent circuit model elements
%using frequency instead of angular frequency in calculations
%Edit 12/19/2018 by Paul Gasper: Changed plotting to plot bode and nyquist
%plots on the same figure.

%Description:
%Fits an EIS curve using a predefined equivalent circuit model that is
%typical for solid-oxide fuel cells.
%Produces a Nyquist plot and Bode plotwith the experimental data,
%total ECM fit, and ECM %split up element-wise in a way that allows
%intuitive understanding.

%ECM structure: R-RQ1-RQ2-GE-FLW

%R: Resistor; parameters: Resistance
%RQ: RQ element; parameters: Yq, nq, Resistance
%GE: Gerischer element; parameters: Tc, Resistance
%FLW: Generalized Finite-Length Warburg element; parameters: Tw, Nw, Resistance

%It is advised to use a relatively good initial guess or reasonable
%constraints in order to ensure the realism of the fit. There are often
%many local minima within a parameter space. Make sure that fit results are
%physically realistic, and that fitted quantities are not simply hitting
%the upper or lower bounds.
```

```
%exp_dat should be a string containing the address of a csv with EIS data
%in it. Fitting accuracy will depend on sampling density
% EIS data structure:
% Frequencies, Real, Imaginary
%   dat      , dat , dat
%   dat      , dat , dat
%   dat      , dat , dat
%   dat      , dat , dat
%   dat      , dat , dat

%initial params guess, upper bound, and lower bound are all 1x12 vectors
%corresponding to the paramater list:
%  1      2       3      4     5       6       7       8     9      10       11
12
%R1(R),RQ1(Yq),RQ1(nq),RQ1(R),RQ2(Yq),RQ2(nq),RQ2(R),GE(Tc),GE(R),FLW(Tw),FLW(n
w),FLW(R)

%data_title is a character string used for naming plots
```

Setup

```
%read the experimental data
dat = csvread(exp_dat,1,0);
exp_dat = clean_eis(dat);
global Freq Omega exp_i exp_r
Freq = exp_dat(:,1); Omega = Freq.*(2*pi);
exp_r = exp_dat(:,2); exp_i = exp_dat(:,3);

%initialize fmincon inputs
if isempty(params)
    %if there's no initial guess use a random one
    %for the SOFCS initial parameters, lb of 0 is fine
    %for upper bounds, resistances can be bounded by total resistance
    %and other parameters can be bounded with physical limits (nq cannot be
    %greater than 1, Yq will never reach 1 Farad in electrochemical
    %reactions, Gerischer time constant will not be larger than 1, and the
    %maximum for nw is 0.5 at the one-dimensional diffusion limit)
    params = rand(1,12);
end
if isempty(lb)
    lb = [0 0 0 0 0 0 0 0 0 0 0 0];
end
if isempty(ub)
    Rtot = max(exp_r);
    ub = [Rtot 1 1 Rtot 1 1 Rtot 1 Rtot 1 0.5 Rtot];
end
A = []; Aeq = [];
```

```
b = []; beq = [];
```

Fit the model

```
[fitted_params, final_error] = ...
    fmincon(@ecm_min_fit, params, A, b, Aeq, beq, lb, ub);
```

Plot

```
freq_long = logspace(-2,6,1001); %generate a wide frequency space for plotting
the model
omega_long = freq_long.*(2*pi);
R_shift = R_element(omega_long,[],1); %unit horizontal shift element for fancy
plotting

% to modify the ECM structure, please modify in ecm_min_fit first then copy
here and change the name of vars
% the first bit ensures consistency and the second bit avoids implicit global
scoping
R = R_element(omega_long,[], fitted_params(1));
RQ1 = RQ_element(omega_long, fitted_params(2:3), fitted_params(4)); % Yq, nq
RQ2 = RQ_element(omega_long, fitted_params(5:6), fitted_params(7)); % Yq, nq
GE = GE_element(omega_long, fitted_params(8), fitted_params(9)); % Tc
FLW = FLW_element(omega_long, fitted_params(10:11), fitted_params(12));% Tw, nw

Rr = R(:,2);          Ri = R(:,3);
RQr1 = RQ1(:,2);      RQi1 = RQ1(:,3);
RQr2 = RQ2(:,2);      RQi2 = RQ2(:,3);
GEr = GE(:,2);        GEi = GE(:,3);
FLWr = FLW(:,2);      FLWi = FLW(:,3);
Sr = R_shift(:,2);    Si = R_shift(:,3);

% ECM is just the five elements in series
sim_r = Rr + RQr1 + RQr2 + GEr + FLWr;
sim_i = Ri + RQi1 + RQi2 + GEi + FLWi;

% Nyquist plot
scrsz = get(groot,'ScreenSize');
figure('OuterPosition',[10 scrsz(4)*0.2 scrsz(3)*0.5 scrsz(4)*0.8]);
nyquist = subplot(2,1,1);
hold on
plot(nyquist,exp_r,exp_i,'ok','LineWidth',1)
plot(nyquist,sim_r,sim_i,'b-','LineWidth',1)
plot(nyquist,RQr1+Sr*(fitted_params(1)), RQi1,'-r')
plot(nyquist,RQr2+Sr*(fitted_params(1)+fitted_params(4)), RQi2,'-g')
plot(nyquist,GEr+Sr*(fitted_params(1)+fitted_params(4)+fitted_params(7)),
GEi,'-m')
```

```
plot(nyquist,FLWr+Sr*(fitted_params(1)+fitted_params(4)+fitted_params(7)+fitted
_params(9)), FLWi,'-c')
xs = get(nyquist, 'XLim');
nyquist.YLim = [-xs(2)/2,0]; % makes y-axis the same length as x-axis
nyquist.YDir = 'reverse';
nyquist.XGrid = 'on';
nyquist.YGrid = 'on';
nyquist.XLabel.String = 'Z_{Real}(\Omega cm^2)';
nyquist.YLabel.String = 'Z_{Imaginary}(\Omega cm^2)';
title(data_title);
axis manual
nyquist.DataAspectRatio = [1 1 1];
hold off
legend('Exp. Data','ECM fit','RQ1','RQ2','GE','FLW','Location','eastoutside')

% Bode plot imaginary
bode = subplot(2,1,2);
plot(bode,Freq,exp_i,'ok','LineWidth',1)
bode.XScale = 'log';
bode.XGrid = 'on';
bode.XTick = [0.01,0.1,1,10,100,1000,10000,100000,1000000];
bode.XMinorGrid = 'off';
bode.YDir = 'reverse';
bode.YGrid = 'on';
bode.XLabel.String = 'Frequency (Hz)';
bode.YLabel.String = 'Z_{Imaginary}(\Omega cm^2)';
bode.PlotBoxAspectRatio = [1 0.5 1];
hold on
plot(bode,freq_long, sim_i, 'b-','LineWidth',1)
plot(bode,freq_long,RQi1,'-r')
plot(bode,freq_long,RQi2,'-g')
plot(bode,freq_long,GEi,'-m')
plot(bode,freq_long,FLWi,'-c')
hold off
legend('Exp. Data','ECM fit','RQ1','RQ2','GE','FLW','Location','eastoutside')
```

Function to exclude positive imaginary components

```
function dat = clean_eis(exp_dat)
 % Cleans EIS data of Zi > 0 elements
 % Zi > 0 only occurs due to inductance, which should be removed from data
 % before fitting anyways. They are removed here to ensure that no fitting
 % error occurs if there are stray data points remaining.
 omega = exp_dat(:,1);
 Zr = exp_dat(:,2);
 Zi = exp_dat(:,3);

 bad = any(Zi>0,2);
```

```
 if sum(bad) > length(Zi)/2
    Zi = Zi.*-1;
    bad = any(Zi>0,2);
 end

 c_omega = omega(~bad,:);
 c_Zr = Zr(~bad,:);
 c_Zi = Zi(~bad,:);

 dat = [c_omega, c_Zr, c_Zi];
end
```

Function to calculate total squared error of a particular ECM parameter set

```
function err = ecm_min_fit(params)
% ecm fit function with defined circuit for implementation in matlab's
% fminsearch funtion

%If you want to modify the ECM structure, make your changes here then copy to
the plotting section & then
%rename vars outside this to avoid causing implicit global variable scoping
Rs = R_element(Omega,[], params(1));
RQ1s = RQ_element(Omega, params(2:3), params(4)); % Yq, nq
RQ2s = RQ_element(Omega, params(5:6), params(7)); % Yq, nq
GEs = GE_element(Omega, params(8), params(9)); % Tc
FLWs = FLW_element(Omega, params(10:11), params(12));% Tw, nw

fit_r = Rs(:,2) + RQ1s(:,2) + RQ2s(:,2) + GEs(:,2) + FLWs(:,2);
fit_i = Rs(:,3) + RQ1s(:,3) + RQ2s(:,3) + GEs(:,3) + FLWs(:,3);
% fit = [Freq, fit_r, fit_i];

err_r = sum((exp_r - fit_r).^2);
err_i = sum((exp_i - fit_i).^2);

err = err_r + err_i;
end
```

Circuit Element functions

```
function dat = R_element(omega, params, R)
 % from a given set of frequencies generates the Zr and Zi for a resistor

 Z = R;

 dat(:,1) = omega;
 dat(:,2) = real(Z);
 dat(:,3) = imag(Z);
```

```
end

function dat = RQ_element(omega, params, R)
 % from a given set of frequencies generates the Zr and Zi for a RQ
 % element
 Y_q = params(1);
 n_q = params(2);

 Q = 1 ./ (Y_q .* (omega.*1i).^n_q);
 Z = R ./ ( 1 + R.*(Q.^-1) );

 dat(:,1) = omega;
 dat(:,2) = real(Z);
 dat(:,3) = imag(Z);
end

function dat = GE_element(omega, params, R)
 % from a given set of frequencies generates the Zr and Zi for a
 % Gerischer Element
 t_c = params(1);

 Z = R ./ sqrt(1+omega.*t_c.*1i);

 dat(:,1) = omega;
 dat(:,2) = real(Z);
 dat(:,3) = imag(Z);
end

function dat = FLW_element(omega, params, R)
 % from a given set of frequencies generates the Zr and Zi for a
 % Finite-Length Warburg Element
 T_w = params(1);
 n_w = params(2);

 Z = R .* ( tanh( (omega.*T_w.*1i).^n_w ) )./...
              ( (omega.*T_w.*1i ).^n_w ) ;

 dat(:,1) = omega;
 dat(:,2) = real(Z);
 dat(:,3) = imag(Z);
end
end
```

Published with MATLAB® R2015b

APPENDIX 5: Example Run of EIS Fitting

Contents


```
%Example script for how to use the EIS equivalent circuit model fitting
function
%Ray Gasper, 2018, UMass Amherst

%Notice that even with 'good' or 'bad' guesses, there are enough degrees of
%freedom within the equivalen cirucit model that a fit with low error can
%be produced. Physical relevance of the EIS fitting result requires a large
%set of experimental conditions and validation of the fitted results by
%comparing results to literature and comparing with I-V data (I-V can be
%simulated using resistances from the EIS fit and compared to the
%experimental I-V).
clear;clc;
```

simplest possible run- random initial guess, default constraints

```
%If you run this multiple times you'll notice the ECM can change
%significantly, this means there are many local minima in the
%error:parameter space- only if you're lucky will this fit be realistic
%sometimes it won't converge at all, often (not always) meaning the random
%initial guess is in a particularly bad region of parameter space, and the fit
is bad
[fit_1, err_1] = fit_eis_dat('exp_data_fine.csv','Random Initial Guess &
Default UB, LB',[],[],[]);
```

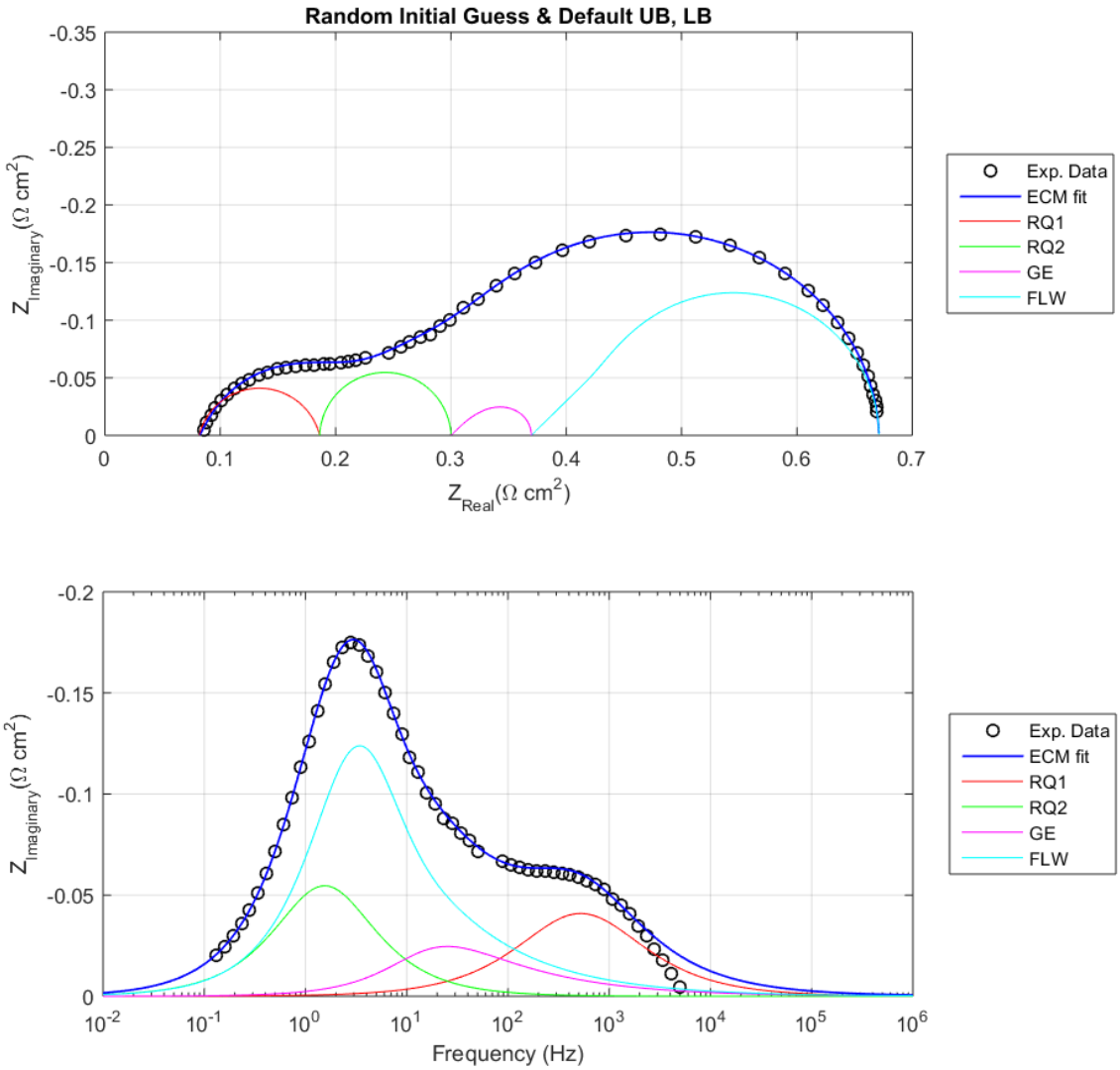

with good initial guess, default UB and LB

```
%this is using a pretty good initial guess.
%Notice with re-running there's some, but little change- we're close to a good
%minima, with these values listed corresponding to realistic ones
guess=[0.01,0.01,0.75,0.15,0.25,0.75,0.05,0.01,0.05,0.05,0.5,0.3];
[fit_2, err_2] = fit_eis_dat('exp_data_fine.csv','Good Initial Guess & Default
UB, LB',guess,[],[]);
```

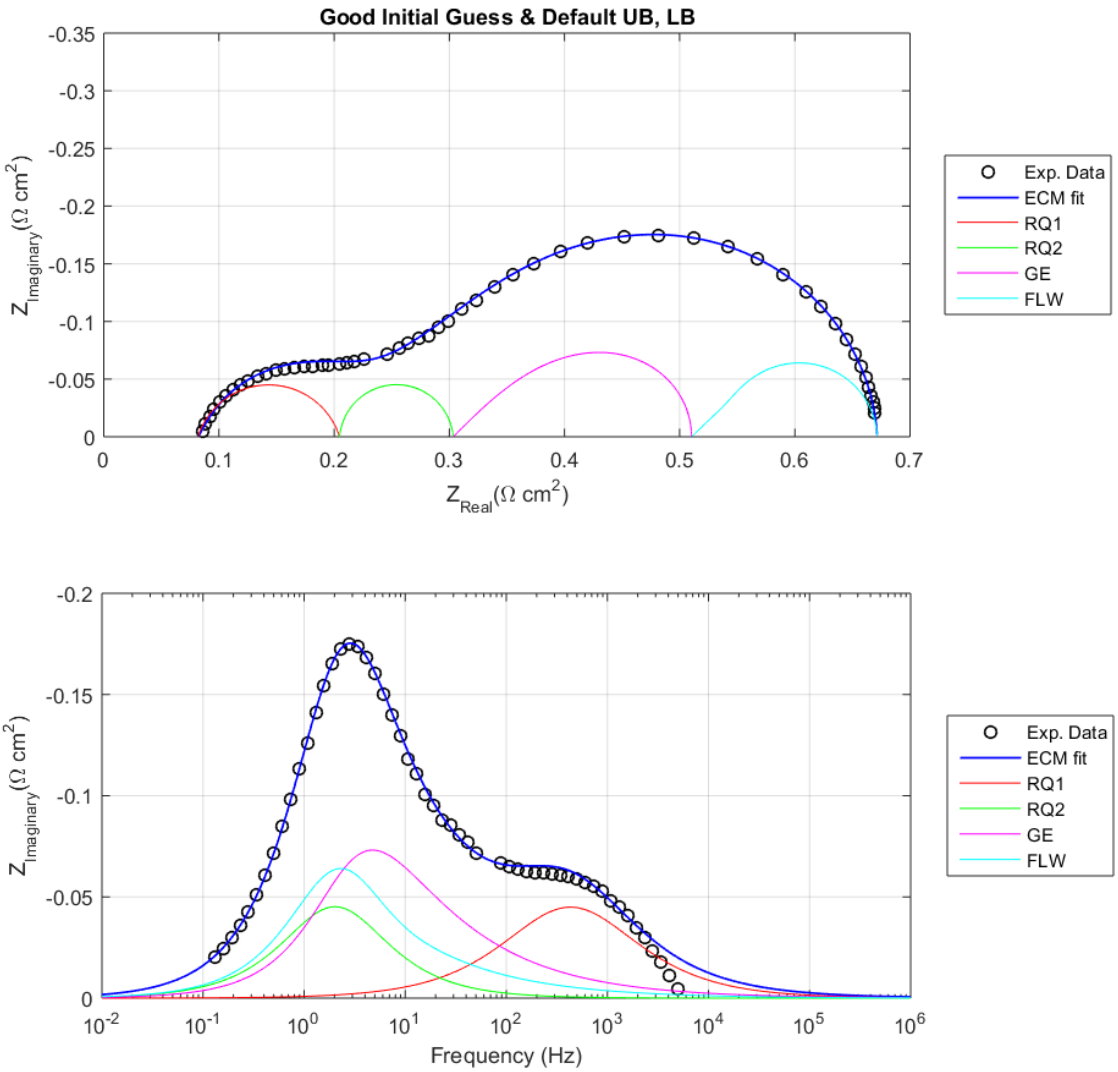

with bad UB and LB, random initial guess

you need good upper bounds and lower bounds, see the result of a poor set here

```
%just arbitrarily setting bounds on all the parameters almost always
%causes failure to produce a good fit
ub=[0.1,0.1,0.99,0.5,0.5,0.99,0.5,0.5,0.5,0.5,0.99,0.99];
lb=[0,0,0,0,0,0,0,0,0,0,0,0];
[fit_3, err_3] = fit_eis_dat('exp_data_fine.csv','Random Initial Guess & BAD
Custom UB, LB',[],ub,lb);
title('Random Initial Guess & BAD Custom UB, LB')
```

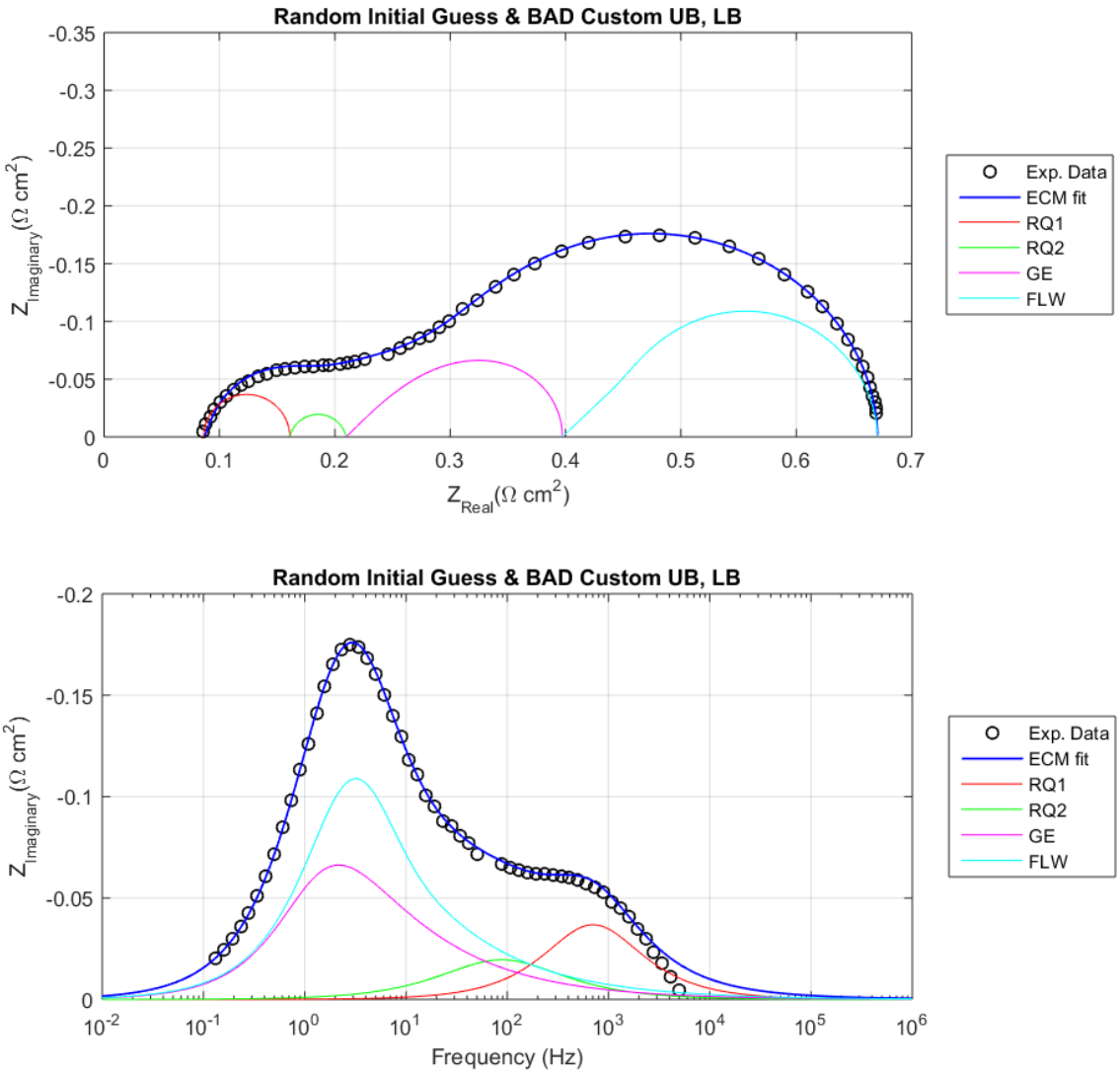

with good UB, random initial guess

```
%We're setting UB for the resistance of the GE element, and leaving everything
else default
ub = [1 1 1 1 1 1 1 1 0.2 1 1 1];
[fit_4, err_4] = fit_eis_dat('exp_data_fine.csv','Random Initial Guess & Good
Custom UB, Default LB',[],ub,[]);
```

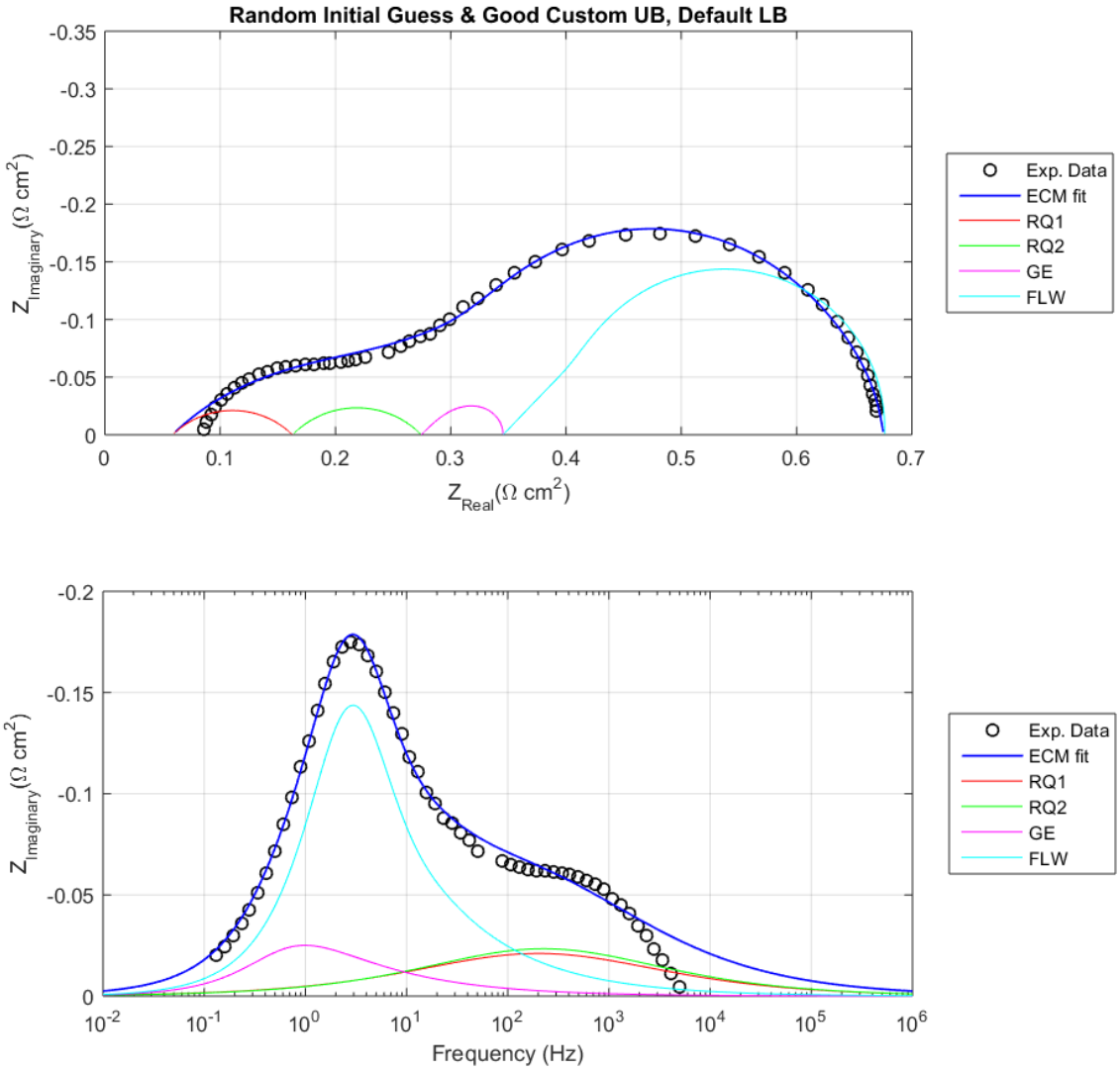

Published with MATLAB® R2015b

BIBLIOGRAPHY

[1] R.P. O'Hayre, S.-W. Cha, W.G. Colella, F.B. Prinz, Fuel Cell Fundamentals, John Wiley & Sons, Inc., Hoboken, New Jersey, 2016.

[2] E.D. Wachsman, K.T. Lee, Lowering the temperature of solid oxide fuel cells, Science. 334 (2011) 935–939. doi:10.1126/science.1204090.

[3] S.C. Singhal, K. Kendall, eds., High Temperature Solid Oxide Fuel Cells: Fundamentals, Design and Applications, Elsevier Ltd, Oxford, UK, 2003.

[4] U.S. Department of Energy, Technology Program Plan Solid Oxide Fuel Cells, Solid Oxide Fuel Cell Technology Program Plan. (2013). https://www.netl.doe.gov/File Library/Research/Coal/energy systems/fuel cells/Program-Plan-Solid-Oxide-Fuel-Cells-2013.pdf.

[5] J.T.S. Irvine, P. Connor, Solid Oxide Fuel Cells: Facts and Figures / Past, Present and Future Perspectives for SOFC Technologies, Springer-Verlag, London, 2013. doi:10.1007/978-1-4471-4456-4.

[6] S.P. Jiang, Nanoscale and nano-structured electrodes of solid oxide fuel cells by infiltration: Advances and challenges, International Journal of Hydrogen Energy. 37 (2012) 449–470. doi:10.1016/j.ijhydene.2011.09.067.

[7] Z. Liu, B. Liu, D. Ding, M. Liu, F. Chen, C. Xia, Review Fabrication and modification of solid oxide fuel cell anodes via wet impregnation/infiltration technique, Journal of Power Sources. 237 (2013) 243–259. doi:10.1016/j.jpowsour.2013.03.025.

[8] J.T.S. Irvine, D. Neagu, M.C. Verbraeken, C. Chatzichristodoulou, C. Graves, M.B. Mogensen, Evolution of the electrochemical interface in high-temperature fuel cells and electrolysers, Nature Energy. 1 (2016) 15014. doi:10.1038/nenergy.2015.14.

[9] P.A. Connor, X. Yue, C.D. Savaniu, R. Price, G. Triantafyllou, M. Cassidy, G. Kerherve, D.J. Payne, R.C. Maher, L.F. Cohen, R.I. Tomov, B.A. Glowacki, R.V. Kumar, J.T.S. Irvine, Tailoring SOFC Electrode Microstructures for Improved Performance, Advanced Energy Materials. 8 (2018) 1–20. doi:10.1002/aenm.201800120.

[10] A. Bertei, J.G. Pharoah, D. a W. Gawel, C. Nicolella, Microstructural modeling and effective properties of infiltrated SOFC electrodes., ECS Transactions. 57 (2013) 2527–2536. doi:10.1149/05701.2527ecst.

[11] L. Holzer, B. Münch, B. Iwanschitz, M. Cantoni, T. Hocker, T. Graule, Quantitative relationships between composition, particle size, triple phase boundary length and surface area in nickel-cermet anodes for Solid Oxide Fuel Cells, Journal of Power Sources. 196 (2011) 7076–7089. doi:10.1016/j.jpowsour.2010.08.006.

[12] S. Futamura, Y. Tachikawa, J. Matsuda, S.M. Lyth, Y. Shiratori, Alternative Ni-Impregnated Mixed Ionic-Electronic Conducting Anode for SOFC Operation at High Fuel Utilization, Journal of the Electrochemical Society. 164 (2017) 3055–3063. doi:10.1149/2.0071710jes.

[13] B. Hua, W. Zhang, M. Li, X. Wang, B. Chi, J. Pu, J. Li, Improved microstructure and performance of Ni-based anode for intermediate temperature solid oxide fuel cells, Journal of Power Sources. 247 (2014) 170–177. doi:10.1016/j.jpowsour.2013.08.060.

[14] P. Keyvanfar, V. Birss, Optimization of Infiltration Techniques Used to Construct Ni/YSZ Anodes, Journal of the Electrochemical Society. 161 (2014) F660–F667. doi:10.1149/2.056405jes.

[15] E.C. Miller, Q. Sherman, Z. Gao, P.W. Voorhees, S.A. Barnett, Stability of Nickel-Infiltrated Anodes in Intermediate Temperature SOFCs, ECS Transactions. 68 (2015) 1245–1254.

[16] B. Hua, M. Li, Y.F. Sun, Y.Q. Zhang, N. Yan, J. Li, T. Etsell, P. Sarkar, J.L. Luo, Grafting doped manganite into nickel anode enables efficient and durable energy conversions in biogas solid oxide fuel cells, Applied Catalysis. B, Environmental. 200 (2017) 174–181. doi:10.1016/j.apcatb.2016.07.001.

[17] M. Li, B. Hua, J.L. Luo, S.P. Jiang, J. Pu, B. Chi, J. Li, Enhancing Sulfur Tolerance of Ni-Based Cermet Anodes of Solid Oxide Fuel Cells by Ytterbium-Doped Barium Cerate Infiltration, ACS Applied Materials and Interfaces. 8 (2016) 10293–10301. doi:10.1021/acsami.6b00925.

[18] S.W. Kim, M. Park, H. Kim, K.J. Yoon, J.W. Son, J.H. Lee, B.K. Kim, J.H. Lee, J. Hong, In-situ nano-alloying Pd-Ni for economical control of syngas production from high-temperature thermo-electrochemical reduction of steam/CO2, Applied Catalysis. B, Environmental. 200 (2017) 265–273. doi:10.1016/j.apcatb.2016.07.008.

[19] B. Timurkutluk, C. Timurkutluk, M.D. Mat, Y. Kaplan, Anode-supported solid oxide fuel cells with ion conductor infiltration, International Journal of Energy Research 35 (2011) 1048–1055. doi:10.1002/er.1832.

[20] S. Sengodan, M. Liu, T.-H. Lim, J. Shin, M. Liu, G. Kim, Enhancing Sulfur

Tolerance of a Ni-YSZ Anode through BaZr0.1Ce0.7Y0.1Yb0.1O3- Infiltration, Journal of the Electrochemical Society. 161 (2014) F668–F673. doi:10.1149/2.068405jes.

[21] R. Kiebach, P. Zielke, J.V.T. Hogh, K. Thyden, H.J. Wang, R. Barford, P. V. Hendriksen, Infiltration of SOFC Stacks: Evaluation of the Electrochemical Performance Enhancement and the Underlying Changes in the Microstructure, Fuel Cells. 16 (2016). doi:10.1002/fuce.201500107.

[22] E.F. Hardjo, D.S. Monder, K. Karan, An Effective Property Model for Infiltrated Electrodes in Solid Oxide Fuel Cells, Journal of the Electrochemical Society. 161 (2014) F83–F93. doi:10.1149/2.036401jes.

[23] Z. Jiao, N. Shikazono, Study on the effects of polarization on local morphological change of nickel at active three-phase-boundary using patterned nickel-film electrode in solid oxide fuel cell anode, Acta Materialia. 135 (2017) 124–131. doi:10.1016/j.actamat.2017.05.051.

[24] N. Mahato, A. Banerjee, A. Gupta, S. Omar, K. Balani, Progress in material selection for solid oxide fuel cell technology: A review, Progress in Materials Science. 72 (2015) 141–337. doi:10.1016/j.pmatsci.2015.01.001.

[25] A. Faes, A. Hessler-Wyser, D. Presvytes, C.G. Vayenas, J. Vanherle, Nickel-zirconia anode degradation and triple phase boundary quantification from microstructural analysis, Fuel Cells. 9 (2009) 841–851. doi:10.1002/fuce.200800147.

[26] A. Hagen, R. Barfod, P.V. Hendriksen, Y.-L. Liu, S. Ramousse, Degradation of Anode Supported SOFCs as a Function of Temperature and Current Load, Journal of the Electrochemical Society. 153 (2006) A1165–A1171. doi:10.1149/1.2193400.

[27] R. Wang, M. Würth, U.B. Pal, S. Gopalan, S.N. Basu, Roles of humidity and cathodic current in chromium poisoning of Sr-doped LaMnO3-based cathodes in solid oxide fuel cells, Journal of Power Sources. 360 (2017) 87–97. doi:10.1016/j.jpowsour.2017.06.005.

[28] P.I. Cowin, C.T.G. Petit, R. Lan, J.T.S. Irvine, S. Tao, Recent progress in the development of anode materials for solid oxide fuel cells, Advanced Energy Materials. 1 (2011) 314–332. doi:10.1002/aenm.201100108.

[29] B. Shri Prakash, S. Senthil Kumar, S.T. Aruna, Properties and development of Ni/YSZ as an anode material in solid oxide fuel cell: A review, Renewable and Sustainable Energy Reviews. 36 (2014). doi:10.1016/j.rser.2014.04.043.

[30] S.P. Jiang, S.H. Chan, A review of anode materials development in solid oxide fuel cells, Journal of Materials Science. 39 (2004) 4405–4439. doi:10.1023/b:jmsc.0000034135.52164.6b.

[31] Y. Zhang, R. Knibbe, J. Sunarso, Y. Zhong, W. Zhou, Z. Shao, Z. Zhu, Recent Progress on Advanced Materials for Solid-Oxide Fuel Cells Operating Below 500 °C, Advanced Materials. 29 (2017). doi:10.1002/adma.201700132.

[32] S.P.S. Badwal, S. Giddey, C. Munnings, A. Kulkarni, Review of progress in high temperature solid oxide fuel cells, Journal of the Australian Ceramic Society. 50 (2014) 23–37. doi:10.1002/chin.201531316.

[33] A. Bertei, E. Ruiz-Trejo, K. Kareh, V. Yufit, X. Wang, F. Tariq, N.P. Brandon, The fractal nature of the three-phase boundary: A heuristic approach to the degradation of nanostructured Solid Oxide Fuel Cell anodes, Nano Energy. 38 (2017) 526–536. doi:10.1016/j.nanoen.2017.06.028.

[34] S. Dierickx, J. Joos, A. Weber, E. Ivers-Tiffée, Advanced impedance modelling of Ni/8YSZ cermet anodes, Electrochimica Acta. 265 (2018) 736–750. doi:10.1016/j.electacta.2017.12.029.

[35] O.M. Pecho, A. Mai, B. Münch, T. Hocker, R.J. Flatt, L. Holzer, 3D microstructure effects in Ni-YSZ anodes: Influence of TPB lengths on the electrochemical performance, Materials (Basel). 8 (2015) 7129–7144. doi:10.3390/ma8105370.

[36] K.J. Yoon, P. Zink, S. Gopalan, U.B. Pal, Polarization measurements on single-step co-fired solid oxide fuel cells (SOFCs), Journal of Power Sources. 172 (2007) 39–49. doi:10.1016/j.jpowsour.2007.03.003.

[37] A. Leonide, V. Sonn, A. Weber, E. Ivers-Tiffée, Evaluation and Modeling of the Cell Resistance in Anode-Supported Solid Oxide Fuel Cells, Journal of the Electrochemical Society. 155 (2008) B36–B41. doi:10.1149/1.2801372.

[38] C. Bao, Z. Jiang, X. Zhang, Modeling mass transfer in solid oxide fuel cell anode: I. Comparison between Fickian, Stefan-Maxwell and dusty-gas models, Journal of Power Sources. 310 (2016) 32–40.

[39] K.J. Yoon, S. Gopalan, U.B. Pal, Effect of fuel composition on performance of single-step cofired SOFCs, Journal of the Electrochemical Society. 154 (2007) B1080. doi:10.1149/1.2769826.

[40] A. Leonide, Y. Apel, E. Ivers-Tiffée, SOFC modeling and parameter identification by means of impedance spectroscopy, ECS Transactions. 19 (2009) 81–109. doi:10.1149/1.3247567.

[41] J.-C. Njodzefon, D. Klotz, A. Kromp, A. Weber, E. Ivers-Tiffée, Electrochemical Modeling of the Current-Voltage Characteristics of an SOFC in Fuel Cell and Electrolyzer Operation Modes, Journal of the Electrochemical Society. 160 (2013) F313–F323. doi:10.1149/2.018304jes.

[42] C. Boigues Muñoz, D. Pumiglia, S.J. McPhail, D. Montinaro, G. Comodi, G. Santori, M. Carlini, F. Polonara, More accurate macro-models of solid oxide fuel cells through electrochemical and microstructural parameter estimation - Part I: Experimentation, Journal of Power Sources. 294 (2015) 658–668. doi:10.1016/j.jpowsour.2015.06.118.

[43] C. Boigues-Muñoz, D. Pumiglia, S.J. McPhail, G. Santori, D. Montinaro, G. Comodi, M. Carlini, F. Polonara, More accurate macro-models of solid oxide fuel cells through electrochemical and microstructural parameter estimation - Part II: Parameter estimation, Journal of Power Sources. 286 (2015) 321–329. doi:10.1016/j.jpowsour.2015.03.129.

[44] A. Leonide, V. Sonn, A. Weber, E. Ivers-Tiffée, Evaluation and Modeling of the Cell Resistance in Anode-Supported Solid Oxide Fuel Cells, Journal of the Electrochemical Society. 155 (2008) B36–B41. doi:10.1149/1.2801372.

[45] V. Sonn, a. Leonide, E. Ivers-Tiffée, Combined Deconvolution and CNLS Fitting Approach Applied on the Impedance Response of Technical Ni/8YSZ Cermet Electrodes, Journal of the Electrochemical Society. 155 (2008) B675. doi:10.1149/1.2908860.

[46] K.T. Lee, N.J. Vito, E.D. Wachsman, Comprehensive quantification of Ni-Gd0.1Ce0.9O 1.95 anode functional layer microstructures by three-dimensional reconstruction using a FIB/SEM dual beam system, Journal of Power Sources. 228 (2013) 220–228. doi:10.1016/j.jpowsour.2012.11.117.

[47] D. Klotz, A. Weber, E. Ivers-Tiffée, Practical Guidelines for Reliable Electrochemical Characterization of Solid Oxide Fuel Cells, Electrochimica Acta. 227 (2017) 110–126. doi:10.1016/j.electacta.2016.12.148.

[48] L. Barelli, E. Barluzzi, G. Bidini, Diagnosis methodology and technique for solid oxide fuel cells: A review, International Journal of Hydrogen Energy. 38 (2013) 5060–5074. doi:10.1016/j.ijhydene.2013.02.024.

[49] G. DiGiuseppe, Seal Leakage Effects on the Electrical Performance of an SOFC Button Cell, Journal of Fuel Cell Science and Technology. 9 (2012) 061006. doi:10.1115/1.4007815.

[50] E. Pahon, N. Yousfi Steiner, S. Jemei, D. Hissel, M.C. Péra, K. Wang, P. Moçoteguy, Solid oxide fuel cell fault diagnosis and ageing estimation based on

wavelet transform approach, International Journal of Hydrogen Energy. 41 (2016) 13678–13687. doi:10.1016/j.ijhydene.2016.06.143.

[51] D. Kennouche, Y.C.K. Chen-Wiegart, K.J. Yakal-Kremski, J. Wang, J.W. Gibbs, P.W. Voorhees, S.A. Barnett, Observing the microstructural evolution of Ni-Yttria-stabilized zirconia solid oxide fuel cell anodes, Acta Materialia. 103 (2016) 204–210. doi:10.1016/j.actamat.2015.09.055.

[52] A. Ploner, A. Hagen, A. Hauch, Classical statistical methodology for accelerated testing of Solid Oxide Fuel Cells, Journal of Power Sources. 395 (2018) 379–385. doi:10.1016/j.jpowsour.2018.05.034.

[53] A. Ploner, A. Hagen, A. Hauch, Study of Operating Parameters for Accelerated Anode Degradation in SOFCs, Fuel Cells. (2017) 1–10. doi:10.1002/fuce.201600193.

[54] M.S. Khan, S.B. Lee, R.H. Song, J.W. Lee, T.H. Lim, S.J. Park, Fundamental mechanisms involved in the degradation of nickel-yttria stabilized zirconia (Ni-YSZ) anode during solid oxide fuel cells operation: A review, Ceramics International. 42 (2015) 35–48. doi:10.1016/j.ceramint.2015.09.006.

[55] T. Matsui, R. Kishida, J.-Y. Kim, H. Muroyama, K. Eguchi, Performance Deterioration of Ni–YSZ Anode Induced by Electrochemically Generated Steam in Solid Oxide Fuel Cells, Journal of the Electrochemical Society. 157 (2010) B776. doi:10.1149/1.3336830.

[56] Z. Jiao, N. Shikazono, N. Kasagi, Performance of an anode support solid oxide fuel cell manufactured by microwave sintering, Journal of Power Sources. 195 (2010) 151–154. doi:10.1016/j.jpowsour.2009.07.009.

[57] K.J. Yoon, High Performance Single Step Co-fired Solid Oxide Fuel Cells (SOFC): Polarization Measurements and Analysis, Boston University, 2008.

[58] W. He, K.J. Yoon, R.S. Eriksen, S. Gopalan, S.N. Basu, U.B. Pal, Out-of-cell measurements of H2-H2O effective binary diffusivity in the porous anode of solid oxide fuel cells (SOFCs), Journal of Power Sources. 195 (2010) 532–535. doi:10.1016/j.jpowsour.2009.07.051.

[59] Q.A. Huang, R. Hui, B. Wang, J. Zhang, A review of AC impedance modeling and validation in SOFC diagnosis, Electrochimica Acta. 52 (2007) 8144–8164. doi:10.1016/j.electacta.2007.05.071.

[60] A. Utz, H. Störmer, A. Leonide, A. Weber, E. Ivers-Tiffée, Degradation and Relaxation Effects of Ni Patterned Anodes in H2–H2O Atmosphere, Journal of the Electrochemical Society. 157 (2010) B920. doi:10.1149/1.3383041.

[61] M.J. Jørgensen, M. Mogensen, Impedance of Solid Oxide Fuel Cell LSM / YSZ Composite Cathodes, Journal of the Electrochemical Society. 148 (2001) A433–A442. doi:10.1149/1.1360203.

[62] J.-C. Njodzefon, C.R. Graves, M.B. Mogensen, A. Weber, J. Hjelm, Kinetic Studies on State of the Art Solid Oxide Cells: A Comparison between Hydrogen/Steam and Reformate Fuels, Journal of the Electrochemical Society. 163 (2016) F1451–F1462. doi:10.1149/2.1201613jes.

[63] A. Kromp, S. Dierickx, A. Leonide, A. Weber, E. Ivers-Tiffée, Electrochemical Analysis of Sulfur-Poisoning in Anode Supported SOFCs Fuelled with a Model Reformate, Journal of the Electrochemical Society. 159 (2012) B597–B601. doi:10.1149/2.015206jes.

[64] B.A. Boukamp, A. Rolle, Use of a distribution function of relaxation times (DFRT) in impedance analysis of SOFC electrodes, Solid State Ionics. 314 (2018) 103–111. doi:10.1016/j.ssi.2017.11.021.

[65] E. Ivers-Tiffée, A. Weber, Evaluation of electrochemical impedance spectra by the distribution of relaxation times, Journal of the Ceramic Society of Japan. 125 (2017) 193–201. doi:10.2109/jcersj2.16267.

[66] C. Graves, J. Hjelm, Advanced impedance modeling of solid oxide electrochemical cells, 11th European SOFC and SOE Forum 2014. European Fuel Cell Forum. B1203 (2014) 1–12.

[67] A. Leonide, SOFC Modelling and Parameter Identification by means of Impedance Spectroscopy. KIT Scientific Publishing, 2010.

[68] D. Klotz, A. Leonide, A. Weber, E. Ivers-Tiffée, Electrochemical model for SOFC and SOEC mode predicting performance and efficiency, International Journal of Hydrogen Energy. 39 (2014) 20844–20849. doi:10.1016/j.ijhydene.2014.08.139.

[69] D.M. Silva-Mosqueda, F. Elizalde-Blancas, D. Pumiglia, F. Santoni, C. Boigues-Muñoz, S.J. McPhail, Intermediate temperature solid oxide fuel cell under internal reforming: Critical operating conditions, associated problems and their impact on the performance, Applied Energy. 235 (2019) 625–640. doi:10.1016/j.apenergy.2018.10.117.

[70] M. Schönleber, E. Ivers-Tiffée, Approximability of impedance spectra by RC elements and implications for impedance analysis, Electrochemistry Communications. 58 (2015) 15–19. doi:10.1016/j.elecom.2015.05.018.

[71] T.H. Wan, M. Saccoccio, C. Chen, F. Ciucci, Influence of the Discretization Methods on the Distribution of Relaxation Times Deconvolution: Implementing

Radial Basis Functions with DRTtools, Electrochimica Acta. 184 (2015) 483–499. doi:10.1016/j.electacta.2015.09.097.

[72] D. Klotz, J.P. Schmidt, A. Kromp, A. Weber, E. Ivers-Tiffée, The Distribution of Relaxation Times as Beneficial Tool for Equivalent Circuit Modeling of Fuel Cells and Batteries, ECS Transactions. 41 (2012) 25–33. doi:10.1149/1.3692958.

[73] B.A. Boukamp, Fourier transform distribution function of relaxation times; application and limitations, Electrochimica Acta. 154 (2015) 35–46. doi:10.1016/j.electacta.2014.12.059.

[74] B.A. Boukamp, A. Rolle, Analysis and Application of Distribution of Relaxation Times in Solid State Ionics, Solid State Ionics. 302 (2016) 12–18. doi:10.1016/j.ssi.2016.10.009.

[75] B.A. Boukamp, Derivation of a Distribution Function of Relaxation Times for the (fractal) Finite Length Warburg., Electrochimica Acta. 252 (2017) 154–163. doi:10.1016/j.electacta.2017.08.154.

[76] B.A. Boukamp, A Linear Kronig-Kramers Transform Test for Immittance Data Validation, Journal of the Electrochemical Society. 142 (1995) 1885–1894. doi:10.1149/1.2044210.

[77] M. Schönleber, D. Klotz, E. Ivers-Tiffée, A Method for Improving the Robustness of linear Kramers-Kronig Validity Tests, Electrochimica Acta. 131 (2014) 20–27. doi:10.1016/j.electacta.2014.01.034.

[78] M. Schönleber, R. Goyal, E. Ivers-Tiffée, Lin-KK, (n.d.). http://www.iwe.kit.edu/Lin-KK.php (accessed January 6, 2019).

[79] J.M. Vohs, R.J. Gorte, High-performance SOFC cathodes prepared by infiltration, Advanced Materials. 21 (2009) 943–956. doi:10.1002/adma.200802428.

[80] R.J. Gorte, J.M. Vohs, Nanostructured anodes for solid oxide fuel cells, Current Opinion in Colloid & Interface Science. 14 (2009) 236–244. doi:10.1016/j.cocis.2009.04.006.

[81] S.P. Jiang, A review of wet impregnation - An alternative method for the fabrication of high performance and nano-structured electrodes of solid oxide fuel cells, Materials Science & Engineering. A, Structural Materials. 418 (2006) 199–210. doi:10.1016/j.msea.2005.11.052.

[82] T. Klemensø, K. Thydén, M. Chen, H.J. Wang, Stability of Ni-yttria stabilized zirconia anodes based on Ni-impregnation, Journal of Power Sources. 195 (2010) 7295–7301. doi:10.1016/j.jpowsour.2010.05.047.

[83] A.N.N. Busawon, D. Sarantaridis, A. Atkinson, Ni Infiltration as a Possible Solution to the Redox Problem of SOFC Anodes, Electrochemical and Solid-State Letters. 11 (2008) B186. doi:10.1149/1.2959078.

[84] M. Kishimoto, H. Iwai, M. Saito, H. Yoshida, Quantitative evaluation of solid oxide fuel cell porous anode microstructure based on focused ion beam and scanning electron microscope technique and prediction of anode overpotentials, Journal of Power Sources. 196 (2011) 4555–4563. doi:10.1016/j.jpowsour.2010.12.100.

[85] C. Endler, A. Leonide, A. Weber, F. Tietz, E. Ivers-tiffée, Time-Dependent Electrode Performance Changes in Intermediate Temperature Solid Oxide Fuel Cells, Journal of the Electrochemical Society. 157 (2010) 292–298. doi:10.1149/1.3270047.

[86] P. Keyvanfar, Structural and Electrochemical Stability of Ni-Infiltrated Anodes for SOFC Applications, University of Calgary, 2017.

[87] A.R. Hanifi, S. Paulson, A. Torabi, A. Shinbine, M.C. Tucker, V. Birss, T.H. Etsell, P. Sarkar, Slip-cast and hot-solution infiltrated porous yttria stabilized zirconia (YSZ) supported tubular fuel cells, Journal of Power Sources. 266 (2014) 121–131. doi:10.1016/j.jpowsour.2014.05.001.

[88] A. Buyukaksoy, V. Petrovsky, F. Dogan, Optimization of redox stable Ni-YSZ anodes for SOFCs by two-step infiltration, Journal of the Electrochemical Society. 159 (2012) F841–F848. doi:10.1149/2.075212jes.

[89] T.L. Skafte, J. Hjelm, P. Blennow, C. Graves, Reactivating the Ni-YSZ electrode in solid oxide cells and stacks by infiltration, Journal of Power Sources. 378 (2018) 685–690. doi:10.1016/j.jpowsour.2018.01.021.

[90] K. Joong Yoon, M. Biswas, H.J. Kim, M. Park, J. Hong, H. Kim, J.W. Son, J.H. Lee, B.K. Kim, H.W. Lee, Nano-tailoring of infiltrated catalysts for high-temperature solid oxide regenerative fuel cells, Nano Energy. 36 (2017) 9–20. doi:10.1016/j.nanoen.2017.04.024.

[91] T.E. Burye, J.D. Nicholas, Precursor solution additives improve desiccated La0.6Sr0.4Co0.8Fe0.2O3-x infiltrated solid oxide fuel cell cathode performance, Journal of Power Sources. 301 (2016) 287–298. doi:10.1016/j.jpowsour.2015.10.012.

[92] R.P. Dowd, S. Lee, Y. Fan, K. Gerdes, Engineering the solid oxide fuel cell electrocatalyst infiltration technique for industrial use, International Journal of Hydrogen Energy. 41 (2016) 14971–14981. doi:10.1016/j.ijhydene.2016.06.015.

[93] E. Ruiz-Trejo, A.K. Azad, J.T.S. Irvine, A 60-Second Microwave-Assisted Synthesis of Nickel Foam and Its Application to the Impregnation of Porous Scaffolds, Journal of the Electrochemical Society. 162 (2015) F273–F279. doi:10.1149/2.0531503jes.

[94] E. Ruiz-Trejo, A. Atkinson, N.P. Brandon, Metallizing porous scaffolds as an alternative fabrication method for solid oxide fuel cell anodes, Journal of Power Sources. 280 (2015) 81–89. doi:10.1016/j.jpowsour.2015.01.091.

[95] Z. Jamil, E. Ruiz-Trejo, P. Boldrin, N.P. Brandon, Anode fabrication for solid oxide fuel cells: Electroless and electrodeposition of nickel and silver into doped ceria scaffolds, International Journal of Hydrogen Energy. 41 (2016) 9627–9637. doi:10.1016/j.ijhydene.2016.04.061.

[96] X. Wu, Y. Tian, J. Zhang, W. Zuo, X. Kong, J. Wang, K. Sun, X. Zhou, Enhanced electrochemical performance and carbon anti-coking ability of solid oxide fuel cells with silver modified nickel-yttrium stabilized zirconia anode by electroless plating, Journal of Power Sources. 301 (2016) 143–150. doi:10.1016/j.jpowsour.2015.10.006.

[97] Z. Jiao, N. Shikazono, In operando optical study of active three phase boundary of nickel-yttria stabilized zirconia solid-oxide fuel cell anode under polarization, Journal of Power Sources. 396 (2018) 119–123. doi:10.1016/j.jpowsour.2018.06.001.

[98] T. Shimonosono, Y. Hirata, Y. Ehira, S. Sameshima, T. Horita, H. Yokokawa, Electronic conductivity measurement of Gd- And Sm-doped ceria ceramics by Hebb-Wagner method, Solid State Ionics. 174 (2004) 27–33. doi:10.1016/j.ssi.2004.07.025.

[99] K. Miyawaki, M. Kishimoto, H. Iwai, M. Saito, H. Yoshida, Comprehensive understanding of the active thickness in solid oxide fuel cell anodes using experimental, numerical and semi-analytical approach, Journal of Power Sources. 267 (2014) 503–514. doi:10.1016/j.jpowsour.2014.05.112.

[100] W.C. Chueh, Y. Hao, W. Jung, S.M. Haile, High electrochemical activity of the oxide phase in model ceria-Pt and ceria-Ni composite anodes, Nature Materials. 11 (2012) 155–161. doi:10.1038/nmat3184.

[101] J. Nielsen, T. Klemenso, P. Blennow, Detailed impedance characterization of a well performing and durable Ni:CGO infiltrated cermet anode for metal-supported solid oxide fuel cells, Journal of Power Sources. 219 (2012) 305–316. doi:10.1016/j.jpowsour.2012.07.031.

[102] P. Blennow, J. Hjelm, T. Klemensø, Å. Persson, K. Brodersen, A.K. Srivastava, H.L. Frandsen, M. Lundberg, S. Ramousse, M. Mogensen, Development of Planar Metal Supported SOFC with Novel Cermet Anode, ECS Transactions. 25 (2009) 701–710.

[103] M. Lomberg, E. Ruiz-Trejo, G. Offer, N.P. Brandon, Characterization of Ni-infiltrated GDC electrodes for solid oxide cell applications, Journal of the Electrochemical Society. 161 (2014) F899–F905. doi:10.1149/2.0501409jes.

[104] O.A. Marina, C. Bagger, S. Primdahl, M. Mogensen, A solid oxide fuel cell with a gadolinia-doped ceria anode: preparation and performance, Solid State Ionics. 123 (1999) 199–208. doi:10.1016/s0167-2738(99)00111-3.

[105] P. Kim-Lohsoontorn, Y.M. Kim, N. Laosiripojana, J. Bae, Gadolinium doped ceria-impregnated nickel-yttria stabilised zirconia cathode for solid oxide electrolysis cell, International Journal of Hydrogen Energy. 36 (2011) 9420–9427. doi:10.1016/j.ijhydene.2011.04.199.

[106] S.P. Jiang, S. Zhang, Y.D. Zhen, A.P. Koh, Performance of GDC-Impregnated Ni Anodes of SOFCs, Electrochemical and Solid-State Letters. 7 (2004) A282. doi:10.1149/1.1783112.

[107] M. Vogler, A. Bieberle-hütter, L. Gauckler, J. Warnatz, W.G. Bessler, J.E. Soc, P. B-b, Ni/YSZ Patterned Anode Modelling Study of Surface Reactions, Diffusion, and Spillover at a Modelling Study of Surface Reactions, Diffusion, and Spillover at a Ni/YSZ Patterned Anode, Journal of the Electrochemical Society. 156 (2009) 663–672. doi:10.1149/1.3095477.

[108] W.G. Bessler, M. Vogler, H. Störmer, D. Gerthsen, A. Utz, A. Weber, E. Ivers-Tiffée, ab Marcel Vogler, ab Heike Stomer, D. Gerthsen, A. Utz, E. Ivers-Tiffeé de, Model anodes and anode models for understanding the mechanism of hydrogen oxidation in solid oxide fuel cells., Physical Chemistry Chemical Physics. 12 (2010) 13888–903. doi:10.1039/c0cp00541j.

[109] A. Kromp, A. Leonide, A. Weber, E. Ivers-Tiffée, Electrochemical Analysis of Reformate-Fuelled Anode Supported SOFC, Journal of the Electrochemical Society. 158 (2011) B980. doi:10.1149/1.3597177.

[110] R. Wang, E. Dogdibegovic, G.Y. Lau, M.C. Tucker, Metal-Supported Solid Oxide Electrolysis Cell with Significantly Enhanced Catalysis, Energy Technology. 7 (2019) 1–13. doi:10.1002/ente.201801154.

[111] Y. Lu, P. Gasper, U.B. Pal, S. Gopalan, S.N. Basu, Improving intermediate temperature performance of Ni-YSZ cermet anodes for solid oxide fuel cells by liquid infiltration of nickel nanoparticles, Journal of Power Sources. 396 (2018)

257–264. doi:10.1016/j.jpowsour.2018.06.027.

[112] L. Zhang, A. V. Virkar, On Space Charge and Spatial Distribution of Defects in Yttria-Stabilized Zirconia, Journal of the Electrochemical Society. 164 (2017) F1506–F1523. doi:10.1149/2.1801713jes.

[113] J. Nielsen, J. Hjelm, Impedance of SOFC electrodes: A review and a comprehensive case study on the impedance of LSM:YSZ cathodes, Electrochimica Acta. 115 (2014) 31–45. doi:10.1016/j.electacta.2013.10.053.

[114] R. de Levie, Electrochemical Responses of Porous and Rough Electrodes, in: P. Delahay (Ed.), Advances in Electrochemistry and Electrochemical Engineering, Vol. 6, Electrochemistry. Interscience Publishers, New York, N.Y., 1967: p. 329.

[115] D.G. Goodwin, H. Zhu, A.M. Colclasure, R.J. Kee, Modeling Electrochemical Oxidation of Hydrogen on Ni–YSZ Pattern Anodes, Journal of the Electrochemical Society. 156 (2009) B1004. doi:10.1149/1.3148331.

[116] R. Barfod, A. Hagen, S. Ramousse, P. V. Hendriksen, M. Mogensen, Break down of losses in thin electrolyte SOFCs, Fuel Cells. 6 (2006) 141–145. doi:10.1002/fuce.200500113.

[117] V. Kharton, F. Marques, A. Atkinson, Transport properties of solid oxide electrolyte ceramics: a brief review, Solid State Ionics. 174 (2004) 135–149.

[118] S.M. Haile, Fuel cell materials and components, Acta Materialia. 51 (2003) 5981–6000.

[119] H. Uchida, S. Suzuki, M. Watanabe, High performance electrode for medium-temperature solid oxide fuel cells: Mixed conducting ceria-based anode with highly dispersed Ni electrocatalysts, Electrochemical and Solid State Letters. 6 (2003) A174–A177.

[120] H. Uchida, T. Osuga, M. Watanabe, High-performance electrode for medium-temperature solid oxide fuel cells: Control of microstructure of ceria-based anodes with highly dispersed ruthenium electrocatalysts, Journal of the Electrochemical Society. 146 (1999) 1677–1682.

[121] S. McIntosh, J.M. Vohs, R.J. Gorte, Effect of precious-metal dopants on SOFC anodes for direct utilization of hydrocarbons, Electrochemical and Solid State Letters. 6 (2003) A240–A243.

[122] M.D. Gross, J.M. Vohs, R.J. Gorte, A strategy for achieving high performance with SOFC ceramic anodes, Electrochemical and Solid State Letters. 10 (2007) B65–B69.

[123] A.-K. Huber, M. Falk, M. Rohnke, B. Luerssen, M. Amati, L. Gregoratti, D. Hesse, J. Janek, In situ study of activation and de-activation of LSM fuel cell cathodes – Electrochemistry and surface analysis of thin-film electrodes, Journal of Catalysis. 294 (2012) 79–88. doi:10.1016/j.jcat.2012.07.010.

[124] M.A. Haider, S. McIntosh, Evidence for Two Activation Mechanisms in LSM SOFC Cathodes, Journal of the Electrochemical Society. 156 (2009) B1369–B1375. doi:10.1149/1.3231500.

[125] K. Murakami, T. Matsui, R. Kikuchi, H. Muroyama, K. Eguchi, Activation of LSM Electrode Related to the Potential Oscillation under Cathodic Polarization, Journal of the Electrochemical Society. 157 (2010) B880–B884. doi:10.1149/1.3374407.

[126] V.A.C. Haanappei, A. Mai, J. Mertens, Electrode activation of anode-supported SOFCs with LSM- or LSCF-type cathodes, Solid State Ionics. 177 (2006) 2033–2037. doi:10.1016/j.ssi.2005.12.038.

CURRICULUM VITAE